UNIVERSITÉ LILLE1 SCIENCES ET TECHNOLOGIES
ÉCOLE DOCTORALE DES SCIENCES POUR L'INGÉNIEUR

THÈSE

PRÉSENTÉE EN VUE D'OBTENIR LE GRADE DE

DOCTEUR EN GÉNIE ÉLECTRIQUE

PAR

ZIFU WANG

CONTRIBUTION TO FINITE ELEMENT ANALYSIS OF MAGNETO-MECHANICAL AND MAGNETO-THERMAL PHENOMENA

SOUTENUE LE 5 DÉCEMBRE 2013

DEVANT LE JURY :

M. HERBERT DE GERSEM	RAPPORTEUR
M. GÉRARD MEUNIER	RAPPORTEUR
M. FRÉDÉRIC BOUILLAULT	EXAMINATEUR
M. PATRICK DULAR	EXAMINATEUR
M. JEAN-CLAUDE MIPO	EXAMINATEUR
M. THOMAS HENNERON	ENCADRANT
M. FRANCIS PIRIOU	DIRECTEUR DE THÈSE

Zifu Wang: *Contribution to Finite Element Analysis of Magneto-Mechanical and Magneto-Thermal Phenomena,* Ph.D. thesis, © Dec. 6, 2013.

ABSTRACT

The work presented in this thesis aims to contribute to finite element analysis of weak-coupling magneto-mechanical and magneto-thermal phenomena.

In general, magneto-mechanical and magneto-thermal problems are made up of subproblems of which the physical nature differs. Using weak-coupling strategies, these subproblems can be calculated separately using finite element methods, and thus on their own meshes, in order to ensure precision. To obtain a precise solution for the entire problem, it is crucial to ensure the transmission of information between the subproblems. In this work, we study field projection methods on overlapping domains.

Field projection formulations are given for classical L^2 or $\mathbf{L}^2$ spaces, as well as for $\mathrm{H}(\mathbf{grad})$, $\mathbf{H}(\mathbf{curl})$ and $\mathbf{H}(div)$ in order to obtain increased projection accuracy for the distributional derivatives. A Petrov-Galerkin method is presented to fill the test space using a bi-orthogonal basis, in order to reduce the computation cost of L^2 or $\mathbf{L}^2$ Ritz-Galerkin projections. Practical implementation techniques are also discussed in detail with respect to their accuracy, speed and simplicity of their implementation. Subsequently, with energy-conserving formulations for electromagnetic fields, applications of mesh-to-mesh projections are demonstrated. The accuracy and efficiency of the presented projection methods are given through multi-physics problems. The thesis closes with some conclusions and possibilities for future work.

Keywords: finite element methods, multi-physics, weak-coupling, magneto-mechanical, magneto-thermal, Galerkin method, field projection.

CONTENTS

INTRODUCTION 1
- Scope and objectives 1
- Outline 2

1 COMPUTATIONAL MODELS 3
- 1.1 Electromagnetic model 3
  - 1.1.1 Continuous problem 3
  - 1.1.2 Potential formulations 6
- 1.2 Mechanical model 8
  - 1.2.1 Continuous problem 9
  - 1.2.2 Displacement formulations 10
- 1.3 Thermal model 10
  - 1.3.1 Continuous problem 10
  - 1.3.2 Temperature formulations 11
- 1.4 Functional framework 12
- 1.5 Finite element methods 13

2 MODEL COUPLING 17
- 2.1 Projection formulations 17
  - 2.1.1 Spaces for field projections 18
  - 2.1.2 Problem to be solved 19
  - 2.1.3 Weak formulations 20
  - 2.1.4 Test function choices 20
  - 2.1.5 Mesh-to-mesh implementation 24
  - 2.1.6 Numerical example 26
  - 2.1.7 Conclusion 34
- 2.2 Implementation consideration 35
  - 2.2.1 Sampling-integration over the target elements 35
  - 2.2.2 Numerical example 36
  - 2.2.3 Conclusion 38
- 2.3 Energetic formulations for electromagnetic fields 38
  - 2.3.1 Magneto-static problems 39
  - 2.3.2 Eddy current problems 41
  - 2.3.3 Numerical example (linear media) 41
  - 2.3.4 Nonlinear magnetic media 45
  - 2.3.5 Numerical example (nonlinear media) 47

2.3.6 Conclusion 49

3 APPLICATIONS 51
3.1 Discretization of uniform analytical current densities 51
3.1.1 Formulations 52
3.1.2 Applications 53
3.1.3 Conclusion 57
3.2 Cylindrical conductor carrying uniform currents 57
3.2.1 Magneto-mechanical calculation on common meshes 58
3.2.2 Magneto-mechanical calculation with M1-to-M2 projection 60
3.2.3 Conclusion 61
3.3 Two face-to-face iron cores 61
3.3.1 From the magneto-static problem to mechanical deformations 61
3.3.2 From the magneto-harmonic problem to temperature rises 63
3.3.3 Conclusion 65
3.4 Electromagnet facing an elastic plate 65
3.4.1 Comparison of projection techniques 67
3.4.2 Comparison of implementation techniques 67
3.4.3 Conclusion 70
3.5 Double-excitation synchronous alternator 70
3.5.1 Magneto-mechanical calculations 70
3.5.2 Conclusion 76

GENERAL CONCLUSIONS 79
Conclusions 79
Contributions 80
Future prospects 81

A APPENDIX: BI-ORTHOGONAL FUNCTIONS 83
Nodal bi-orthogonal functions 83
Edge bi-orthogonal functions 84
Facet bi-orthogonal functions 86

ACKNOWLEDGMENTS 89

BIBLIOGRAPHY 91

LIST OF FIGURES

Figure 1 Study domain for electromagnetic models. 4

Figure 2 Boundary conditions for electromagnetic models. 6

Figure 3 Maxwell's house. 13

Figure 4 Whitney functions and bi-orthogonal functions associated with the common edge. 23

Figure 5 Whitney functions and bi-orthogonal functions associated with the common facet. 24

Figure 6 Intersections (green) of one target triangular element (red) with the source mesh (blue). Three quadrature points can then be applied to each intersection (green stars). The resulting mesh is actually the lowest common mesh for source and target meshes. 25

Figure 7 Meshes of the cubic domain used here. 26

Figure 8 Projected field on mesh 1 (edge elements), obtained in the analytical-to-discretized projection using the $\mathbf{L}^2(D)$ Ritz-Galerkin method. 29

Figure 9 Curl of projected fields, plotted on the plane $x = 0.5$ of mesh 1. 31

Figure 10 Projected fields on mesh 1 (facet elements). 33

Figure 11 Divergence of the projected fields on mesh 1 (facet elements). 33

Figure 12 Three quadrature points (green stars) taken with respect to one target triangular element (red). 36

Figure 13 Meshes used: M1 (58k elements) and M2 (4k elements). 37

Figure 14 Geometry of the studied example. S is the clipping plane used to illustrate the result. 42

Figure 15 M1-to-M2 projected $\mathbf{H}_t$ (A/m) field on iron core 1 (on a clipping plane), using: (a) $\mathbf{L}^2(\mathscr{D})$-projection. (b) Energetic projection. 43

Figure 16 Distribution of $\mathbf{B}_t$ (T) on a clipping plane, calculated from the projected $\mathbf{H}_t$ fields (Figure 15). (a) $\mathbf{L}^2(\mathscr{D})$-projection. (b) Energetic projection. 43

Figure 17 Magnetic forces (N) on iron core 2. They are calculated by applying the virtual work method on the projected $\mathbf{H}_t$ field using the energetic formulation. 44

Figure 18 Eddy current density (A/m^2) in the two iron cores. This is calculated from the "energetically" projected $\mathbf{H}_t$ field. 45

Figure 19 Energetic error norms to be minimized for $\mathbf{H}$-conform formulations. 46

Figure 20 Mesh used for the studied example. 47

Figure 21 B-H characteristic of the iron circuit used here. 47

Figure 22 Comparison of the $\mathbf{B}_s$ field on the source mesh and the $\mathbf{B}_t$ field on the target mesh. Here the $\mathbf{B}_t$ field is calculated from the "energetically" projected H_t field. 48

Figure 23 Two conductor geometries for the discretization of excitation current densities. The mesh of the bent conductor only contains the conductor. For the twisted conductor, an air box also is used. 53

Figure 24 Discretized current densities, obtained using edge and facet trees (`code_Carmel` v1.7.2). 54

Figure 25 Discretized current densities and their divergence, obtained using full-norm projection methods (bent conductor, clipped). 55

Figure 26 Discretized current densities and their divergence, obtained using full-norm projection methods (twisted conductor). 56

Figure 27 $\mathbf{K}_h$ field and discretized current densities, obtained using the $\mathbf{H}(\mathbf{curl}, \mathscr{D})$ semi-norm projection (98) (bent conductor). 56

Figure 28 $\mathbf{K}_h$ field and discretized current densities, obtained using the $\mathbf{H}(\mathbf{curl}, \mathscr{D})$ semi-norm projection (98) (twisted conductor + air box). 57

Figure 29 Meshes of the cylinder used here. 58

Figure 30 Distribution of the magnetic flux density (T), plotted on a clipping plane. 59

Figure 31 Obtained Von Mises stress (N/m^2) in the cylinder. 60

Figure 32 Magnetic forces (N) on iron core 2. They are calculated by applying the virtual work method on the projected $\mathbf{H}_t$ field using the energetic formulation. 62

Figure 33 Displacement field (m) in iron core 2. Here the left-hand face is attracted by magnetic forces. 62

Figure 34 Von Mises stresses (N/m^2) in iron core 2. 62

Figure 35 Ohmic losses densities (w/m^3) in the two iron cores. They are calculated from the "energetically" projected $\mathbf{H}_t$ field. 63

Figure 36 Evolution of the maximum temperature (°C) versus time (s). 63

Figure 37 Evolution of the distribution of the temperature field T (°C), plotted on a clipping plane of mesh M2. 64

Figure 38 Geometry of the considered electromagnet. 65

Figure 39 Computation strategy using the projection of $\mathbf{B}$. 66

Figure 40 Magnetic forces on the plate and the induced deformations. 66

Figure 41 Meshes used in the magnetic and mechanical models. 72

Figure 42 Computation strategy for the electrical machine. 73

Figure 43 Obtained magnetic flux density (T) at the first time step (Collaboration with R. Fratila). 74

Figure 44 Obtained magnetic forces (N) on the stator (mechanical mesh), calculated from the projected $\mathbf{H}$ field at the first time step. 74

Figure 45 Module of the normal component of the force (N) on node 4899. Plotted as a function of time (above) and the corresponding frequency spectrum (below). 75
Figure 46 Module of the deformation (m) versus frequency (Hz) at node 4899 (collaboration with A. Tan-Kim). 75
Figure 47 Module of the acceleration (m/s^2) versus frequency (Hz) at node 4899 (collaboration with A. Tan-Kim). 76
Figure 48 Distribution of the module of the acceleration filed (m/s^2). 77
Figure 49 Mesh of two triangles. They share a common edge. 84
Figure 50 Whitney functions and bi-orthogonal functions associated with the common edge. 86
Figure 51 Whitney functions and bi-orthogonal functions associated with the common facet. 88

LIST OF TABLES

Table 1 Characteristics of the meshes used. 27
Table 2 Projection errors on mesh 1 (node elements). The target fields are obtained from analytical-to-discrete projections using different methods. 27
Table 3 Projection errors on mesh 2 (node elements), calculated in the analytical-to-discretized projection using different methods. 28
Table 4 Mesh-to-mesh projection errors. The target solution is obtained on mesh 1 (node elements) using different methods. 28
Table 5 Used computation time for mesh1-to-mesh2 projections. 29
Table 6 Projection errors on mesh 1 (edge elements), calculated in the analytical-to-discretized projection using different methods. 30
Table 7 Projection errors on mesh 2 (edge elements), calculated in the analytical-to-discretized projection using different methods. 30
Table 8 Mesh-to-mesh projection errors. The target solution is obtained on mesh 1 (edge elements) using different methods. 32
Table 9 Computation time required for mesh2-to-mesh1 projections. 32
Table 10 Projection errors on mesh 1 (facet elements), calculated with respect to the analytical-to-discretized projection using different methods. 34
Table 11 Computation time required for analytical-to-discrete projections. 34

Table 12 Relative errors of projections (w.r.t. the analytical function), calculated in the continuous-to-discrete projections and the M1-to-M2 projections using different projection techniques. 37

Table 13 Computation time used in the M1-to-M2 projections using different techniques. 38

Table 14 Validation of the energetic projection approach (magneto-static problem). 42

Table 15 Validation of the energetic projection approach (eddy current problem). 44

Table 16 Comparison of the maximum values of $\mathbf{B}_s$ and $\mathbf{B}_t$, for the projections regarding nonlinear magnetic media. 48

Table 17 Comparison with the analytical solution. Here the magnetic and elastic problems are solved on the common mesh. 59

Table 18 Comparison with the analytical solution. Here both meshes are used and the M1-to-M2 projection of $\mathbf{B}$ field is carried out. 60

Table 19 Comparison of the different strategies. (Concerning "$m_\#$ without projection", the magnetic problem is solved on $m_\#$ and the elastic problem is solved on the submesh of $m_\#$ which constitutes the plate.) 68

Table 20 Comparison of implementation techniques in the magneto-mechanical example. The Galerkin projection is applied to the magnetic flux density $\mathbf{B}$. Concerning "$m_\#$ without projection" ($\# = 1, 2$), the magnetic problem is solved on $m_\#$ and the elastic problem is solved on the submesh of $m_\#$ which constitutes the plate. 69

Table 21 Computation time overview for the magneto-mechanical analysis (with a cpu of 2.4GHz single thread). 73

INTRODUCTION

In recent years, greater attention has been paid to studies of multi-physics problems. These studies deal with the interactions between different physical phenomena (electromagnetic - thermal [1, 2, 3, 4], magnetic - mechanical [5, 6, 7, 8, 9, 10, 11, 12], etc.). This is due, not only to the development of industrial applications for new model designs, but also to scientific motivation for accurate modeling of complex systems.

SCOPE AND OBJECTIVES

The work presented in this thesis aims to contribute to finite element analysis of magneto-mechanical and magneto-thermal phenomena.

In electrical machines, magneto-mechanical and magneto-thermal interactions are important sources for mechanical vibrations and temperature rise respectively. In order to meet the growing demand of users regarding the silence and reliability of machines, the understanding and precise modeling of magneto-mechanical and magneto-thermal phenomena has become crucial.

Thanks to modern computers and finite element methods, numerical models have increasingly been used to simulate physical phenomena with great precision. Numerous software packages can be found on the market nowadays to solve electromagnetic, mechanical and thermal problems. Few of them, however, take into account the interactions between different physical phenomena.

In general, multi-physics problems can be treated with different coupling strategies depending on the importance of the internal interaction [7]. In the cases of weak-coupling models, the original problem is divided into subproblems of which the physical nature differs (e. g. electromagnetic, thermal and mechanical problems). The studied domain is thus discretized on different meshes for different subproblems. These subproblems are then solved separately using finite element methods. This strategy is particularly useful for coupled problems with weak interaction, because of the simplicity of its realization.

The model coupling is of crucial importance in such multi-physics problems, in order to ensure the information transmission and the communication between the subproblems. In this work, we study field projection approaches on overlapping domains.

This work has been carried out in Valeo Electrical Systems based in Créteil[1] and at the Laboratory of Electrical Engineering and Power Electronics at Lille[2], both located in France.

---

[1] Valeo, 2 Rue André Boulle, 94000 Créteil, France. http://www.valeo.com/

[2] L2EP, Bât. P2, Université Lille1, 59650 Villeneuve d'ascq, France. http://l2ep.univ-lille1.fr/

This thesis has also been conducted within the "Motors and Electrical Devices for Energy Efficiency" (MEDEE) project.

OUTLINE

This thesis is divided into three chapters.

Chapter 1 presents the computational models we use in this work. After the definition of the hypotheses on which all studies are based, we give a short reminder of the equations governing three models: electromagnetic, mechanical and thermal. The continuous function spaces to which physical fields belong are briefly presented, as well as the complexes they form. The sequence of Whitney elements is then used to construct finite element spaces.

Chapter 2 studies field projection approaches for model coupling. Here projections consist of transferring information from one computational model to another. First, depending on the properties of the field to be projected, projection formulations are developed in different spaces. Ritz-Galerkin as well as Petrov-Galerkin methods are used to apply test functions. Second, we present two implementation techniques in order to carry out mesh-to-mesh projections in practice. They are compared in terms of accuracy, speed and simplicity of realization. Third, we propose energetic formulations for the projection of electromagnetic fields. Energy-conserving projections ensure greater accuracy in magneto-mechanical and magneto-thermal calculations. For all three sections, numerical examples are presented in order to support theoretical studies.

Chapter 3 highlights several applications of field projections, to the discretization of analytical fields and the computation of magneto-mechanical and magneto-thermal problems. For multi-physics problems we focus on the projection of electromagnetic fields between different computational models. The result of electromagnetic computation is projected onto different meshes for downstream calculations (e. g. mechanical and thermal). In this chapter, we study a magneto-mechanical example for which the analytical solution is given. We also describe more common examples in electrical engineering, such as electromagnets and electrical machines.

1

COMPUTATIONAL MODELS

In the case of small deformations, we assume that mechanical deformations have no influence on the distribution of electromagnetic fields. For mechanical problems, constitutive laws are considered to be independent from electromagnetic fields. Under these conditions, a magneto-mechanical model is presented using two separate submodels: an electromagnetic model and a mechanical model.

Similarly, thermal time constants are in general much greater than electromagnetic wave periods. Electromagnetic constitutive laws can be considered to be stable while evaluating electromagnetic fields for a specific period (i. e. not depending on time or temperature variations). A magneto-thermal model is thus divided into an electromagnetic model and a thermal model.

In this chapter, we first define the problems to be solved with electromagnetic, mechanical and thermal models. Second, the continuous function spaces to which physical fields belong, as well as the complexes they form, are briefly presented. Third, the definition of Whitney elements is given. They are now widely used in finite element analysis.

1.1 ELECTROMAGNETIC MODEL

The first model we present is the electromagnetic model. Given an electromagnetic system, the electromagnetic model deals with the mathematical modeling of electromagnetic fields.

1.1.1 *Continuous problem*

Let us consider a domain Θ with regular boundary $\partial\Theta$ for the magnetic study. In the area of electrical engineering, Θ can be composed of air, magnetic materials, conductors and magnetic sources such as excitation currents and permanent magnets (Figure 1).

Maxwell's equations

Mathematically, electromagnetic problems to be solved are presented using Maxwell's equations:

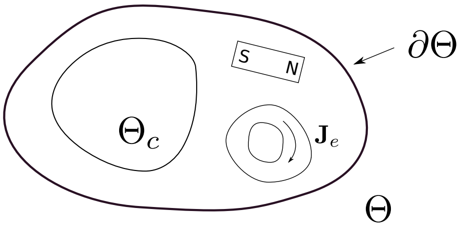

Figure 1: Study domain for electromagnetic models.

$$\textbf{curl } \mathbf{E} = -\partial_t \mathbf{B} \tag{1a}$$

$$\textbf{curl } \mathbf{H} = \mathbf{J} + \partial_t \mathbf{D} \tag{1b}$$

$$\text{div } \mathbf{D} = q \tag{1c}$$

$$\text{div } \mathbf{B} = 0 \tag{1d}$$

Equations (1a), (1b), (1c) and (1d) represent respectively the Faraday's law, the generalized Ampère's law, the electric Gauss's law and the magnetic Gauss's law. The five vector fields **E**, **H**, **J**, **B** and **D** are respectively the electric field (V/m), the magnetic field (A/m), the electric current density (A/m^2), the magnetic flux density (T) and the electric displacement field (C/m^2). q is the electric charge density (C/m^3) and ∂_t is the time derivative operator.

We should note that, (1b) together with (1c), imply the equation of the conservation of electric charges:

$$\text{div } \mathbf{J} + \partial_t q = 0 \tag{2}$$

In the area of electrical engineering, at low frequency, the time-derivative of the displacement current density (the $\partial_t \mathbf{D}$ term in (1b)) is usually assumed to be neglectable. In this case, (1b) is replaced by:

$$\textbf{curl } \mathbf{H} = \mathbf{J} \tag{3}$$

This assumption is justifiable when the wavelength of electromagnetic fields is much greater than the characteristic size of the studied domain. Physically, this means propagation phenomena are not taken into account. Under this condition, the current density is divergence-free:

$$\text{div } \mathbf{J} = 0 \tag{4}$$

Constitutive laws

The different materials in the study domain impact on the relations between electromagnetic fields. This impact is described by constitutive laws. In this work, only homogeneous medias are considered.

The first constitutive law we adopt is Ohm's law, valid for conductors:

$$\mathbf{J} = \sigma \mathbf{E} \tag{5}$$

where σ is the electrical conductivity (S/m).

The second constitutive law expresses the relation between the magnetic flux density and the magnetic field:

$$\mathbf{B} = \mu \mathbf{H} + \mathbf{B}_r \tag{6}$$

where μ is the magnetic permeability (H/m) and $\mathbf{B}_r$ is the remanent induction (T).

In this work, $\mathbf{B}_r$ is used to take permanent magnets into account. For other media, $\mathbf{B}_r = \mathbf{0}$.

For ferromagnetic materials, the magnetic permeability μ is in general non-linear and depends on the module of the magnetic field, i. e. $\mathbf{B} = \mu(H)\mathbf{H}$. In the linear working area of the such materials, the non-linear **B**-**H** characteristics can be approximated with straight lines. For other cases, non-linear models should be used [13].

Boundary conditions

The above Maxwell's equations (1) as well as the constitutive laws (5) and (6) form a differential problem. This problem is completed with boundary conditions. From a mathematical point of view, boundary conditions ensure the unicity of the solution for a studied problem.

Regarding temporal boundary conditions, the values of electromagnetic fields are usually assumed to be zero at the starting point.

For spatial boundary conditions, the boundary of the studied domain $\partial\Theta$ is decomposed into two parts: $\Gamma_{\mathbf{H}}$ for the boundary condition with respect to the magnetic field and $\Gamma_{\mathbf{B}}$ for the magnetic flux density. Thus we have $\Gamma_{\mathbf{H}} \cup \Gamma_{\mathbf{B}} = \partial\Theta$ and $\Gamma_{\mathbf{H}} \cap \Gamma_{\mathbf{B}} = \emptyset$. Let the field of outward directed normal unit vectors be denoted by $\mathbf{n}$. The boundary conditions with respect to magnetic quantities can be expressed as follows:

$$\mathbf{n} \times \mathbf{H}|_{\Gamma_{\mathbf{H}}} = \mathbf{0} \tag{7a}$$

$$\mathbf{n} \cdot \mathbf{B}|_{\Gamma_{\mathbf{B}}} = 0 \tag{7b}$$

Similarly, for the conducting subdomain Θ_c with the boundary $\partial\Theta_c = \Gamma_{\mathbf{E}} \cup \Gamma_{\mathbf{J}}$, the boundary conditions with respect to electric quantities can be defined as follows:

$$\mathbf{n} \times \mathbf{E}|_{\Gamma_{\mathbf{E}}} = \mathbf{0} \tag{8a}$$

$$\mathbf{n} \cdot \mathbf{J}|_{\Gamma_{\mathbf{J}}} = 0 \tag{8b}$$

In the case where the conducting domain Θ_c shares a boundary with the study domain Θ (i. e. $\partial\Theta_c \cap \partial\Theta \neq \emptyset$), at the intersecting boundary we have the following relations:

- $\mathbf{n} \times \mathbf{E} = \mathbf{0}$ implies $\mathbf{n} \cdot \mathbf{B} = 0$ because of (1a)
- $\mathbf{n} \times \mathbf{H} = \mathbf{0}$ implies $\mathbf{n} \cdot \mathbf{J} = 0$ because of (3)

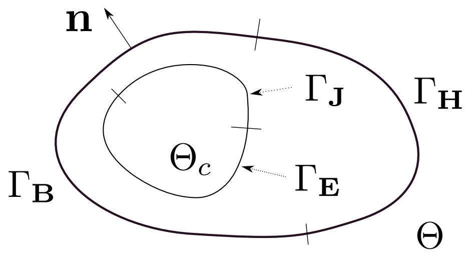

Figure 2: Boundary conditions for electromagnetic models.

1.1.2 *Potential formulations*

The Maxwell's equations can be directly solved using field formulations. Potential formulations are however more convenient for taking into account transmission conditions at the interfaces of different media [14]. In this part, potential formulations for both magneto-static and magneto-dynamic problems are presented. We note that, gauge conditions must be added in order to ensure the unicity of the solution in the case of potential formulations.

1.1.2.1 *Magneto-static problems*

In the case of magneto-static problems, the equations to be solved are:

$$\begin{cases} \mathbf{curl}\ \mathbf{H} = \mathbf{J}_e \\ div\ \mathbf{B} = 0 \end{cases} \tag{9}$$

As no induced current is presents in static problems, here the current density (the **J** term in Ampère's law (3)) is replaced by $\mathbf{J}_e$, which stands for a given stable excitation current density. In this work we restrict ourselves to the case of homogeneous excitation current densities.

If present, permanent magnets are also sources of magnetic fields: $\mathbf{B} = \mu\mathbf{H} + \mathbf{B}_r$.

Two potential formulations can be employed for magneto-static problems: the **A** formulation and the Ω formulation. They focus on the differential equations of the magnetic field and the magnetic flux density respectively.

A *formulation*

Since $div\ \mathbf{B} = 0$, we can derive the magnetic flux density **B** from a vector potential **A** such that

$$\mathbf{B} = \mathbf{curl}\ \mathbf{A} \tag{10}$$

As a consequence, the problem to be solved (9) can be expressed as:

$$\mathbf{curl}\ (\frac{1}{\mu}\mathbf{curl}\ \mathbf{A}) = \mathbf{J}_e + \mathbf{curl}\ (\frac{1}{\mu}\mathbf{B}_r) \tag{11}$$

Different gauge conditions can be used in order to ensure the unicity of **A**. In this work, the finite element methods are used for discretization and the conjugate gradient method for solving the linear systems. This implies implicitly Coulomb's gauge [15]: $div\ \mathbf{A} = 0$.

Ω formulation

Another possibility for solving magneto-static problems is to employ a scalar potential formulation. We can decompose the magnetic field **H** into two components: the excitation part $\mathbf{H}_e$ and the reaction part $(\mathbf{H} - \mathbf{H}_e)$, such that:

$$\mathbf{curl}\ \mathbf{H}_e = \mathbf{J}_e \tag{12a}$$

$$\mathbf{curl}\ (\mathbf{H} - \mathbf{H}_e) = \mathbf{0} \tag{12b}$$

Hence we can derive the reaction part $(\mathbf{H} - \mathbf{H}_e)$ from a scalar potential Ω such that:

$$\mathbf{H} = \mathbf{H}_e - \mathbf{grad}\ \Omega \tag{13}$$

The problem to be solved (9) can then be expressed as:

$$div\ (\mu \mathbf{grad}\ \Omega) = div\ (\mu \mathbf{H}_e + \mathbf{B}_r) \tag{14}$$

In practice, fixing the value of Ω at the boundary $\Gamma_\mathbf{H}$ gauges the problem. If $\Gamma_\mathbf{H} = \emptyset$, the average value of Ω can be used, e. g. fixing $\int_\Theta \Omega = 0$.

1.1.2.2 *Magneto-dynamic problems*

Magneto-dynamic models consist of studying time-dependent electromagnetic phenomena. With the time-derivative of the displacement current density neglected, the equations to be solved are:

$$\begin{cases} \mathbf{curl}\ \mathbf{E} = -\partial_t \mathbf{B} \\ \mathbf{curl}\ \mathbf{H} = \mathbf{J} \\ div\ \mathbf{B} = 0 \end{cases} \tag{15}$$

Similar to the static case, two formulations can be used: the $\mathbf{A} - \phi$ formulation and the $\mathbf{T} - \Omega$ formulation.

$\mathbf{A} - \phi$ *formulation*

Since $div\ \mathbf{B} = 0$, we can, as in magneto-statics, derive the magnetic flux density **B** from a vector potential **A** such that $\mathbf{B} = \mathbf{curl}\ \mathbf{A}$ in Θ.

We can thus deduce the following relation:

$$\mathbf{curl}\ (\mathbf{E} + \partial_t \mathbf{A}) = \mathbf{0} \tag{16}$$

Equation (16) leads to the definition of a scalar electric potential ϕ in the conducting domain Θ_c such that

$$\mathbf{E} = -\partial_t \mathbf{A} - \mathbf{grad}\ \phi \tag{17}$$

Using the definitions of $\mathbf{A}$ and ϕ, the magnetic field $\mathbf{H}$ and the induced current density $\mathbf{J}_{ind}$ in the conducting domain can be expressed as:

$$\mathbf{H} = \frac{1}{\mu}(\mathbf{curl}\ \mathbf{A} - \mathbf{B}_r) \text{ and } \mathbf{J}_{ind} = -\sigma(\partial_t \mathbf{A} + \mathbf{grad}\ \phi) \tag{18}$$

Thus the problem to be solved (15) can be expressed in the following form:

$$\begin{cases} \mathbf{curl}\ (\frac{1}{\mu}\mathbf{curl}\ \mathbf{A}) + \sigma(\partial_t \mathbf{A} + \mathbf{grad}\ \phi) = \mathbf{J}_e + \mathbf{curl}\ (\frac{1}{\mu}\mathbf{B}_r) \text{ in } \Theta \\ \text{div}\ (\sigma(\partial_t \mathbf{A} + \mathbf{grad}\ \phi)) = 0 \text{ in } \Theta_c \end{cases} \tag{19}$$

$\mathbf{T} - \Omega$ *formulation*

As we have presented in the magneto-static case, a field $\mathbf{H}_e$ can be defined such that $\mathbf{J}_e = \mathbf{curl}\ \mathbf{H}_e$ in Θ. The reaction part is thus curl-free: $\mathbf{curl}\ (\mathbf{H} - \mathbf{H}_e) = \mathbf{0}$. Moreover, in the conducing domain, since the divergence of the induced current density $\mathbf{J}_{ind}$ is null, a vector potential denoted by $\mathbf{T}$ can be introduced such that $\mathbf{J}_{ind} = \mathbf{curl}\ \mathbf{T}$.

Using the scalar potential Ω over the entire study domain and the vectorial potential $\mathbf{T}$ which only appears in conductors, the magnetic field $\mathbf{H}$ can be defined as a piecewise function:

$$\mathbf{H} = \begin{cases} \mathbf{H}_e - \mathbf{grad}\ \Omega \text{ in } \Theta_{nc} \\ \mathbf{H}_e + \mathbf{T} - \mathbf{grad}\ \Omega \text{ in } \Theta_c \end{cases} \tag{20}$$

where Θ_{nc} describes the non-conducting domain.

In this case, the problem to be solved (15) can be expressed as follows:

$$\begin{cases} \mathbf{curl}\ (\frac{1}{\sigma}\mathbf{curl}\ \mathbf{T}) + \partial_t(\mu(\mathbf{T} - \mathbf{grad}\ \Omega)) = -\partial_t(\mu \mathbf{H}_e) \text{ in } \Theta_c \\ \text{div}\ (\mu(\mathbf{T} - \mathbf{grad}\ \Omega)) = -\text{div}\ (\mu \mathbf{H}_e + \mathbf{B}_r) \text{ in } \Theta_c \\ \text{div}\ (\mu \mathbf{grad}\ \Omega) = \text{div}\ (\mu \mathbf{H}_e + \mathbf{B}_r) \text{ in } \Theta_{nc} \end{cases} \tag{21}$$

As in the magneto-static case, gauge conditions have to be defined in order to select one of the possible potential solutions.

1.2 MECHANICAL MODEL

The second computational model we present is the mechanical model. In this work, mechanical problems are only considered as downstream models for electromagnetic computations. The coupling terms between the two models are magnetic forces. These forces are calculated from magnetic models and used as source terms for mechanical models.

Thus we focus on the deformations and the vibrations caused by electromagnetic origins. Under the assumption of small deformations, we restrict ourselves to the case of linear elasticity [16, 17].

1.2.1 *Continuous problem*

Let Λ be a smooth and connected domain, which is identified with the solid body of interest at the starting point. In the case of linear elasticity, we assume that all deformations are small such that a linearization of the strain tensor is justifiable.

Governing equations

A linear elastic boundary value problem is based on the balance equation of linear momentum (22a) and the infinitesimal relation between strain and displacement (22b):

$$\rho\ \partial_t^2 \mathbf{u} = \mathbf{div}\ \boldsymbol{\tau} + \mathbf{f} \tag{22a}$$

$$\varepsilon = \frac{1}{2}\left[\mathbf{grad}\ \mathbf{u} + (\mathbf{grad}\ \mathbf{u})^T\right] \tag{22b}$$

where ρ is the mass density ($\mathrm{kg/m^3}$), $\mathbf{u}$ is the displacement field (m), $\mathbf{f}$ is the volume force density ($\mathrm{N/m^3}$), $\boldsymbol{\tau}$ is the 3x3 stress tensor ($\mathrm{N/m^2}$) and ε is the 3x3 strain tensor (dimensionless). $\partial_t^2 \mathbf{u}$ signifies the second-order time-derivative of the displacement, i. e. the acceleration ($\mathrm{m/s^2}$).

Constitutive law

Material law for linear elasticity, which states the relation between the strain and the stress tensor, is described by Hooke's law.

For isotropic homogeneous medias, we often use Young's modulus E ($\mathrm{N/m^2}$) and Poisson's ratio ν (dimensionless) to characterize different materials. The relation between stress and strain can be expressed as:

$$\boldsymbol{\tau} = \frac{E}{1+\nu}\left[\varepsilon + \frac{\nu}{1-2\nu}\mathrm{Tr}(\varepsilon)\mathbf{I}\right] \tag{23}$$

where $\mathrm{Tr}(\varepsilon)$ is the trace of the strain tensor and $\mathbf{I}$ is a 3x3 identity tensor. Physically, sensible values of E and ν vary as follows: $E > 0$ and $0 < \nu < 1/2$.

Boundary conditions

As for electromagnetic models, we add suitable conditions with respect to the stress and displacement fields at the boundary of the studied domain $\partial\Lambda$. Correctly chosen conditions ensure that the equations of elasticity have an unique set of solutions.

If the studied body is fixed along at least a part of its boundary, the deformations and stresses can be uniquely determined because no rigid body motions can occur. Otherwise, the solution can only be unique up to such rigid body motions which do not affect the strains and stresses inside.

We can divide the boundary $\partial\Lambda$ into two parts: $\partial\Lambda = \Gamma_{\mathbf{u}} \cup \Gamma_{\boldsymbol{\tau}}$. These two parts shall not intersect: $\Gamma_{\mathbf{u}} \cap \Gamma_{\boldsymbol{\tau}} = \emptyset$.

The boundary conditions for linear elasticity can then be expressed as follows:

$$\mathbf{u}|_{\Gamma_{\mathbf{u}}} = \mathbf{u}_0 \tag{24a}$$

$$\boldsymbol{\tau}\,\mathbf{n}|_{\Gamma_{\tau}} = \mathbf{t}_0 \tag{24b}$$

Equation (24a) is a Dirichlet boundary condition, i. e. we fix the displacement $\mathbf{u}$ to some given surface displacement $\mathbf{u}_0$. On the remaining boundary $\Gamma_{\boldsymbol{\tau}}$, (24b) describes the given surface traction $\mathbf{t}_0$.

1.2.2 *Displacement formulations*

A very common formulation in order to solve linear elastic problems is the displacement formulation.

The strains and stresses are eliminated, leaving the displacements as the unknowns to be solved:

$$\frac{E}{2(1+\nu)}\mathbf{div}(\mathbf{grad}\ \mathbf{u}) + \frac{E}{2(1+\nu)(1-2\nu)}\mathbf{grad}(\mathrm{div}\ \mathbf{u}) + \mathbf{f} = \rho\ \partial_t^2\mathbf{u} \tag{25}$$

If no other countervailing forces act in the interior of the material and the material is in a static state, the force density must vanish throughout the materials interior due to Newton's law. Equation (22a) becomes:

$$\mathbf{div}\ \boldsymbol{\tau} + \mathbf{f} = \mathbf{0} \tag{26}$$

In this case, the displacement formulation for static linear elastic problems is:

$$\frac{E}{2(1+\nu)}\mathbf{div}(\mathbf{grad}\ \mathbf{u}) + \frac{E}{2(1+\nu)(1-2\nu)}\mathbf{grad}(\mathrm{div}\ \mathbf{u}) + \mathbf{f} = \mathbf{0} \tag{27}$$

This equation is called the Navier-Cauchy equation.

1.3 THERMAL MODEL

Another computational model we use in this work is the thermal model. Similar to the mechanical model, the thermal model is only considered as a downstream model for electromagnetic computations. In the domain of electrical engineering, the electromagnetic wave period is usually much smaller than the time for temperature variation (i. e. thermal time constants). The copper losses and iron losses issued from electromagnetic phenomena and accumulated in periods, can thus be used as source terms for the thermal model.

For simplicity, here we restrict ourselves to the problems of heat conduction [18, 19].

1.3.1 *Continuous problem*

Let us consider a domain Π for the thermal study. Its boundary $\partial\Pi$ is regular.

Heat conduction is a transfer mode driven by a temperature difference between two regions of the same medium, or between two media in contact. However, unlike the process of heat convection, no displacement of material is present in the macroscopic scale.

Governing equations

The balance of the heat energy, which describes the relation between the heat source and the time-derivative of the temperature, is governed by the following equation:

$$\mathrm{div}\,\mathbf{Q} + p = \rho C \partial_t T \tag{28}$$

where $\mathbf{Q}$ is the heat flux density (w/m^2), p is the volume heat source (w/m^3), ρ is the mass density (kg/m^3), C is the specific heat capacity ($J/(kg \cdot K)$) and T is the temperature (K).

Constitutive law

The law of heat conduction, also known as Fourier's law, states the relation between the heat flux density and the negative gradient of the temperature field:

$$\mathbf{Q} = -k\,\mathbf{grad}\,T \tag{29}$$

where k is the thermal conductivity ($W/(m \cdot K)$).

Boundary conditions

Regarding the temporal boundary conditions of thermal problems, an initial temperature distribution can be imposed depending on the environment.

Three types of spacial boundary conditions can then be used at the boundary $\partial\Pi$.

$$T|_{\Gamma_T} = T_0 \tag{30a}$$
$$\mathbf{n} \cdot \mathbf{Q}|_{\Gamma_Q} = \mathbf{Q}_0 \tag{30b}$$
$$\mathbf{n} \cdot \mathbf{Q}|_{\Gamma_e} = C_e(T_e - T) \tag{30c}$$

Here Γ_T, Γ_Q and Γ_e denote the boundaries with respect to specified temperatures T_0, specified heat flux densities $\mathbf{Q}_0$ and convection heat transfer respectively. In the case of the convection heat transfer boundary, C_e is the heat transfer coefficient and T_e is the environment temperature.

1.3.2 *Temperature formulations*

The balance of the heat energy (28), together with Fourier's law (29) and the boundary conditions (30), characterize the problem to be solved under thermal conductions. We can eliminate the heat flux density in these equations, leaving the distribution of temperature governed by the following equation:

$$-\mathrm{div}\,(k\,\mathbf{grad}\,T) + p = \rho C \partial_t T \tag{31}$$

For steady-state cases, the T field is no longer a function of time. Thus no initial condition is needed, and the governing equation is simplified to:

$$-\mathrm{div}\,(k\,\mathbf{grad}\,T) + p = 0 \tag{32}$$

1.4 FUNCTIONAL FRAMEWORK

We can now set up our framework for the three computational models.

Different functional spaces can be defined in order to host the physical quantities presented. These spaces are used later in the discretization process (Section 1.5) and the field projection (Chapter 2).

For an open connected domain $\mathscr{D} \subset \mathbb{R}^3$, let $L^2(\mathscr{D})$ and $\mathbf{L}^2(\mathscr{D})$ be the spaces of square integrable scalar and vectorial functions respectively:

$$L^2(\mathscr{D}) = \left\{ f, \int_{\mathscr{D}} | f |^2 < +\infty \right\} \tag{33a}$$

$$\mathbf{L}^2(\mathscr{D}) = \left\{ \mathbf{f}, \int_{\mathscr{D}} | \mathbf{f} |^2 < +\infty \right\} \tag{33b}$$

$L^2(\mathscr{D})$ and $\mathbf{L}^2(\mathscr{D})$ are basic spaces for physical fields, which are characterized by a finite energy.

We can also introduce the subspaces $H(\mathbf{grad}, \mathscr{D})$, $\mathbf{H}(\mathbf{curl}, \mathscr{D})$ and $\mathbf{H}(\mathrm{div}, \mathscr{D})$ associated with the three fundamental operators **grad**, **curl**, and div [20]:

$$H(\mathbf{grad}, \mathscr{D}) = \left\{ f \in L^2(\mathscr{D}), \mathbf{grad}\, f \in \mathbf{L}^2(\mathscr{D}) \right\} \tag{34a}$$

$$\mathbf{H}(\mathbf{curl}, \mathscr{D}) = \left\{ \mathbf{f} \in \mathbf{L}^2(\mathscr{D}), \mathbf{curl}\, \mathbf{f} \in \mathbf{L}^2(\mathscr{D}) \right\} \tag{34b}$$

$$\mathbf{H}(\mathrm{div}, \mathscr{D}) = \left\{ \mathbf{f} \in \mathbf{L}^2(\mathscr{D}), \mathrm{div}\, \mathbf{f} \in L^2(\mathscr{D}) \right\} \tag{34c}$$

where the first-order derivatives are also square integrable.

These spaces provide the environment for physical quantities in electromagnetic, mechanical and thermal models.

For instance, the electromagnetic quantities in the Maxwell's equations (1) and the potentials we have previously defined in Section 1.1.2, can be hosted in different spaces:

- $\Omega, \phi \in H(\mathbf{grad}, \mathscr{D})$
- $\mathbf{E}, \mathbf{H}, \mathbf{A}, \mathbf{T} \in \mathbf{H}(\mathbf{curl}, \mathscr{D})$
- $\mathbf{B}, \mathbf{J} \in \mathbf{H}(\mathrm{div}, \mathscr{D})$

Since $\mathbf{grad}\; H(\mathbf{grad}, \mathscr{D}) \subset \mathbf{H}(\mathbf{curl}, \mathscr{D})$, $\mathbf{curl}\; \mathbf{H}(\mathbf{curl}, \mathscr{D}) \subset \mathbf{H}(\mathrm{div}, \mathscr{D})$ and $\mathrm{div}\; \mathbf{H}(\mathrm{div}, \mathscr{D}) \subset L^2(\mathscr{D})$, the spaces $H(\mathbf{grad}, \mathscr{D})$, $\mathbf{H}(\mathbf{curl}, \mathscr{D})$, $\mathbf{H}(\mathrm{div}, \mathscr{D})$ and $L^2(\mathscr{D})$ form a complex:

$$H(\mathbf{grad}, \mathscr{D}) \xrightarrow{\mathbf{grad}} \mathbf{H}(\mathbf{curl}, \mathscr{D}) \xrightarrow{\mathbf{curl}} \mathbf{H}(\mathrm{div}, \mathscr{D}) \xrightarrow{\mathrm{div}} L^2(\mathscr{D}) \tag{35}$$

which is usually called the de Rham complex.

In the case of regular bounded domains, the image of $H(\mathbf{grad},\mathscr{D})$ in $\mathbf{H}(\mathbf{curl},\mathscr{D})$ by the **grad** is the kernel of the **curl** operator, which means that all curl-free fields can be expressed as gradients. Moreover, the image of $\mathbf{H}(\mathbf{curl},\mathscr{D})$ in $\mathbf{H}(\mathrm{div},\mathscr{D})$ by **curl** is the kernel of the div operator, i. e. all divergence-free fields can be expressed as curls.

A basic continuous structure, which is often called "Maxwell's house", can be formed by four de Rham complexes [14]. In Figure 3, two de Rham complexes (35) are placed on the left (top to bottom), another two on the right (bottom to top). This symmetry reflects the symmetry of Maxwell's equations. The two complexes on each side are linked by the time-derivative. The horizontal beams, which link the left and right sides, signify the constitutive laws.

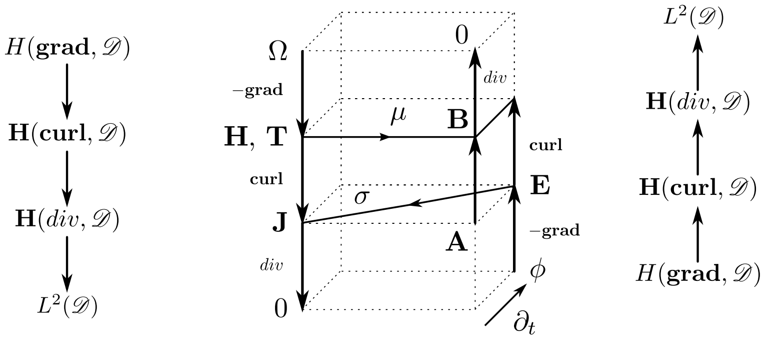

Figure 3: Maxwell's house.

For the displacement formulations with respect to linear elasticity (Section 1.2.2), the displacement field is sought in the Sobolev space $[H(\mathbf{grad},\mathscr{D})]^3$. The stress tensor is eliminated in these formulations, as it can be expressed in terms of the displacement field. We refer to [8] for a functional-framework "house" concept in strong-coupling magneto-mechanical problems.

Regarding the thermal model, the temperature formulation (Section 1.3.2) is very similar to the Ω-formulation of the static magnetic model. $H(\mathbf{grad},\mathscr{D})$, $\mathbf{H}(\mathrm{div},\mathscr{D})$ and $L^2(\mathscr{D})$ are respectively the natural spaces for the temperature field, the heat flux density and the volume heat source.

1.5 FINITE ELEMENT METHODS

The electromagnetic, mechanical and thermal models can be analytically solved in the case of simple geometries. For complex systems, they can be numerically calculated thanks to computer technologies.

Among the different numerical methods (e. g. boundary element method, finite integration technique, natural element method, etc. [21, 22, 23, 24]), finite element methods (FEM) are nowadays widely used in both research and industrial domains of engineering. The general idea is to weaken continuous formulations to a discrete subspace, and solve the corresponding finite-dimensional problem. In particular, using finite element methods, the discretized subspaces are piece-wise defined on an union of geometrical elements. Whitney elements [25, 26, 14] have been proven to provide a sound discretization basis for finite element analysis.

Let us consider a tetrahedral mesh of the domain $\mathscr{D}$. We denote by $\mathscr{N}$, $\mathscr{E}$, $\mathscr{F}$ and $\mathscr{T}$ the sets of simplices of dimension 0 to 3, i. e. nodes, edges, facets, and tetrahedra respectively. The Whitney functions for each simplex are defined as follows:

- **Node:** For each node $n_i \in \mathscr{N}$, a nodal linear function w_i^n is associated. At point x, if x is not located in a tetrahedron connected to n_i, the value of w_i^n is zero. Otherwise, its value is equal to the barycentric coordinate of x with respect to n_i in the tetrahedral volume.

- **Edge:** For an edge $e_i \in \mathscr{E}$ constructed by two nodes n_a and n_b, a vectorial function is associated:

$$\mathbf{w}_i^e = w_a^n \,\mathbf{grad}\, w_b^n - w_b^n \,\mathbf{grad}\, w_a^n \tag{36}$$

- **Facet:** Similarly, for a triangular facet $f_i \in \mathscr{F}$ constructed by nodes n_a, n_b and n_c:

$$\begin{aligned}\mathbf{w}_i^f =& 2(w_a^n \,\mathbf{grad}\, w_b^n \times \mathbf{grad}\, w_c^n + w_b^n \,\mathbf{grad}\, w_c^n \times \mathbf{grad}\, w_a^n \\ &+ w_c^n \,\mathbf{grad}\, w_a^n \times \mathbf{grad}\, w_b^n)\end{aligned} \tag{37}$$

- **Tetrahedra:** Finally, the volume Whitney function for each tetrahedron $t_i \in \mathscr{T}$ is scalar. Its value is equal to $1/\mathrm{vol}(t_i)$ in the same tetrahedron and zero elsewhere. Here $\mathrm{vol}(t_i)$ is the volume of the i-th tetrahedron.

Therefore, every simplex of dimension 0 to 3 is associated with a scalar or vectorial field. All these fields together are the Whitney elements. Some of their main properties can be highlighted as follows:

- The sum of all nodal functions is equal to 1 over the entire domain, i. e. $\sum_{n_i \in \mathscr{N}} w_i^n = 1$.
- The circulation of an edge function is equal to 1 along the same edge, i. e. $\int_{e_i} \mathbf{w}_i^e = 1$.
- The flux of a facet function is equal to 1 across the same facet, i. e. $\int_{f_i} \mathbf{w}_i^f = 1$.
- The integral of a volume function is equal to 1 in the same tetrahedron, i. e. $\int_{t_i} w_i^t = 1$.

The Whitney elements provide great closeness when compared to the nature of physical fields:

* The Whitney nodal element is continuous. It is well suited for the discretization of a field with finite gradient (e. g. the scalar potentials in electromagnetic models, the displacement field in the mechanical model, the temperature field in the thermal model, etc.). Given the punctual evaluation of a field at these nodes, these values can be used as weights (called degrees of freedom) for the nodal functions.

- For the edge and facet elements, their tangential or normal components match at the boundary of different tetrahedrons. They provide great conformity for the discretization of vector fields of which the tangential or normal components are continuous across material interfaces.

  For instance, the electric and magnetic fields or the vectorial potentials can be better discretized at edges than other elements. A facet element is more suitable for the magnetic flux density, the current density and the heat flux density. In these cases, their degrees of freedom are the circulations along the edges and the fluxes across the faces for edges and facets respectively.

- The Whitney volume element is constant in each tetrahedron. This makes it a suitable target for the discretization of volume densities, e. g. the density of electric charge, magnetic energy or joule heating.

Thanks to their continuous properties, the Whitney elements supply discretized subspaces for the spaces $H(\mathbf{grad}, \mathscr{D})$, $\mathbf{H}(\mathbf{curl}, \mathscr{D})$, $\mathbf{H}(\mathrm{div}, \mathscr{D})$ and $L^2(\mathscr{D})$. If we define the size h for the largest radius of the element circumsphere of the mesh used, the corresponding "h-discretized" spaces are noted as: $H_h(\mathbf{grad}, \mathscr{D})$, $\mathbf{H}_h(\mathbf{curl}, \mathscr{D})$, $\mathbf{H}_h(\mathrm{div}, \mathscr{D})$ and $L^2_h(\mathscr{D})$.

As noted previously with respect to the different computational models, the problems to be solved can be generalized in the following form: find a field (scalar or vectorial) $u \in U$ such that

$$A(u) = f \tag{38}$$

For instance, u can be the magnetic potentials, the displacement, the temperature, etc.

Equation (38) is equivalent to its weak formulation, namely: find $u \in U$ such that

$$a(u, \psi) = l(\psi), \ \forall \psi \in U \tag{39}$$

where $a(\cdot, \cdot)$ is a bilinear form and $l(\cdot)$ is a linear form. Here ψ is called a test function.

With Whitney elements, u is discretized into the corresponding "h-discretized" space U_h:

$$u_h = \sum_i w_i x_i \tag{40}$$

where w_i are the corresponding Whitney functions and x_i are the degrees of freedom.

The obtained Galerkin equation is presented by: find $u_h \in U_h$ such that

$$a(u_h, \psi_h) = l(\psi_h), \ \forall \psi_h \in U_h \tag{41}$$

Equation (41) produces a linear system of equations, which can be presented in matrix forms. The degrees of freedom can thus be solved thanks to numerical solvers.

2

MODEL COUPLING

In the domain of finite element analysis, computational models such as the electromagnetic, mechanical and thermal models, are very often solved with respect to their specific regions of interest and their efficient discretization. To obtain a precise computational result for the entire coupled magneto-mechanical or magneto-thermal problem, a common mesh should take all the particulars of the subproblems into account. Another solution is to carry out the computations on different meshes: in this case the information transmission and the communication between the subproblems are of crucial importance. In this work we are interested in field projection approaches on overlapping domains.

Furthermore, we concentrate on Whitney elements which were previously presented in Section 1.5. Whitney shape functions associated with coefficients (called degrees of freedom) are used for the field discretization. The field projection methods consist of the numerical computation of the degrees of freedom from a given solution. The proposed projection methods can be applied to mesh-to-mesh field transmission or to the imposition of analytical source fields.

In this chapter, we first present general projection formulations in order to transfer fields between different meshes. Second, implementation techniques are studied with respect to practice considerations. Third, energetic formulations are given for the projection of electromagnetic fields.

2.1 PROJECTION FORMULATIONS

In the literature, the basic projection idea is not new. Similar applications can also be found in domain decomposition methods [27, 28, 29, 30, 31, 32, 33, 34]. In this work the L^2 or $\mathbf{L}^2$ projection theory is extended to the subspaces $\mathrm{H}(\mathbf{grad})$, $\mathbf{H}(\mathbf{curl})$ and $\mathbf{H}(\mathrm{div})$. These extensions of projection theory allow greater accuracy for the derivatives. A Petrov-Galerkin method using local bi-orthogonal test functions is then presented.

This section is organized as follows: first, we give a brief reminder of the spaces used to host physical quantities. Second, we define the problem to be solved using field projection and give the corresponding weak formulations. In comparison with the literature, the formulations introduced are also applied to the subspaces $\mathrm{H}(\mathbf{grad})$, $\mathbf{H}(\mathbf{curl})$ and $\mathbf{H}(\mathrm{div})$. Third, the classical Ritz-Galerkin method is recalled and a Petrov-Galerkin method using the local bi-orthogonal test functions is presented. Using the Petrov-Galerkin method and bi-orthogonal test functions, the projection is presented using a diagonal matrix. However, in the standard Ritz-Galerkin projections, a linear system must be solved. In order to highlight some applications of the projection methods, numerical results are then presented for all Whitney element types. In particular, the projection error will be given using the L^2 or $\mathbf{L}^2$ norm, as well as the subspace norm, to illustrate the performance of different approaches.

2.1.1 *Spaces for field projections*

In Section 1.4, we defined the different spaces in order to host the physical fields in electromagnetic, mechanical and thermal models: $L^2(\mathscr{D})$, $\mathbf{L}^2(\mathscr{D})$, $H(\mathbf{grad}, \mathscr{D})$, $\mathbf{H}(\mathbf{curl}, \mathscr{D})$ and $\mathbf{H}(\mathrm{div}, \mathscr{D})$. These spaces are Sobolev spaces. Each one is equipped with an inner product [20]:

$$\forall f, g \in L^2(\mathscr{D}) : (f, g)_{L^2(\mathscr{D})} = \int_{\mathscr{D}} f \cdot g \tag{42}$$

$$\forall \mathbf{f}, \mathbf{g} \in \mathbf{L}^2(\mathscr{D}) : (\mathbf{f}, \mathbf{g})_{\mathbf{L}^2(\mathscr{D})} = \int_{\mathscr{D}} \mathbf{f} \cdot \mathbf{g} \tag{43}$$

$$\forall f, g \in H(\mathbf{grad}, \mathscr{D}) : \langle f, g\rangle_{H(\mathbf{grad}, \mathscr{D})} = \int_{\mathscr{D}} f \cdot g + \int_{\mathscr{D}} \mathbf{grad}\, f \cdot \mathbf{grad}\, g \tag{44}$$

$$\forall \mathbf{f}, \mathbf{g} \in \mathbf{H}(\mathbf{curl}, \mathscr{D}) : \langle \mathbf{f}, \mathbf{g}\rangle_{\mathbf{H}(\mathbf{curl}, \mathscr{D})} = \int_{\mathscr{D}} \mathbf{f} \cdot \mathbf{g} + \int_{\mathscr{D}} \mathbf{curl}\, \mathbf{f} \cdot \mathbf{curl}\, \mathbf{g} \tag{45}$$

$$\forall \mathbf{f}, \mathbf{g} \in \mathbf{H}(\mathrm{div}, \mathscr{D}) : \langle \mathbf{f}, \mathbf{g}\rangle_{\mathbf{H}(\mathrm{div}, \mathscr{D})} = \int_{\mathscr{D}} \mathbf{f} \cdot \mathbf{g} + \int_{\mathscr{D}} \mathrm{div}\, \mathbf{f} \cdot \mathrm{div}\, \mathbf{g} \tag{46}$$

For simplicity, in what follows we note $\mathscr{H}^1(\mathscr{D})$ in a general way for the three subspaces. $\mathscr{H}^1(\mathscr{D})$ stands for $H(\mathbf{grad}, \mathscr{D})$, $\mathbf{H}(\mathbf{curl}, \mathscr{D})$ or $\mathbf{H}(\mathrm{div}, \mathscr{D})$ depending on the context. Similarly we will write both $L^2(\mathscr{D})$ and $\mathbf{L}^2(\mathscr{D})$ as $\mathscr{L}^2(\mathscr{D})$.

For a (scalar or vectorial) function $f \in \mathscr{L}^2(\mathscr{D})$, the $\mathscr{L}^2(\mathscr{D})$-norm is defined as

$$\|f\|_{\mathscr{L}^2(\mathscr{D})} = (f, f)^{\frac{1}{2}}_{\mathscr{L}^2(\mathscr{D})} \tag{47}$$

If $f \in \mathscr{H}^1(\mathscr{D})$, the $\mathscr{H}^1(\mathscr{D})$-norm is given by

$$\|f\|_{\mathscr{H}^1(\mathscr{D})} = \langle f, f\rangle^{\frac{1}{2}}_{\mathscr{H}^1(\mathscr{D})} \tag{48}$$

2.1.2 *Problem to be solved*

Let $v \in \mathscr{L}^2(\mathscr{D})$ or $\mathscr{H}^1(\mathscr{D})$ be a known function in domain $\mathscr{D}$. In practice v stands for an analytical field or a numerical result derived from numerical approaches such as the finite element method.

On the same domain $\mathscr{D}$, we will consider a mesh of finite dimension. Its maximum diameter of elements is h. This target mesh can be different from the source mesh of v (if v is discretized). We introduce the related h-discretized subspaces $\mathscr{L}_h^2(\mathscr{D})$ and $\mathscr{H}_h^1(\mathscr{D})$.

The aim of the projection is to obtain, on the target mesh, an approximation u_h of v. Furthermore, we note that, on the target mesh u_h is discretized using the Whitney elements (Section 1.5):

$$u_h = \sum_{i=1}^{N} w_i X_i \tag{49}$$

with w_i the Whitney basis functions (scalar or vectorial, depending on the target simplex), X_i the degrees of freedom and N their total number.

For the sets of nodes, edges and facets, as a consequence of the combinatorial properties of the Whitney complex, u_h is ensured to be a member of $\mathscr{H}_h^1(\mathscr{D})$. For example, when we are looking for a scalar field u_h discretized on the nodes, we enforce in advance the target function $u_h \in H_h(\mathbf{grad}, \mathscr{D}) \subset L_h^2(\mathscr{D})$; on the edges, $\mathbf{u}_h \in \mathbf{H}_h(\mathbf{curl}, \mathscr{D}) \subset \mathbf{L}_h^2(\mathscr{D})$; and on the facets, $\mathbf{u}_h \in \mathbf{H}_h(\mathrm{div}, \mathscr{D}) \subset \mathbf{L}_h^2(\mathscr{D})$.

Thus depending on the chosen target elements and the importance of the derivative of the field (i. e. **grad**, **curl** or div), the projection can be carried out in two ways: the $\mathscr{L}^2$-projection and the $\mathscr{H}^1$-projection.

- $\mathscr{L}^2$-projection

  Given $v \in \mathscr{L}^2(\mathscr{D})$, find $u_h \in \mathscr{L}_h^2(\mathscr{D})$ which minimize the $\mathscr{L}^2$-norm of their difference:

  $$\|u_h - v\|_{\mathscr{L}^2(\mathscr{D})} \rightarrow \min \tag{50}$$

- $\mathscr{H}^1$-projection

  Given $v \in \mathscr{H}^1(\mathscr{D})$, on the corresponding element set (i. e. nodes, edges or facets) which provides discrete corresponding $\mathscr{H}_h^1(\mathscr{D})$, find u_h which minimize the $\mathscr{H}_1$-norm of their difference:

  $$\|u_h - v\|_{\mathscr{H}^1(\mathscr{D})} \rightarrow \min \tag{51}$$

A $\mathscr{H}^1$-projection reduces the $\mathscr{H}^1$-norm of the difference, i. e. the difference on the fields themselves but also on their derivatives. The $\mathscr{L}^2$-projection only reduces the difference in terms of the $\mathscr{L}^2$-norm (the fields themselves), regardless the precision on the derivatives.

Remark 1 *To the author's knowledge, the Whitney volume elements do not have any $\mathscr{H}^1(\mathscr{D})$-like properties. Thus, in this work, for the projections on volume elements, only $\mathscr{L}^2(\mathscr{D})$ is considered.*

In practice, if the source function v is only well defined in $\mathscr{L}^2(\mathscr{D})$, or the target elements are the volumes, the $\mathscr{L}^2$-projection is the only choice. If $v \in \mathscr{H}^1(\mathscr{D})$ but the chosen target elements do not provide the corresponding discrete space, the $\mathscr{H}^1$-projection is not possible. If $v \in \mathscr{H}^1(\mathscr{D})$ and the target elements are chosen with care, either the $\mathscr{L}^2$-projection or the $\mathscr{H}^1$-projection can be carried out.

2.1.3 *Weak formulations*

In the weak form using the Galerkin method, by introducing the test functions ψ_h in the target space, we solve the following formulations:

- $\mathscr{L}^2$-projection

  Given $v \in \mathscr{L}^2(\mathscr{D})$: find $u_h \in \mathscr{L}^2_h(\mathscr{D})$ which satisfies

$$(\psi_h, u_h - v)_{\mathscr{L}^2(\mathscr{D})} = 0, \ \forall \psi_h \in \mathscr{L}^2_h(\mathscr{D}) \tag{52}$$

- $\mathscr{H}^1$-projection

  Given $v \in \mathscr{H}^1(\mathscr{D})$: find $u_h \in \mathscr{H}^1_h(\mathscr{D})$ which satisfies

$$\langle \psi_h, u_h - v \rangle_{\mathscr{H}^1(\mathscr{D})} = 0, \ \forall \psi_h \in \mathscr{H}^1_h(\mathscr{D}) \tag{53}$$

The Galerkin method ensures the uniqueness of the solution. Furthermore, another key property of the Galerkin approach is that the error is orthogonal to the chosen subspace [35, 36].

Let u_h be the solution of equation (52) or (53) and $\varepsilon = u_h - v$ be the projection error. Using Céa's lemma [37, 38, 39], the norm of the projection error can be expressed as:

- For $\mathscr{L}^2$-projections

$$\|\varepsilon\|_{\mathscr{L}^2(\mathscr{D})} \leqslant \|\psi_h - v\|_{\mathscr{L}^2(\mathscr{D})}, \ \forall \psi_h \in \mathscr{L}^2_h(D) \tag{54}$$

- For $\mathscr{H}^1$-projections

$$\|\varepsilon\|_{\mathscr{H}^1(\mathscr{D})} \leqslant \|\psi_h - v\|_{\mathscr{H}^1(\mathscr{D})}, \ \forall \psi_h \in \mathscr{H}^1_h(D) \tag{55}$$

We note that these equations are valid for every applied test function. Each test function applied in the h-discretized space sets an upper bound for the error norm in the continuous space.

2.1.4 *Test function choices*

In the previous section, our initial problem of the projection is converted into an error norm minimizing problem by applying the test functions.

By the Galerkin method, the test function choice is limited to a h-discretized space $V_h(\mathscr{D})$. Here $V_h(\mathscr{D})$ stands for the target space chosen among $L_h^2(\mathscr{D})$, $\mathbf{L}_h^2(\mathscr{D})$, $H_h(\mathbf{grad}, \mathscr{D})$, $\mathbf{H}_h(\mathbf{curl}, \mathscr{D})$ and $\mathbf{H}_h(\mathrm{div}, \mathscr{D})$, depending on the projection to be carried out. In order to minimize the error norm in the continuous space, it is crucial to then fill $V_h(\mathscr{D})$ with test functions.

A natural idea is to choose a set of basis functions of $V_h(\mathscr{D})$ as the test functions. If the test functions ψ_h are chosen to be the same as the Whitney shape functions of the target function u_h, the method is called the Ritz-Galerkin method. Otherwise, it is called the Petrov-Galerkin method.

2.1.4.1 *Ritz-Galerkin method*

In [27, 28], this method is developed and applied to the projection in $\mathscr{L}^2(\mathscr{D})$. Similar applications can also be found in [29, 30, 31, 33, 34]. Here we recall their contributions and extend the theory to the subspaces $\mathscr{H}^1(\mathscr{D})$.

As the target function u_h is discretized by Whitney shape functions $\{w_i\}_{i=1}^N$, a natural choice is to take the same functions as the test functions: $\{\psi_{hi}\} = \{w_i\}, i = 1..N$.

Given that the advantages of this method are well discussed in the literature [40], we will not dwell on them here.

We note that, by this method, a linear system is obtained such that:

$$[C]\ \ [X] = [F] \tag{56}$$

where

$$C_{p,q} = \langle w_p, w_q \rangle_{V(\mathscr{D})} \tag{57a}$$

$$F_p = \langle w_p, v \rangle_{V(\mathscr{D})} \tag{57b}$$

and [X] is the vector of the degrees of freedom to be solved.

Using the Ritz-Galerkin method, the obtained [C] matrix is similar to a typical stiffness matrix in the finite element method computations. It is a symmetric positive-definite sparse matrix describing the stiffness among the degrees of freedom.

2.1.4.2 *Petrov-Galerkin method*

In this case a second basis is introduced: $\{\psi_{hi}\} = \{w_{PGi}\}, i = 1..N$. The new basis is different from the shape functions. In the linear system (56), the components in the [C] matrix are replaced by $C_{p,q} = \left\langle w_{PGp}, w_q \right\rangle_{V(\mathscr{D})}$ and [F] becomes $F_p = \left\langle w_{PGp}, v \right\rangle_{V(\mathscr{D})}$.

In spite of the freedom with respect to the test function choices, in practice the Petrov-Galerkin method is not widely used in comparison to the Ritz-Galerkin method. A set of test functions chosen without caution usually results in an ill-conditioned, even dense [C] matrix [41, 42].

In this part, we present a Petrov-Galerkin method with a specific choice of test functions. This technique calculates the local bi-orthogonal functions and uses them as a test basis. When applied to $\mathscr{L}^2(\mathscr{D})$-projections, it allows a diagonal [C] matrix to be directly built.

We note that local nodal bi-orthogonal functions have been used in [43] to define the interpolation operator and in [30, 44, 45] for domain decomposition theory. Here we determine them on the edge and facet elements. These functions are then used to define the projection test space.

Definition of bi-orthogonal functions

The mathematical definition of bi-orthogonal systems is given in [46]. When applied to a $\mathscr{L}^2(\mathscr{D})$-projection, we consider that :

Given a Whitney basis $\{w_i\}_{i=1}^{N}$ associated with a mesh of tetrahedrons, the local bi-orthogonal basis $\{\psi_{B_j}\}_{j=1}^{N}$ is a family of functions in the dual space such that $\forall K \in \mathscr{T}$:

$$\left(\psi_{B_j}, w_i\right)_{\mathscr{L}^2(K)} = \begin{cases} 1 & \forall i = j \\ 0 & \forall i \neq j \end{cases} \tag{58}$$

where $\mathscr{L}^2(K)$ is the space associated with a single tetrahedron K on the target mesh.

Remark 2 *For $\mathscr{L}^2(K)$ and even the subspaces $\mathscr{H}^1(K)$, equation (58) guarantees the local bi-orthogonal functions are well defined. However, we should note that the local bi-orthogonal functions are determined in each tetrahedron. As such, no continuous condition applies on the interface of two elements. The thus determined functions are NOT included in the $\mathscr{H}^1(\mathscr{D})$ space. In this work, we thus restrict ourselves to the $\mathscr{L}^2(\mathscr{D})$-projections when using the bi-orthogonal test functions.*

For a $\mathscr{L}^2(\mathscr{D})$-projection, when a bi-orthogonal basis is chosen as the test functions, the projection map is given by

$$[C_B]\ [X] = [F_B] \tag{59}$$

where $F_{B_p} = \left(\psi_{B_p}, v\right)_{\mathscr{L}^2(\mathscr{D})}$ and $[C_B]$ is a diagonal matrix. In the classical Ritz-Galerkin method a linear system of equations must be solved. The advantage of using a method such as the Petrov-Galerkin method with bi-orthogonal test functions is that the obtained system is much simpler to solve.

Determination of local bi-orthogonal functions

For a tetrahedron K on the target mesh, we can determine the local bi-orthogonal functions $\{\psi_{B_j}\}_{j=1}^{n}$ associated with the n local target Whitney elements. In this work, we restrict ourselves to the case of polynomial degree one for the Whitney shapes as well as for the test functions. Each bi-orthogonal function can be written as a linear combination of the Whitney shape functions:

$$\psi_{B_j} = \sum_{k=1}^{n} \alpha_{jk} w_k \text{ in } K \tag{60}$$

The coefficients $\{\alpha_{jk}\}$ are obtained by solving equation (58). It can be shown that this is the inversed matrix of the $n \times n$ matrix system of tetrahedron K:

$$[\alpha]\ [M] = [I] \tag{61}$$

where $M_{p,q} = (w_p, w_q)_{\mathscr{L}^2(K)}$ is the scalar product of the classical Whitney functions and [I] an identity matrix.

Scalar nodal bi-orthogonal functions can be found in [47] for both 2D and 3D cases. They are also presented in Appendix A of this manuscript. We use them in this work as test functions for the nodal $L^2(\mathscr{D})$-projection. However, in practice for the projection on edge or facet elements, a coordinate transformation using the Jacobian matrix is used when evaluating the numerical integral. In this case the bi-orthogonal functions must be determined in each tetrahedron [48].

In terms of application for the edge or facet elements, the first step is to solve equation (61) in each tetrahedron. In this way we have determined the local bi-orthogonal functions. However, so far, a determined function is associated to one single tetrahedron.

Then, in order to apply these functions in the projection, a second step is carried out. For a target element (edge or facet), as it may appear in several tetrahedrons, we combine all the functions (determined in the first step) connected to this element into one only. In this way, we obtain a single novel function, which is piecewise-defined in all tetrahedrons connected to the target element and null in the rest. This time the domain for the novel function is the whole mesh.

To illustrate, let us consider a 2D mesh of two triangles. The two triangles share one common boundary. In Figure 4 and Figure 5, the Whitney functions associated with this boundary, as well as the bi-orthogonal functions, are shown. Details of their precise determination are presented in Appendix A.

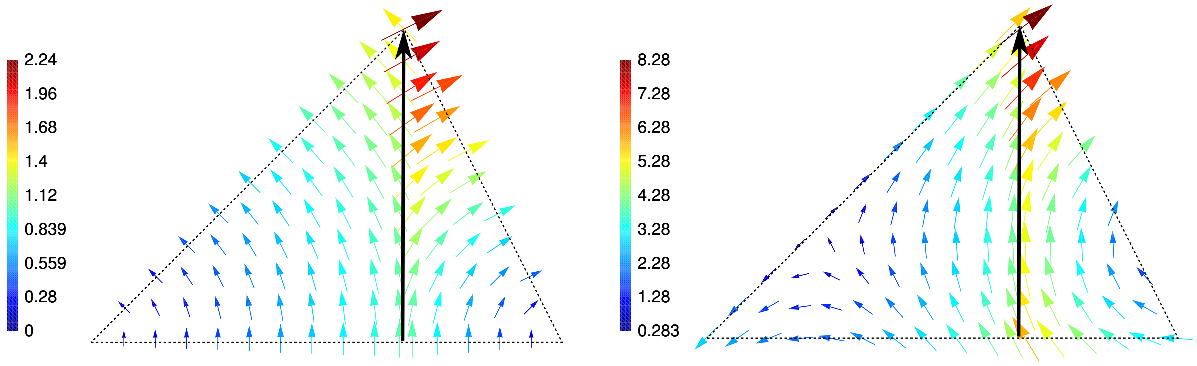

(a) Whitney edge functions (b) Bi-orthogonal edge functions

Figure 4: Whitney functions and bi-orthogonal functions associated with the common edge.

Unlike the Whitney functions, the bi-orthogonal functions have no continuous condition on the shared boundary. As previously indicated the bi-orthogonal functions are not members of $\mathscr{H}^1(\mathscr{D})$. They can only be used in the $\mathscr{L}^2(\mathscr{D})$-projections.

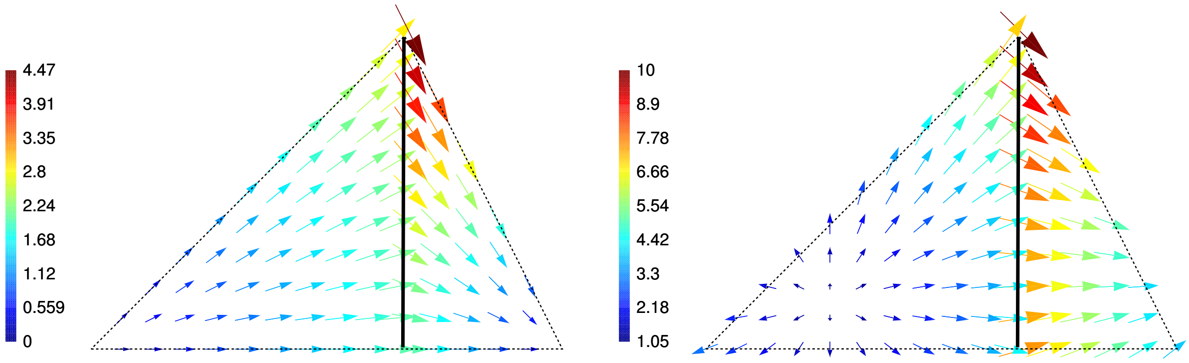

(a) Whitney facet functions

(b) Bi-orthogonal facet functions

Figure 5: Whitney functions and bi-orthogonal functions associated with the common facet.

However, the discontinuity of the bi-orthogonal functions does not affect the continuity of the obtained solution. We recall that the bi-orthogonal functions are used as test functions. The target solution is always discretized with the continuous Whitney shape functions.

2.1.5 *Mesh-to-mesh implementation*

The projection formulations produce a matrix equation such as in (56) or (59). In spite of their mathematical simplicity, the general assembly of this equation is quite difficult in practice. In finite element computations, physical fields are associated with specific discrete elements such as nodes, edges, facets and volumes. The shape function of an element is typically a linear or quadratic piecewise function defined in the surrounding volumes. Together with the degrees of freedom, the fields are discretized as piecewise polynomial over the considered domain (Section 1.5).

In (57a), the entries of [C] matrix are the scalar products of the shape functions on the target mesh. They can be iteratively calculated over the target elements.

Nevertheless, in (57b) for the calculation of the right-hand vector [F], w_p and v are associated with different meshes. $\{w_p\}_{p=1}^{N}$ are the shape functions of the target mesh, whereas v is the source field given on the source mesh. Let us suppose that v is also discretized with Whitney elements:

$$v = \sum_{j=1}^{N'} w'_j Y_j \tag{62}$$

where $\{w'_j\}_{j=1}^{N'}$ are the shape functions on the source mesh.

In this case, the entries of [F] can be written as:

$$F_p = \int_{\mathscr{D}} w_p \cdot \sum_{j=1}^{N'} w'_j Y_j \tag{63}$$

In order to assemble these entries, it is necessary to calculate the scalar product of the Whitney functions of different meshes: w_i of the target mesh and w'_j of the source mesh. To achieve this aim, the accurate calculation should be carried out over an intermediate mesh of which the cells are the intersections of the source and target meshes. In one intersection, which is often a polyhedron, the Whitney functions w_i and w'_j can be easily defined since the corresponding source and target elements are given. Both shape functions are polynomials and therefore so is their product. After clipping the polyhedron into more regular shapes (e.g. tetrahedrons in 3D cases), the product of the Whitney functions can be computed with quadrature rules.

For illustrative purposes, let us consider two 2D triangular meshes. The intersections of one target element with the source mesh are shown in Figure 6.

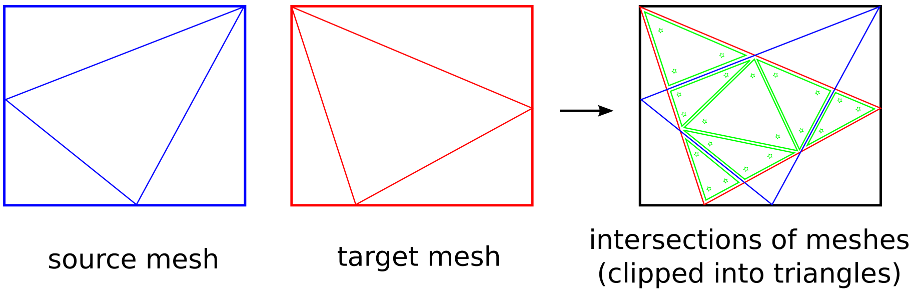

Figure 6: Intersections (green) of one target triangular element (red) with the source mesh (blue). Three quadrature points can then be applied to each intersection (green stars). The resulting mesh is actually the lowest common mesh for source and target meshes.

The algorithm of a general implementation of the projection with the intersections can be summarized as follows:

(i) Find the intersecting pairs of source and target elements.

(ii) Loop over target elements:

  1 Calculate the product of w_i, w_j and assemble in the $[C]$ matrix: (57a).

  2 Loop over intersecting source elements:

    a) Identify the intersection region.

    b) Clip the intersecting region into tetrahedrons.

    c) Over tetrahedral intersections: calculate the product of w_i, v and assemble in the $[F]$ vector: (57b).

(iii) Solve the linear system (56).

We refer to [49, 50] for further studies on the mesh intersection technique. Let N' and N be the element number of the source and target meshes respectively; detecting the intersecting pairs using a R-tree requires a time of $O[(N+N')\log(N')]$. The intersections can then be calculated using the Sutherland-Hodgman clipping algorithm [51, 52]: in order to find the intersecting region, each face of the clipping element is considered in turn. Generally speaking, for field projections using the intersection technique, the most significant part of computation time is consumed by the construction of intersections. In the 2D example (Figure 6), for two meshes of 4 triangles the resulting intersections are 16 triangles. For 3D cases, the technique of intersection is even more computationally expensive. The intersection of two tetrahedral meshes of about 10^5 elements may results in millions of tetrahedrons.

2.1.6 *Numerical example*

The proposed projection methods are applied to the imposition of analytical fields and to mesh-to-mesh field transmission [53].

As presented in Section 1.5, depending on the mathematical characteristics of a physical field, the geometric support is usually different Whitney elements: nodes, edges, facets or volumes. Here, we will present, on all four support types, different numerical results illustrating the performance of various projection methods.

For the fields discretized on nodes, edges or facets, the classical $\mathscr{L}^2(\mathscr{D})$ theory, as well as the presented $\mathscr{H}^1(\mathscr{D})$ formulations, will be used. For $\mathscr{L}^2(\mathscr{D})$-projections, we apply the Ritz-Galerkin method and the Petrov-Galerkin method using local bi-orthogonal test functions. For $\mathscr{H}^1(\mathscr{D})$-projections, only the Ritz-Galerkin method is used.

In implementation terms, for the mesh-to-mesh projections, the numerical integration of vector $[F]$ in (56) or $[F_B]$ in (59) is carried out on the lowest common mesh for the "source" and "target" fields, as presented in Section 2.1.5. To solve the linear systems, the conjugate gradient method is employed.

In this part, we project analytical fields on the different supports and then treat the mesh-to-mesh projections.

We consider two meshes of tetrahedrons on a cubic domain: $\mathscr{D} = (0, 1)^3$ (Figure 7). The characteristics of the meshes are given in Table 1.

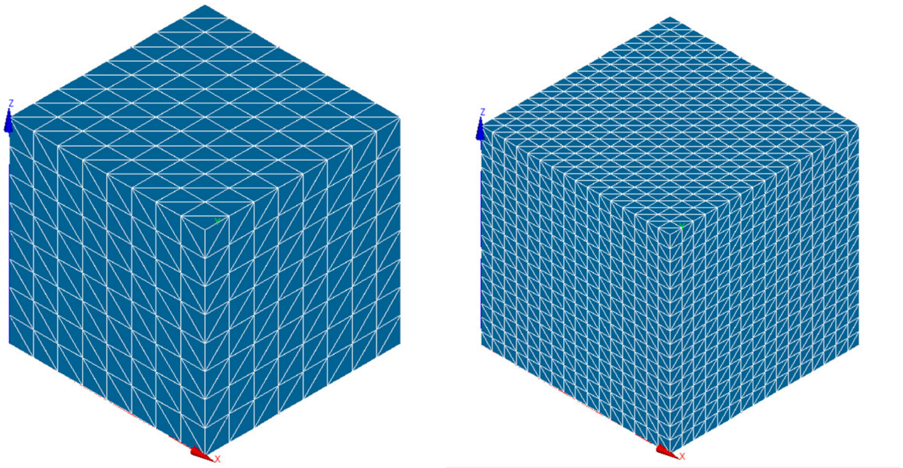

(a) Mesh 1 (b) Mesh 2

Figure 7: Meshes of the cubic domain used here.

Table 1: Characteristics of the meshes used.

mesh	# nodes	# edges	# facets	# volumes
1	729	4184	6528	3072
2	4913	31024	50688	24576

Remark 3 *Here mesh 2 is obtained by a refinement of mesh 1. Thus the discretized spaces are enlarged:* $\mathscr{L}^2_{h1} \subset \mathscr{L}^2_{h2}$ *and* $\mathscr{H}^1_{h1} \subset \mathscr{H}^1_{h2}$.

In the following, different analytical fields will be projected. All projected solutions will be compared to the analytical solution. Let $\varepsilon = u_h - v$ be the projection error. We recall that its norm in the space $V(\mathscr{D})$ (i.e. $L^2(\mathscr{D})$, $\mathbf{L}^2(\mathscr{D})$, $H(\mathbf{grad}, \mathscr{D})$, $\mathbf{H}(\mathbf{curl}, \mathscr{D})$ or $\mathbf{H}(\mathrm{div}, \mathscr{D})$) is defined as the root of its inner product with itself.

In this part, to illustrate the projection accuracy, we will also use the notion of relative error such that:

$$\varepsilon^r_{V(\mathscr{D})} = \frac{\|\varepsilon\|_{V(\mathscr{D})}}{\|v\|_{V(\mathscr{D})}} = \frac{\|u_h - v\|_{V(\mathscr{D})}}{\|v\|_{V(\mathscr{D})}} \tag{64}$$

2.1.6.1 *Projection on the node elements*

We consider a quadratic scalar field: $v(x, y, z) = x^2$ with a linear gradient: $\mathbf{grad}\, v = \mathbf{vect}(2x, 0, 0)$.

Imposition of the analytical solution

The analytical field is projected on the node elements of the two target meshes. In Table 2 and Table 3, the projection errors are given using the $L^2(\mathscr{D})$-norm as well as the $H(\mathbf{grad}, \mathscr{D})$-norm.

Remark 4 *Using the standard* $\mathscr{L}^2(\mathscr{D})$ *projections, the precision of the distributional derivatives is not guaranteed. However, we still illustrate their error in the* $\mathscr{H}^1(\mathscr{D})$*-norm for reference purposes.*

Table 2: Projection errors on mesh 1 (node elements). The target fields are obtained from analytical-to-discrete projections using different methods.

Projection method	$\|\varepsilon\|_{L^2(\mathscr{D})}$	$\varepsilon^r_{L^2(\mathscr{D})}$	$\|\varepsilon\|_{H(\mathbf{grad},\mathscr{D})}$	$\varepsilon^r_{H(\mathbf{grad},\mathscr{D})}$
$L^2(\mathscr{D})$ Ritz-Galerkin	1.16e-3	0.26%	7.21e-2	5.8%
$L^2(\mathscr{D})$ Petrov-Galerkin ψ_B	1.16e-3	0.26%	7.21e-2	5.8%
$H(\mathbf{grad}, \mathscr{D})$ Ritz-Galerkin	1.56e-3	0.35%	7.18e-2	5.8%

As shown in [47], for the nodal projections, using a H^2-regular source field, the optimal error using $L^2(\mathscr{D})$-norm is of order h^2, and for the $H(\mathbf{grad}, \mathscr{D})$-norm, it is of order h.

Table 3: Projection errors on mesh 2 (node elements), calculated in the analytical-to-discretized projection using different methods.

Projection method	$\|\varepsilon\|_{L^2(\mathscr{D})}$	$\varepsilon^r_{L^2(\mathscr{D})}$	$\|\varepsilon\|_{H(\mathbf{grad},\mathscr{D})}$	$\varepsilon^r_{H(\mathbf{grad},\mathscr{D})}$
$L^2(\mathscr{D})$ Ritz-Galerkin	2.91e-4	0.065%	3.61e-2	2.9%
$L^2(\mathscr{D})$ Petrov-Galerkin ψ_B	2.91e-4	0.065%	3.61e-2	2.9%
$H(\mathbf{grad},\mathscr{D})$ Ritz-Galerkin	3.94e-4	0.088%	3.60e-2	2.9%

Here, by the different projection methods, the relative projection error for the $L^2(\mathscr{D})$-norm is smaller than 0.5%. Our numerical results show that, for a nodal $L^2(\mathscr{D})$-projection, the use of bi-orthogonal test functions has almost no influence on the result accuracy. The $H(\mathbf{grad},\mathscr{D})$ projection using the Ritz-Galerkin method slightly reduces the absolute error for the $H(\mathbf{grad},\mathscr{D})$-norm, despite loss of accuracy for $L^2(\mathscr{D})$.

Mesh-to-mesh projection

We then carry out the mesh-to-mesh projections. Here a previously calculated field on mesh 2 (the $L^2(\mathscr{D})$ Ritz-Galerkin result in Table 2) is used as the source field, and we calculate the projection approximation on mesh 1. We do not project in the opposite direction because the projection does not improve the accuracy (mesh 2 is finer). For a coarse-mesh to fine-mesh projection, the best possible result will be no more accurate than the source field. Here we are interested in fine-mesh to coarse-mesh projections, in order to study the information conservation.

In Table 4, we continue to compare the projection results to the analytical field v imposed in the continuous domain.

The obtained results are at least as accurate as the continuous-to-discretized calculations (Table 3). In Table 5, we show the computation time for the mesh-to-mesh projection using the different methods. The consumed time by the intersection of meshes and the construction of the linear system is also taken into account.

Table 4: Mesh-to-mesh projection errors. The target solution is obtained on mesh 1 (node elements) using different methods.

Projection method	$\|\varepsilon\|_{L^2(\mathscr{D})}$	$\varepsilon^r_{L^2(\mathscr{D})}$	$\|\varepsilon\|_{H(\mathbf{grad},\mathscr{D})}$	$\varepsilon^r_{H(\mathbf{grad},\mathscr{D})}$
source field	2.91e-4	0.065%	3.61e-2	2.9%
$L^2(\mathscr{D})$ Ritz-Galerkin	1.16e-3	0.26%	7.21e-2	5.8%
$L^2(\mathscr{D})$ Petrov-Galerkin ψ_B	1.16e-3	0.26%	7.21e-2	5.8%
$H(\mathbf{grad},\mathscr{D})$ Ritz-Galerkin	1.40e-3	0.31%	7.18e-2	5.8%

Table 5: Used computation time for mesh1-to-mesh2 projections.

Projection method	$L^2(\mathscr{D})$ Ritz-Galerkin	$L^2(\mathscr{D})$ Petrov-Galerkin ψ_B	$H(\mathbf{grad}, \mathscr{D})$ Ritz-Galerkin
Computation time	159s	156s	164s

Compared to the $L^2(\mathscr{D})$-projections the projections using the $H(\mathbf{grad}, \mathscr{D})$ formulation (53) require additional computation time on the gradient components.

In this analytical example, the use of the Petrov-Galerkin method and the bi-orthogonal test functions gives little advantage in terms of the computation time. This approach does, however, give a diagonal matrix in the linear system, thus reducing the memory cost and simplifying its solution. The advantage with respect to the computation time becomes greater on finer meshes.

2.1.6.2 *Projection on the edge elements*

For the edge elements, we consider an analytical vector field included in $\mathbf{H}(\mathbf{curl}, \mathscr{D})$: $\mathbf{v}(x, y, z) = \mathbf{vect}(y^2, 0, 0)$, where the curl is given by $\mathbf{vect}(0, 0, -2y)$.

Imposition of the analytical solution

Visually, using the different projection methods, the calculated vectorial fields are almost all the same. We give the obtained result using the $\mathbf{L}^2(\mathscr{D})$ Ritz-Galerkin method in Figure 8.

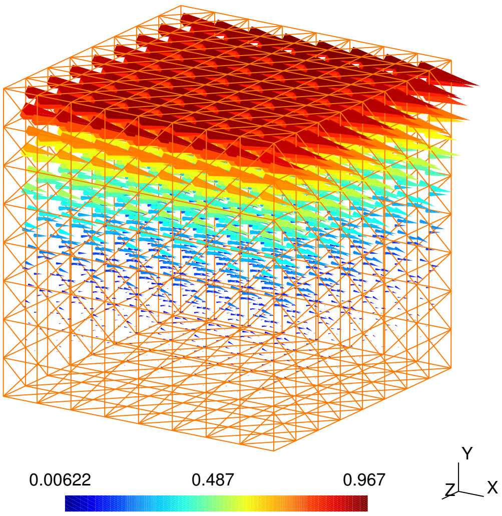

Figure 8: Projected field on mesh 1 (edge elements), obtained in the analytical-to-discretized projection using the $\mathbf{L}^2(\mathrm{D})$ Ritz-Galerkin method.

As for the nodal projections, we show the projection errors using the $\mathbf{L}^2(\mathscr{D})$-norm and the $\mathbf{H}(\mathbf{curl},\mathscr{D})$-norm (Table 6 for mesh 1 and Table 7 for mesh 2). We recall that, in comparison to the $\mathbf{L}^2(\mathscr{D})$-norm, the $\mathbf{H}(\mathbf{curl},\mathscr{D})$-norm contains an additional part, i.e. the scalar product of the curl of the error.

Table 6: Projection errors on mesh 1 (edge elements), calculated in the analytical-to-discretized projection using different methods.

Projection method	$\|\varepsilon\|_{\mathbf{L}^2(\mathscr{D})}$	$\varepsilon^r_{\mathbf{L}^2(\mathscr{D})}$	$\|\varepsilon\|_{\mathbf{H}(\mathbf{curl},\mathscr{D})}$	$\varepsilon^r_{\mathbf{H}(\mathbf{curl},\mathscr{D})}$
$\mathbf{L}^2(\mathscr{D})$ Ritz-Galerkin	5.07e-2	11.3%	6.43e-1	51.9%
$\mathbf{H}(\mathbf{curl},\mathscr{D})$ Petrov-Galerkin ψ_B	5.38e-2	12.0%	2.64e-1	21.3%
$\mathbf{H}(\mathbf{curl},\mathscr{D})$ Ritz-Galerkin	5.55e-2	12.3%	8.55e-2	6.9%

Table 7: Projection errors on mesh 2 (edge elements), calculated in the analytical-to-discretized projection using different methods.

Projection method	$\|\varepsilon\|_{\mathbf{L}^2(\mathscr{D})}$	$\varepsilon^r_{\mathbf{L}^2(\mathscr{D})}$	$\|\varepsilon\|_{\mathbf{H}(\mathbf{curl},\mathscr{D})}$	$\varepsilon^r_{\mathbf{H}(\mathbf{curl},\mathscr{D})}$
$\mathbf{L}^2(\mathscr{D})$ Ritz-Galerkin	2.73e-2	6.1%	4.99e-1	40.3%
$\mathbf{H}(\mathbf{curl},\mathscr{D})$ Petrov-Galerkin ψ_B	2.82e-2	6.3%	1.89e-1	15.2%
$\mathbf{H}(\mathbf{curl},\mathscr{D})$ Ritz-Galerkin	2.89e-2	6.5%	4.36e-2	3.5%

We refer to [54] for a $\mathbf{H}(\mathbf{curl},\mathscr{D})$ application on non-overlapping domain decomposition and the error estimation. When applied to the projection, on mesh 1 and mesh 2, the three methods have almost the same level of accuracy in the $\mathbf{L}^2(\mathscr{D})$-space (Table 6 and Table 7). However, the $\mathbf{H}(\mathbf{curl},\mathscr{D})$ Ritz-Galerkin method has the best accuracy in terms of the $\mathbf{H}(\mathbf{curl},\mathscr{D})$ error norm. In Figure 9, we compare the curl of the fields projected using the different methods.

The $\mathbf{H}(\mathbf{curl},\mathscr{D})$ Ritz-Galerkin has a projection result which gives the smoothest curl at the bounds. Indeed, as previously shown, for the node elements, no significant difference is observed using the different projection methods. Here in comparison with the gradient operator, the curl operator is, to a certain extent, "more complex", and the advantage of using the $\mathbf{H}(\mathbf{curl},\mathscr{D})$-projection instead of a $\mathbf{L}^2(\mathscr{D})$-projection is illustrated by the fact that we obtain better curl results.

Mesh-to-mesh projection

Let the previously projected field on mesh 2 using the $\mathbf{H}(\mathbf{curl},\mathscr{D})$ Ritz-Galerkin method (row 3 in Table 6) be the source field. We carry out a mesh-to-mesh projection and look for an approximation on mesh 1.

The projected fields are then compared to the analytical field $\mathbf{v}$ (Table 8). The computation time is illustrated in Table 9.

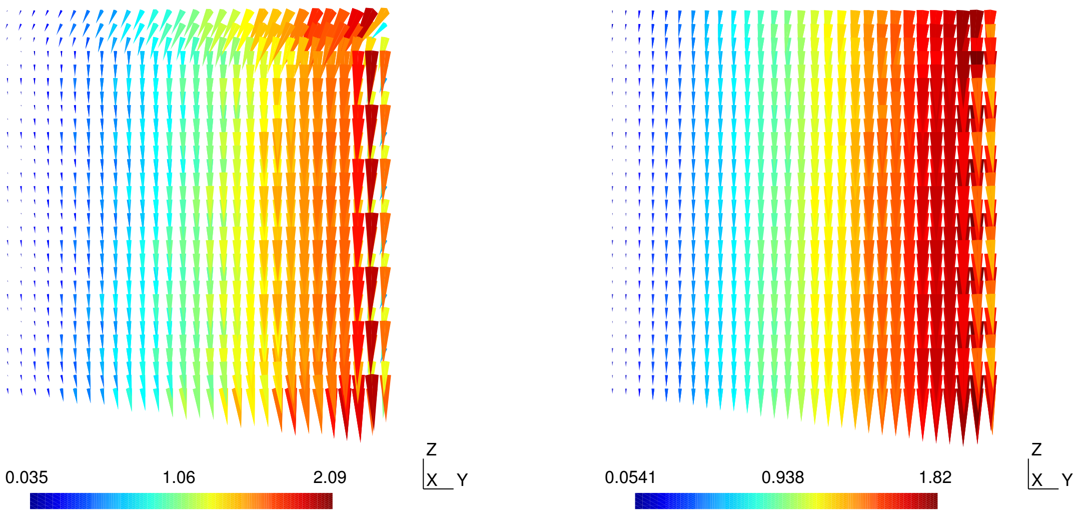

(a) $\mathbf{L}^2(\mathscr{D})$ Ritz-Galerkin (b) $\mathbf{L}^2(\mathscr{D})$ Petrov-Galerkin ψ_B

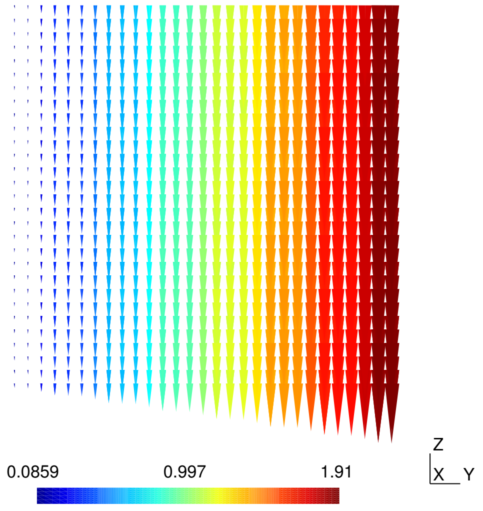

(c) $\mathbf{H}(\mathbf{curl},\mathscr{D})$ Ritz-Galerkin

Figure 9: Curl of projected fields, plotted on the plane $x = 0.5$ of mesh 1.

Table 8: Mesh-to-mesh projection errors. The target solution is obtained on mesh 1 (edge elements) using different methods.

Projection method	$\|\varepsilon\|_{\mathbf{L}^2(\mathscr{D})}$	$\varepsilon^r_{\mathbf{L}^2(\mathscr{D})}$	$\|\varepsilon\|_{\mathbf{H}(\mathbf{curl},\mathscr{D})}$	$\varepsilon^r_{\mathbf{H}(\mathbf{curl},\mathscr{D})}$
source field	2.89e-2	6.5%	4.36e-2	3.5%
$\mathbf{L}^2(\mathscr{D})$ Ritz-Galerkin	5.10e-2	11.4%	4.80e-1	38.7%
$\mathbf{H}(\mathbf{curl},\mathscr{D})$ Petrov-Galerkin ψ_B	5.39e-2	12.0%	2.08e-1	16.8%
$\mathbf{H}(\mathbf{curl},\mathscr{D})$ Ritz-Galerkin	5.55e-2	12.4%	8.55e-2	6.9%

Table 9: Computation time required for mesh2-to-mesh1 projections.

Projection method	$\mathbf{L}^2(\mathscr{D})$ Ritz-Galerkin	$\mathbf{L}^2(\mathscr{D})$ Petrov-Galerkin ψ_B	$\mathbf{H}(\mathbf{curl},\mathscr{D})$ Ritz-Galerkin
Computation time	226s	163s	1174s

As the source field used here gives good accuracy in terms of the $\mathbf{H}(\mathbf{curl},\mathscr{D})$ error norm, the mesh-to-mesh projected field is more accurate on the curl, as can be seen when compared to the results in Table 7. This may explain an advantage of using projection approaches. Indeed, to get an accurate target field, we launch the first calculation on a finer mesh and then project the obtained field on the target mesh. The thus calculated field may be preferable in comparison to direct computation on the target mesh.

In terms of the computation time, as a mesh of tetrahedrons has more edges than nodes, here the actual computation time is greater than the nodal projections. In this case, the results illustrate the performance of the approach using local bi-orthogonal test functions.

2.1.6.3 *Projection on the facet elements*

Let $\mathbf{v}(x,y,z) = \mathbf{vect}(x^2,0,0)$ be the analytical field to be projected, where its divergence is equal to $2x$.

Imposition of the analytical solution

Here we present the projected fields on mesh 1 (Figure 10) and their divergence (Figure 11). The projection errors are then compared in Table 10 for the different methods.

By the $\mathbf{H}(\mathrm{div},\mathscr{D})$ Ritz-Galerkin method, we obtain a result which is the most accurate in terms of the $\mathbf{L}^2(\mathscr{D})$ error norm as well as for the $\mathbf{H}(\mathrm{div},\mathscr{D})$-norm. However, this method requires significant computation time.

Using the Petrov-Galerkin method with local bi-orthogonal test functions, we are unable to guarantee the precision of the divergence. However, the obtained linear system is much

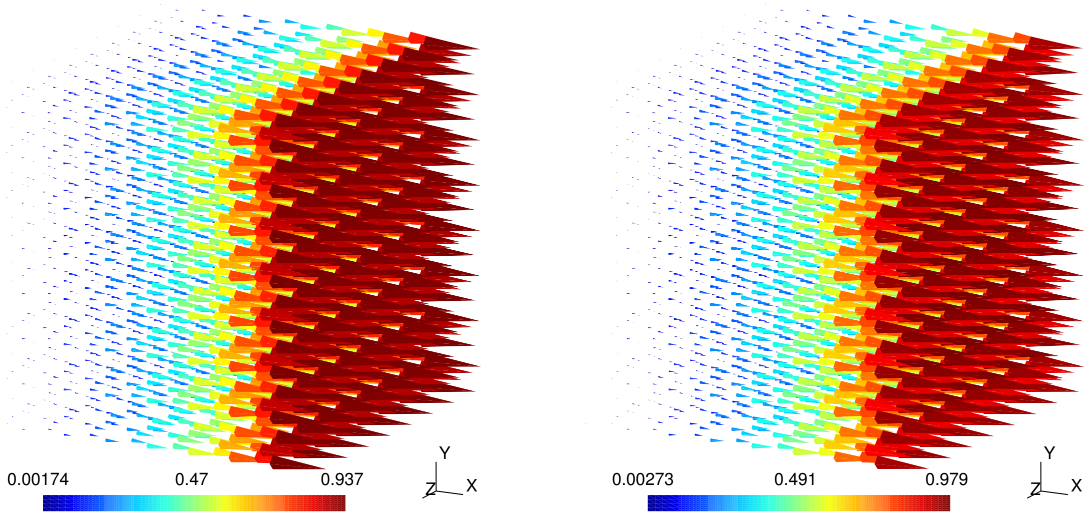

(a) $\mathbf{L}^2(\mathscr{D})$ Ritz-Galerkin

(b) $\mathbf{H}(\mathrm{div}, \mathscr{D})$ Ritz-Galerkin

Figure 10: Projected fields on mesh 1 (facet elements).

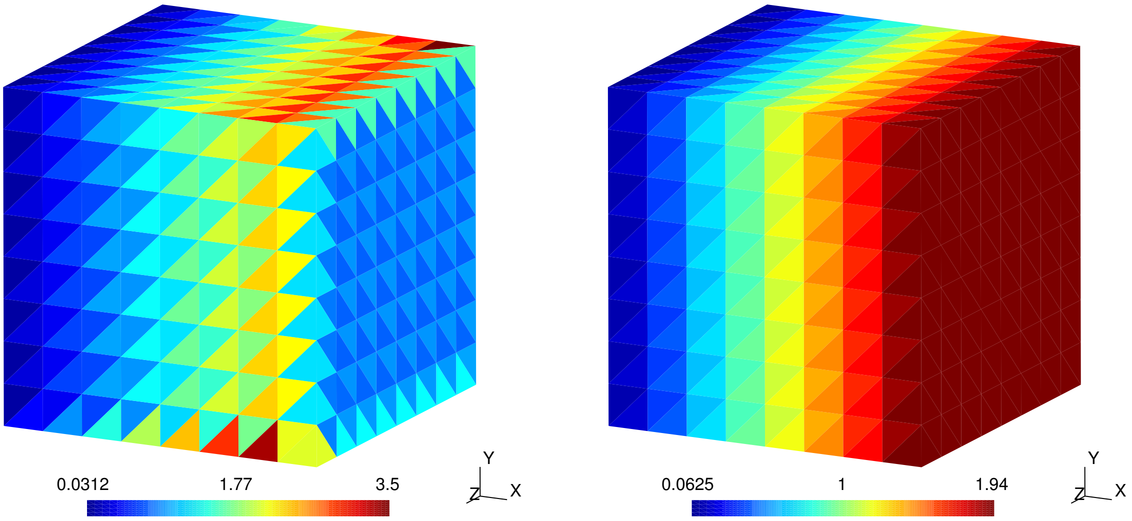

(a) $\mathbf{L}^2(\mathscr{D})$ Ritz-Galerkin

(b) $\mathbf{H}(\mathrm{div}, \mathscr{D})$ Ritz-Galerkin

Figure 11: Divergence of the projected fields on mesh 1 (facet elements).

easier to solve than the one obtained using the classical $\mathbf{L}^2(\mathscr{D})$ Ritz-Galerkin method. The computation time, as well as the memory cost, are greatly decreased.

Table 10: Projection errors on mesh 1 (facet elements), calculated with respect to the analytical-to-discretized projection using different methods.

Projection method	$\|\varepsilon\|_{\mathbf{L}^2(\mathscr{D})}$	$\varepsilon^r_{\mathbf{L}^2(\mathscr{D})}$	$\|\varepsilon\|_{\mathbf{H}(\mathrm{div},\mathscr{D})}$	$\varepsilon^r_{\mathbf{H}(\mathrm{div},\mathscr{D})}$
$\mathbf{L}^2(\mathscr{D})$ Ritz-Galerkin	4.34e-2	9.70%	9.67e-1	78.0%
$\mathbf{L}^2(\mathscr{D})$ Petrov-Galerkin - ψ_B	4.50e-2	10.08%	8.08e-1	65.2%
$\mathbf{H}(\mathrm{div},\mathscr{D})$ Ritz-Galerkin	4.06e-2	9.07%	9.04e-2	7.29%

Table 11: Computation time required for analytical-to-discrete projections.

Projection method	$\mathbf{L}^2(\mathscr{D})$ Ritz-Galerkin	$\mathbf{L}^2(\mathscr{D})$ Petrov-Galerkin ψ_B	$\mathbf{H}(\mathrm{div},\mathscr{D})$ Ritz-Galerkin
Computation time	162s	89s	1780s

2.1.6.4 *Projection on the volume elements*

Unlike the other elements, for the field discretized using volumes, we only consider the $L^2(\mathscr{D})$ projection. The reason for this is explained in Remark 1. As the Whitney volume shape functions of the lowest degree are constant in each tetrahedron (Section 1.5), the obtained $[C]$ matrix to be inversed is already diagonal. Thus, no bi-orthogonal test function is calculated in this part.

We consider a linear function $v(x, y, z) = x$. Using the $L^2(\mathscr{D})$ Ritz-Galerkin method, the projected field on mesh 1 has an relative error of 4.4%.

2.1.7 *Conclusion*

Computation of coupling problems requires field communication when the subproblems are discretized on multiple meshes. The field projection approaches based on the Galerkin method presented in this section provide useful tools for such cases. The classical Ritz-Galerkin method is recalled and extended to $H(\mathbf{grad})$, $\mathbf{H}(\mathbf{curl})$ and $\mathbf{H}(\mathrm{div})$ in order to obtain greater projection accuracy for the distributional derivatives. Subsequently, the bi-orthogonal test functions are used to build a Petrov-Galerkin projection system with a diagonal matrix. Through the analytical examples, the $H(\mathbf{grad})$, $\mathbf{H}(\mathbf{curl})$ and $\mathbf{H}(\mathrm{div})$ projections give greater accuracy than L^2 or $\mathbf{L}^2$ projections. In the case of L^2 or $\mathbf{L}^2$ projections, the Petrov-Galerkin method with bi-orthogonal test functions allows the same level of accuracy as the Ritz-Galerkin method, while notably reducing the computation cost.

2.2 IMPLEMENTATION CONSIDERATION

In practice the general implementation of mesh-to-mesh field projections has proved challenging. As the source and target fields are discretized on different meshes, the accurate assembly of the projection system necessitates numerical integration over an intermediate mesh. In practice, such an intermediate mesh can be calculated by means of intersecting the source and target meshes (Section 2.1.5). However, the use of intersection requires significant programming work and a high computation cost [55, 49].

Another possibility is to avoid mesh intersections, by using a sampling-integration algorithm. Instead of integrating over the lowest common mesh, the integrals are computed over the target mesh. Over the quadrature points of target elements, the source solution is sampled and approximately integrated. This is less accurate than integrating over intersections. The accuracy, however, can be improved using high-order quadrature rules.

In this section, we focus on a comparison of the two implementation techniques for Galerkin projection. For applications, depending on the problem to be solved, Galerkin projection can be applied to different fields and at different times. Here we analyze the advantages and disadvantages for the two implementation techniques, in terms of accuracy, speed and computational complexity.

For the sake of simplicity, in this section we restrict ourselves to the case of $\mathscr{L}^2(\mathscr{D})$ (i. e. $\mathrm{L}^2(\mathscr{D})$ and $\mathbf{L}^2(\mathscr{D})$) Ritz-Galerkin projections. Nevertheless, the implementation techniques we present, can be easily extended to $\mathscr{H}^1(\mathscr{D})$ projections and to the Petrov-Galerkin method (e. g. bi-orthogonal test functions).

2.2.1 *Sampling-integration over the target elements*

Unlike the intersection of meshes (Section 2.1.5), the second implementation is solely implemented over the target elements.

Over each target element, the Whitney functions w_i can be easily defined because they are associated with the same mesh. The shape functions w'_j which are associated with the source mesh, can be evaluated over the Gaussian quadrature points. As such, the product of w_i and w'_j can be approximated with the weighted sum over the quadrature points. This technique is much simpler in terms of computational complexity. However, the integration accuracy can not be ensured. The quadrature scheme is in general exact for a specified polynomial order. However, in the case where w'_j is associated with a different mesh, w'_j is piecewise-defined and may has several subdomains in one specific target element. This error in the calculation of the integral, leads to the inaccuracy of the assembly of the vector $[\mathrm{F}]$ as the right-hand side of (56).

To illustrate, Figure 12 presents the quadrature points taken in a target element. Compared to Figure 6, the computational complexity is clearly reduced.

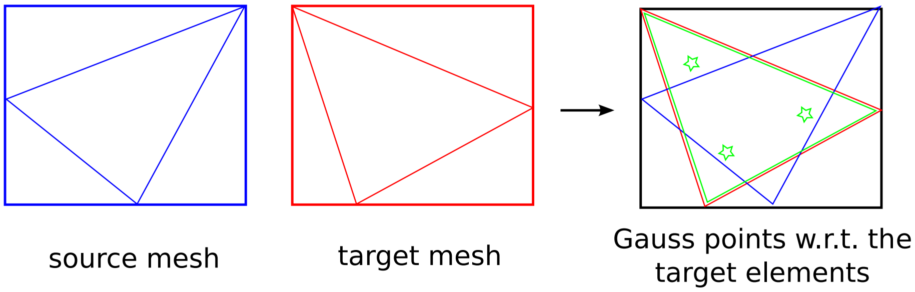

Figure 12: Three quadrature points (green stars) taken with respect to one target triangular element (red).

The implementation of the field projection with the sampling-integration algorithm over target elements can be summarised as follows:

(i) Loop over target elements:
  1 Calculate the product of w_i, w_j and assemble in the $[C]$ matrix: (57a).
  2 Calculate the product of w_i, v and assemble in the $[F]$ vector: (57b).

(ii) Solve the linear system (56).

We note that, although both are calculated over target elements, here steps (i)1 and (i)2 are not constrained by the same quadrature rules.

- In the case of linear Whitney functions, as in this work, 4 Gaussian points is precise enough to compute the scalar product of w_i and w_j in a linear tetrahedron. More quadrature points would only lead to a waste of computation time.
- However, Gaussian quadrature produces accurate results only if the function is well approximated by a polynomial. As one target element may overlap several source elements, w'_j is piecewise and risks having several intervals. In this case, the computation of the scalar product of w_i and w'_j is not accurate even if we take high-order quadrature rules, because w'_j can not be presented with one single polynomial over the target element. Nevertheless, since more quadrature points takes more samples of the source function, we can eventually improve the accuracy of the scalar product of w_i and w'_j.

2.2.2 *Numerical example*

The two implementation techniques are applied to mesh-to-mesh field transfers [56]. In particular, in this section, continuous analytical functions are used. The error of each projection can thus be computed in comparison to the analytical function.

We consider two tetrahedral meshes of the cubic domain $(0,1)^3$ (Figure 13).

Remark 5 *Unlike Section 2.1.6, here the two meshes used have no parental relation; i. e. they are both randomly generated.*

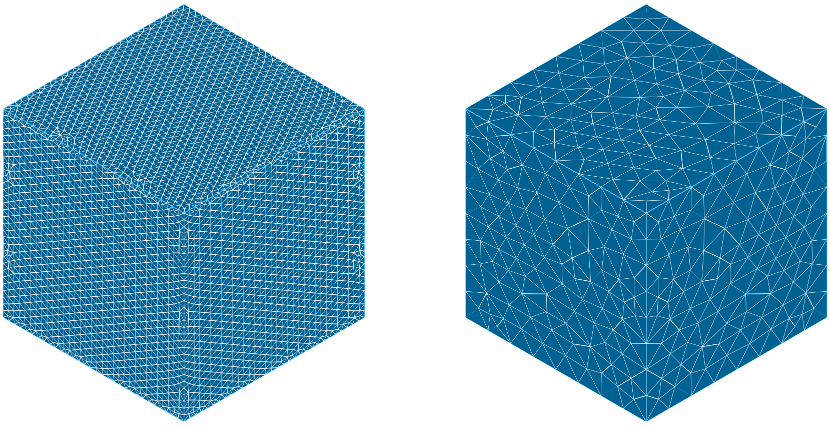

Figure 13: Meshes used: M1 (58k elements) and M2 (4k elements).

In the following, skin-effect-current-density-like exponential analytical functions will be considered. Significant value variations are located in only 25% of the volume of the studied domain. Concerning the sampling-integration technique over target elements, in this work the quadrature rules with 4, 16 and 29 Gaussian points are used for tetrahedrons.

Let the norm of the difference between the projected field and the analytical function be the absolute error. The relative error is the ratio of the absolute error to the norm of the analytical function. The two projection techniques are compared in Table 12 for accuracy and in Table 13 for computation time.

Table 12: Relative errors of projections (w.r.t. the analytical function), calculated in the continuous-to-discrete projections and the M1-to-M2 projections using different projection techniques.

		node	edge	facet
		e^{-12x}	$[e^{-12y}, 0, 0]$	$[e^{-12x}, 0, 0]$
source solution on M1		1.25%	11.96%	10.37%
reference solution on M2		6.20%	24.21%	23.32%
M1→M2	intersection	6.05%	23.79%	21.53%
	4 Gaussian points sampling	9.30%	24.90%	23.30%
	16 Gaussian points sampling	7.83%	24.34%	22.55%
	29 Gaussian points sampling	7.69%	24.20%	22.46%

In Table 12, "source solution on M1" and "reference solution on M2" are obtained using continuous-to-discrete projections. The M1-to-M2 projections can then be obtained from "source solution on M1" with the two presented implementation techniques. As explained before, we do not project from M2 to M1, because M1 is finer and the projection does not improve the accuracy.

Table 13: Computation time used in the M1-to-M2 projections using different techniques.

		node e^{-12x}	edge $[e^{-12y}, 0, 0]$	facet $[e^{-12x}, 0, 0]$
M1→M2	intersection	92s	192s	117s
	4 Gaussian points sampling	1.7s	1.7s	1.7s
	16 Gaussian points sampling	4.5s	4.6s	4.7s
	29 Gaussian points sampling	10.0s	10.3s	10.2s

Mathematical error estimation for the projections can be found in [47, 54]. For a H^2-regular analytical function, the optimal error is of order h^2 for nodal projections and order h for edge and facet elements. This is why the projection error at edge and facet elements is relatively more important than at the nodes. Moreover, error for the facets are slightly smaller than for edges because the number of unknowns is greater; e. g. M2 has 5713 edges but 8736 facets.

As the source field on M1 gives good accuracy, the M1-to-M2 projections using intersection is more accurate in comparison to the reference solution on M2.

Using the approximate integration over the target mesh (the 3 last lines in Table 12), the optimality of the solution in comparison to the reference solution on M2 can no longer be ensured. Although more quadrature points can indeed improve the accuracy of the result, the projection with the sampling-integration algorithm over the target mesh is always suboptimal compared with intersection of meshes. Nevertheless, the sampling-integration algorithm over target elements presents the important advantage of involving lower computation time.

2.2.3 *Conclusion*

Projection can be applied to mesh-to-mesh transfers of physical fields. In practice the accurate implementation of the projection requires the intersection of source and target meshes and is computationally expensive. Another solution is to directly integrate over target elements, by means of sampling the source field distribution on quadrature points. Projection with the latter implementation technique is in general less accurate than mesh-intersecting. However, the accuracy can be improved using high-order quadrature rules.

2.3 ENERGETIC FORMULATIONS FOR ELECTROMAGNETIC FIELDS

In the previous sections, projection tools transfer fields between different meshes. We have also compared the different implementation techniques. Now we can study formulations which are better adapted for electromagnetic fields.

Remark 6 *In this work, we concentrate on the projection of electromagnetic fields. The result of the electromagnetic model (e. g. electromagnetic fields), is projected onto a second mesh and serves as the* *source term for mechanical or thermal models. However, under the assumption of weak interaction, no projection is realized in the opposite direction (i.e. no major influence from mechanical / thermal models to electromagnetic models).*

In practice, depending on the nature of the electromagnetic field to be projected, projections can be carried out in the different Sobolev spaces. For example, $\mathbf{L}^2(\mathscr{D})$ projections can generally be used to find the approximation of a vector field on the target mesh, with which the $\mathbf{L}^2(\mathscr{D})$-norm of their difference is minimized. For the fields with finite curl (e.g. the magnetic and electric fields), the projections can also be carried out in $\mathbf{H}(\mathbf{curl}, \mathscr{D})$. A $\mathbf{H}(\mathbf{curl}, \mathscr{D})$-projection reduces the $\mathbf{H}(\mathbf{curl}, \mathscr{D})$-norm of the difference between our solution and the given field, i.e. the difference on the fields but also on their curls. For example, the $\mathbf{H}(\mathbf{curl}, \mathscr{D})$-projection of a magnetic field, returns an approximated field with similar current density, which is its curl.

However, in multi-physics problems, after the transfer, we may need additional information other than distribution of the fields. The accuracy of the energy distribution is often crucial.

For instance, in electrical machines at low speeds range, the magnetic forces are the main sources for mechanical vibrations and acoustic noises. In terms of numerical modeling, these forces can be calculated from the distribution of magnetic fields and used as excitations in the mechanical computation. Assuming that the projection of the magnetic field is used between the magnetic and mechanical problems, the magnetic forces are thus calculated from the projected field on the mechanical mesh. As forces are the derivatives of the magnetic energy with respect to virtual displacements [57], the projection used should ensure great accuracy with respect to the distribution of the magnetic energy. Otherwise, the non-conservation of energetic quantities may lead to errors regarding magnetic forces and thus errors for the entire magneto-mechanical modeling.

Another example concerns the magneto-thermal modeling. The eddy currents are important sources for the joule heating in electrical machines. In order to calculate the magnetic and thermal problems on different meshes, the transfer used should ensure the accuracy regarding ohmic losses.

Here we focus on the mesh-to-mesh energy-conserving projection of electromagnetic fields. The energetic formulations are investigated for magneto-static problems [58] as well as harmonic eddy current problems [59]. The formulations with respect to nonlinear magnetic media, are then presented.

2.3.1 *Magneto-static problems*

In order to solve magneto-static problems, different formulations can be employed, e.g. formulations based on scalar or vectorial potentials (Section 1.1.2). Consequently, in the numerical result either the magnetic field or the magnetic flux density better respects the physical properties. In the following, we assume that only such discrete fields are projected.

We denote by $\mathbf{H}_s$ and $\mathbf{B}_s$ the fields obtained on the source mesh and by $\mathbf{H}_t$ and $\mathbf{B}_t$ the fields to be calculated on the target mesh. The magneto-static energetic norms of the interpolation error are defined as:

$$\varepsilon_{\mathbf{H}} = \int_{\mathscr{D}} \frac{\mu}{2} |\mathbf{H}_t - \mathbf{H}_s|^2 \, d\tau \tag{65}$$

$$\varepsilon_{\mathbf{B}} = \int_{\mathscr{D}} \frac{1}{2\mu} |\mathbf{B}_t - \mathbf{B}_s|^2 \, d\tau \tag{66}$$

In comparison to the classic inner norms (Section 2.1.1), here the norms to be minimized are weighted by the distribution of the magnetic permeability or reluctivity.

On the target mesh, using Whitney elements in 3D, $\mathbf{H}_t$ and $\mathbf{B}_t$ are discretized at the edge and facet element spaces respectively (Section 1.5):

$$\mathbf{H}_t = \sum_{i=1}^{E} \mathbf{w}_i^e h_i \text{ and } \mathbf{B}_t = \sum_{i=1}^{F} \mathbf{w}_i^f b_i \tag{67}$$

where $\mathbf{w}_i^e$ (resp. $\mathbf{w}_i^f$) and h_i (resp. b_i) are the shape functions and the values of $\mathbf{H}_t$ (resp. $\mathbf{B}_t$) associated with the $i-th$ edge (resp. facet). E and F are the number of edge and facet elements respectively.

To project fields onto a target mesh with respect to the magnetic energy, weak formulations based on the minimization of the energetic norm are developed. In (65), the energetic error norm is minimized when its derivatives with respect to all degrees of freedom are equal to zero. Thus for each edge of the target mesh $\forall i \in \{1..E\}$:

$$\frac{\partial}{\partial h_i} \int_{\mathscr{D}} \frac{\mu}{2} |\mathbf{H}_t - \mathbf{H}_s|^2 \, d\tau = 0 \tag{68}$$

$$\int_{\mathscr{D}} \frac{\mu}{2} \frac{\partial}{\partial h_i} (\mathbf{H}_t^2 + \mathbf{H}_s^2 - 2\, \mathbf{H}_t \cdot \mathbf{H}_s) d\tau = 0 \tag{69}$$

$$\int_{\mathscr{D}} \mu (\mathbf{w}_i^e \cdot \mathbf{H}_t - \mathbf{w}_i^e \cdot \mathbf{H}_s) d\tau = 0 \tag{70}$$

Finally, the matrix equation to be solved can be written:

$$[C]\,[h] = [F] \tag{71}$$

where

$$C_{ij} = \int_{\mathscr{D}} \mu \mathbf{w}_i^e \cdot \mathbf{w}_j^e d\tau, \; F_i = \int_{\mathscr{D}} \mu \mathbf{w}_i^e \cdot \mathbf{H}_s d\tau \tag{72}$$

and $[h]$ is the vector of the degrees of freedom to be calculated.

A similar demonstration can be applied to (66) for the projection of $\mathbf{B}_s$ with respect to the magnetic energy: $\forall i \in \{1..F\}$

$$\int_{\mathscr{D}} \frac{1}{\mu} (\mathbf{w}_i^f \cdot \mathbf{B}_t - \mathbf{w}_i^f \cdot \mathbf{B}_s) d\tau = 0 \tag{73}$$

2.3.2 *Eddy current problems*

For eddy current problems, either magnetic (e. g. $\mathbf{T} - \Omega$) or electric (e. g. $\mathbf{A} - \phi$) harmonic formulations can be used in order to calculate the harmonic fields. On the source mesh, either $\mathbf{H}_s$ or $\mathbf{E}_s$ better respects the physical properties. Thus, depending on the formulation used, the mesh-to-mesh energetic error norm to be minimized can be defined as [60, 61, 62]:

$$\varepsilon_\mathbf{H} = \int_{\mathscr{D}} \mu \left|\mathbf{H}_t - \mathbf{H}_s\right|^2 d\tau + \int_{\mathscr{D}_c} \frac{1}{\sigma\omega} \left|\mathbf{curl}\ \mathbf{H}_t - \mathbf{curl}\ \mathbf{H}_s\right|^2 d\tau \tag{74}$$

$$\varepsilon_\mathbf{E} = \int_{\mathscr{D}_c} \frac{\sigma}{\omega} \left|\mathbf{E}_t - \mathbf{E}_s\right|^2 d\tau + \int_{\mathscr{D}} \frac{1}{\mu} \left|\frac{\mathbf{curl}\ \mathbf{E}_t - \mathbf{curl}\ \mathbf{E}_s}{\omega}\right|^2 d\tau \tag{75}$$

with ω the angular pulsation. Here both norms contain the magnetic energy in the studied domain $\mathscr{D}$ as well as the joule heating in conducting domain $\mathscr{D}_c$.

On the target mesh, edge elements provide sound discrete spaces for $\mathbf{H}_t$ and $\mathbf{E}_t$. Weak formulations can then be obtained by the minimization of the energetic norm (74): $\forall i \in \{1..E\}$

$$\int_{\mathscr{D}} \mu(\mathbf{w}_i^e \cdot \mathbf{H}_t - \mathbf{w}_i^e \cdot \mathbf{H}_s) d\tau + \int_{\mathscr{D}_c} \frac{1}{\sigma\omega} (\mathbf{curl}\ \mathbf{w}_i^e \cdot \mathbf{curl}\ \mathbf{H}_t - \mathbf{curl}\ \mathbf{w}_i^e \cdot \mathbf{curl}\ \mathbf{H}_s) d\tau = 0 \tag{76}$$

or in the case of electric formulations (75): $\forall i \in \{1..E\}$

$$\int_{\mathscr{D}_c} \frac{\sigma}{\omega} (\mathbf{w}_i^e \cdot \mathbf{E}_t - \mathbf{w}_i^e \cdot \mathbf{E}_s) d\tau + \int_{\mathscr{D}} \frac{1}{\mu\omega^2} (\mathbf{curl}\ \mathbf{w}_i^e \cdot \mathbf{curl}\ \mathbf{E}_t - \mathbf{curl}\ \mathbf{w}_i^e \cdot \mathbf{curl}\ \mathbf{E}_s) d\tau = 0 \tag{77}$$

Equation (76) gives rise to the following matrix equation:

$$\left([C] + \left[C^{curl}\right]\right)[h] = [F] + \left[F^{curl}\right] \tag{78}$$

where [C] and [F] are the same matrices as in magneto-static problems and

$$C_{ij}^{curl} = \int_{\mathscr{D}_c} \frac{1}{\sigma\omega} \mathbf{curl}\ \mathbf{w}_i^e \cdot \mathbf{curl}\ \mathbf{w}_j^e d\tau \tag{79}$$

$$F_i^{curl} = \int_{\mathscr{D}_c} \frac{1}{\sigma\omega} \mathbf{curl}\ \mathbf{w}_i^e \cdot \mathbf{curl}\ \mathbf{H}_s d\tau \tag{80}$$

The sum of [C] and $[C^{curl}]$ is a positive-definite matrix.

A similar matrix system can be obtained from (77) in order to project $\mathbf{E}_s$.

2.3.3 *Numerical example (linear media)*

The proposed projection formulations are applied in an academic example (Figure 14 [59]). The studied domain is composed of two face-to-face cylindrical iron cores. Iron core 1 is wound around by an excitation coil. Here all media have linear magnetic characteristics. `code_Carmel` is used in order to solve the electromagnetic model.

Two meshes are considered: M1 (234k elements) and M2 (29k elements). In order to carry out the mesh-to-mesh transfer, M1 is used as the source mesh to solve the magnetic problem and M2 is considered as the target mesh for the projection.

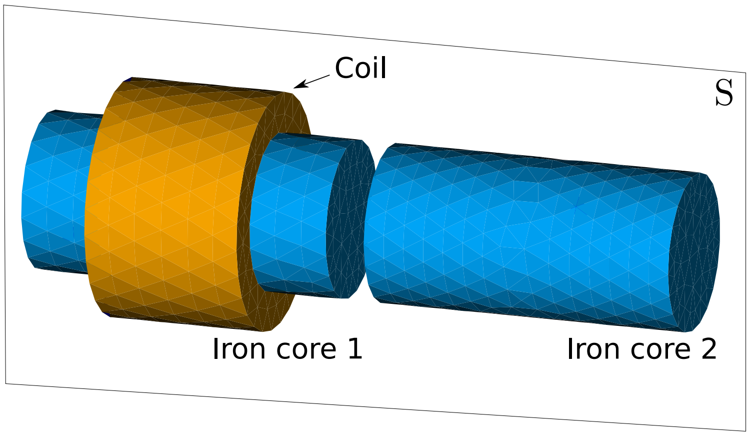

Figure 14: Geometry of the studied example. S is the clipping plane used to illustrate the result.

2.3.3.1 *Magneto-static problem*

First, a constant current is applied in the coil. Given Ampere's law, magnetic fields appear and the two iron cores tend to attract each other.

The magneto-static problem is solved on M1 using the scalar potential formulation. The calculated magnetic field $\mathbf{H}_s$, is then projected to M2 using the $\mathbf{L}^2(\mathscr{D})$-projection (52) and the energetic formulation (70).

The obtained magnetic field $\mathbf{H}_t$ on M2 is presented in Figure 15 on a clipping plane. Here the two projection methods return very similar distributions for $\mathbf{H}_t$.

The $\mathbf{B}_t$ fields can then be calculated from the projected $\mathbf{H}_t$ fields using the magnetic constitutive law. Although the projected magnetic field appears to be appropriate, the $\mathbf{L}^2(\mathscr{D})$-projection fails to provide a correct distribution of $\mathbf{B}_t$ at the boundary of the iron cores (Figure 16(a)). The advantage of the energetic formulation is shown by the correct distribution of the corresponding $\mathbf{B}_t$ (Figure 16(b)).

Table 14 compares the magnetic energy and interaction force calculated on M1, M2 and then by M1-to-M2 projection. The energy-conserving projection allows us to calculate magnetic forces on M2 from the projected $\mathbf{H}_t$ field (Figure 17). As expected, iron core 2 is attracted by iron core 1.

Table 14: Validation of the energetic projection approach (magneto-static problem).

	calculated on M1	calculated on M2	M1→M2 energetic proj.
magnetic energy (mJ)	364	361	366
interaction force (N)	2.61	2.91	2.66

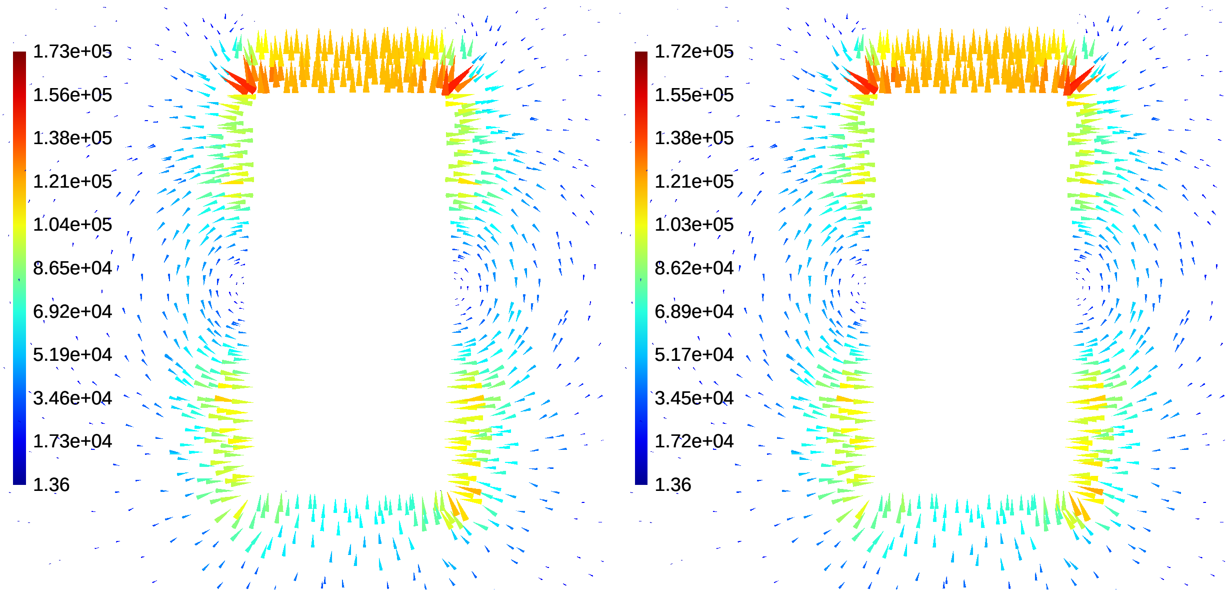

(a) (b)

Figure 15: M1-to-M2 projected $\mathbf{H}_t$ (A/m) field on iron core 1 (on a clipping plane), using: (a) $\mathbf{L}^2(\mathscr{D})$-projection. (b) Energetic projection.

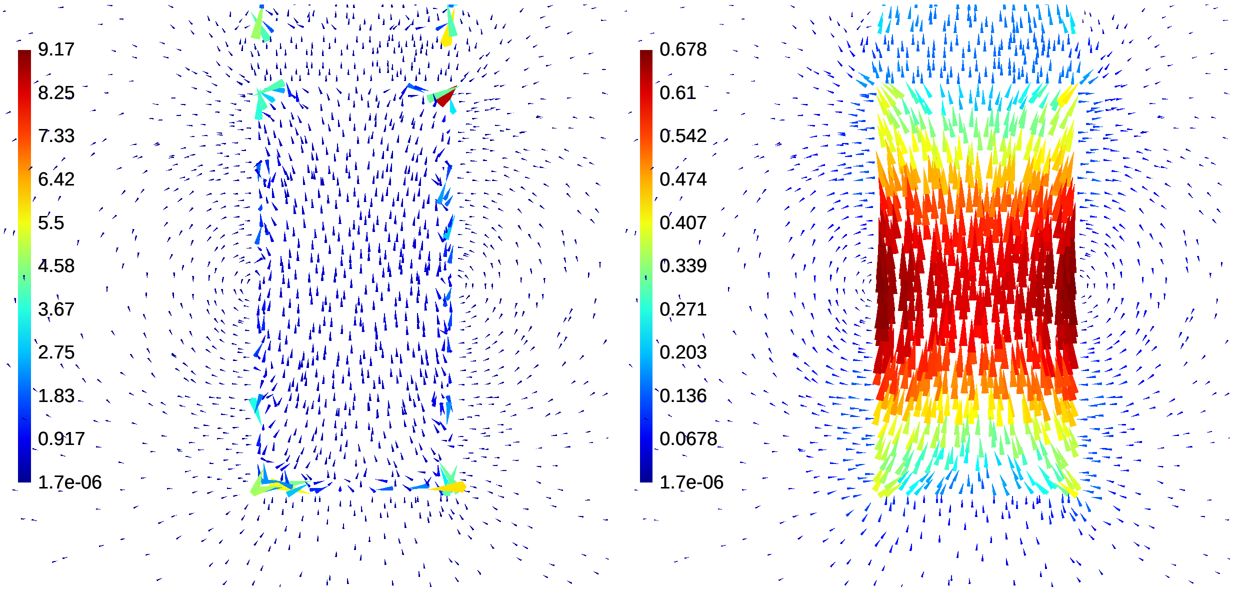

(a) (b)

Figure 16: Distribution of $\mathbf{B}_t$ (T) on a clipping plane, calculated from the projected $\mathbf{H}_t$ fields (Figure 15). (a) $\mathbf{L}^2(\mathscr{D})$-projection. (b) Energetic projection.

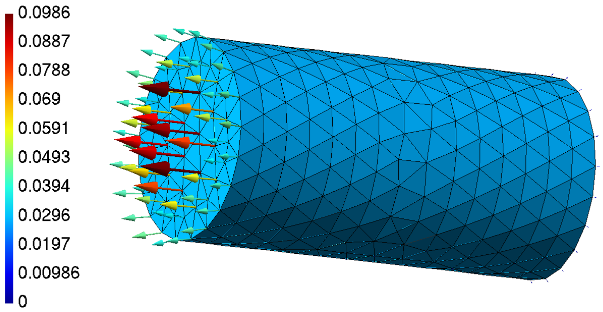

Figure 17: Magnetic forces (N) on iron core 2. They are calculated by applying the virtual work method on the projected $\mathbf{H}_t$ field using the energetic formulation.

2.3.3.2 *Eddy current problem*

Second, a sinusoidal current is applied as excitation. In this case, eddy currents appear in the iron cores.

On M1, the magneto harmonic problem is solved with the magnetic $\mathbf{T}$-Ω formulation. The obtained magnetic field $\mathbf{H}_s$, is then projected onto M2 using the presented energetic projection (76).

Table 15 presents the energetic values solely calculated on M1 and M2 for reference, and then those issued from M1-to-M2 projections. Compared with the magneto-static case (Table 14), here the accuracy is slightly lower in terms of magnetic energy. A difference up to 7% can be observed between the energy obtained on M2 and that deduced from projected $\mathbf{H}_t$. However, the energetic formulation (76), aims to minimize the sum of the differences with respect to the magnetic energy and joule heating.

Table 15: Validation of the energetic projection approach (eddy current problem).

	calculated on M1	calculated on M2	M1→M2 energetic proj.
magnetic energy (mJ)	370.7	380.8	353.5
ohmic losses (mW)	13.5	14.3	12.8
magnetic energy + joule heating per period (mJ)	372.8	383.1	355.5

Similar to the static case, the $\mathbf{L}^2(\mathscr{D})$ projection and the $\mathbf{H}(\mathbf{curl}, \mathscr{D})$-projection of $\mathbf{H}_s$ are capable of returning the approximated distribution on the target mesh. Important errors can however be remarked with respect to the distribution of the magnetic flux density and the eddy current density.

On the contrary, the obtained $\mathbf{H}_t$ field using the energetic formulation, ensures good accuracy regarding the magnetic flux density $\mathbf{B}_t$. Moreover, since $\textbf{curl}\ \mathbf{H} = \mathbf{J}$, the projection used gives good accuracy with respect to the eddy current (Figure 18) and thus the joule heating.

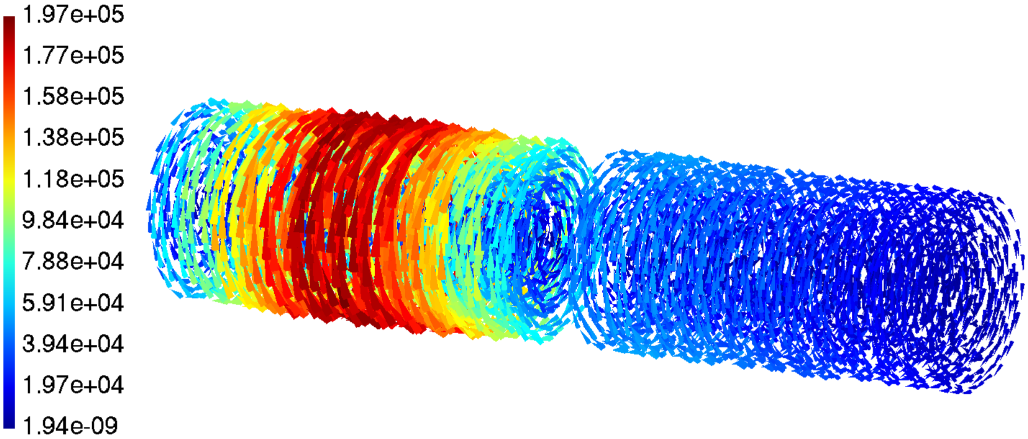

Figure 18: Eddy current density (A/m^2) in the two iron cores. This is calculated from the "energetically" projected $\mathbf{H}_t$ field.

2.3.4 *Nonlinear magnetic media*

We can now take into account the nonlinearity of magnetic media. The aim here is to project a magnetic quantity from one mesh to another, and to conserve the magnetic energy with respect to the nonlinear magnetic permeability. To ensure the simplicity of our illustration, here we restrict ourselves to the case of static problems.

As before, we denote by $\mathbf{H}_s$ and $\mathbf{B}_s$ the fields obtained on the source mesh and by $\mathbf{H}_t$ and $\mathbf{B}_t$ the fields to be calculated on the target mesh. As was the case with linear permeability, the energetic error norm to be minimized for $\mathbf{H}$-conform formulation is defined as:

$$\varepsilon_{\mathbf{H}} = \int_{\mathscr{D}} \frac{\mu}{2} |\mathbf{H}_t - \mathbf{H}_s|^2 \, d\tau \tag{81}$$

which can be illustrated by the blue area in Figure 19(a).

For nonlinear media, we can define a similar area as the error norm to be minimized. In Figure 19(b), the $\mathbf{H}_s$-$\mathbf{B}_s$ point stands for the working point on the source mesh. We look for a working point $\mathbf{H}_t$-$\mathbf{B}_t$ on the target mesh, which minimizes the red area defined as:

$$\varepsilon_{\mathbf{H}}^{nl} = \int_{\mathscr{D}} \int_{\mathbf{H}_s}^{\mathbf{H}_t} [\mu(H_t)\mathbf{H}_t - \mu(H_s)\mathbf{H}_s] \, d\mathbf{H}_t \, d\tau \tag{82}$$

As in the linear cases, the $\mathbf{H}_t$ field is discretized at the edge elements of the target mesh:

$$\mathbf{H}_t = \sum_{i=1}^{E} \mathbf{w}_i^e h_i \tag{83}$$

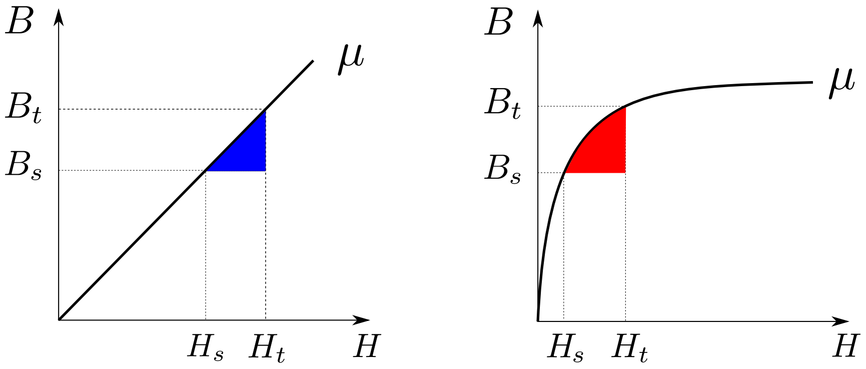

(a) Linear case

(b) Nonlinear case

Figure 19: Energetic error norms to be minimized for **H**-conform formulations.

When the energetic error norm is minimized, its derivatives with respect to all degrees of freedom are zero: $\forall i \in \{1..E\}$

$$\frac{\partial \varepsilon^{nl}_{\mathbf{H}}}{\partial h_i} = 0 \tag{84}$$

$$\int_{\mathscr{D}} \left\{ \frac{\partial}{\partial h_i} \int_{\mathbf{H}_s}^{\mathbf{H}_t} \left[\mu(H_t)\mathbf{H}_t - \mu(H_s)\mathbf{H}_s \right] d\mathbf{H}_t \right\} d\tau = 0 \tag{85}$$

$$\int_{\mathscr{D}} \left\{ \frac{\partial}{\partial \mathbf{H}_t} \int_{\mathbf{H}_s}^{\mathbf{H}_t} \left[\mu(H_t)\mathbf{H}_t - \mu(H_s)\mathbf{H}_s \right] d\mathbf{H}_t \right\} \cdot \frac{\partial \mathbf{H}_t}{\partial h_i} d\tau = 0 \tag{86}$$

$$\int_{\mathscr{D}} \left[\mu(H_t)\mathbf{H}_t - \mu(H_s)\mathbf{H}_s \right] \cdot \frac{\partial \mathbf{H}_t}{\partial h_i} d\tau = 0 \tag{87}$$

Thus the final equation to be solved can be written: $\forall i \in \{1..E\}$

$$\int_{\mathscr{D}} \left[\mathbf{w}_i^e \cdot \mu(H_t)\mathbf{H}_t - \mathbf{w}_i^e \cdot \mu(H_s)\mathbf{H}_s \right] d\tau = 0 \tag{88}$$

Or in matrix form:

$$[C^{nl}][h] = [F] \tag{89}$$

with

$$C_{ij}^{nl} = \int_{\mathscr{D}} \mu([h])\mathbf{w}_i^e \cdot \mathbf{w}_j^e d\tau \ , \ \ F_i = \int_{\mathscr{D}} \mu(H_s)\mathbf{w}_i^e \cdot \mathbf{H}_s d\tau \tag{90}$$

and $[h]$ the vector of the degrees of freedom to be solved.

A similar demonstration can be applied to the magnetic flux density **B** field, in order to realize its energetic projection with respect to the magnetic energy: $\forall i \in \{1..F\}$

$$\int_{\mathscr{D}} \left[\mathbf{w}_i^f \cdot \frac{1}{\mu(B_t)}\mathbf{B}_t - \mathbf{w}_i^f \cdot \frac{1}{\mu(B_s)}\mathbf{B}_s \right] d\tau = 0 \tag{91}$$

2.3.5 *Numerical example (nonlinear media)*

In order to illustrate the energetic projection regarding media with nonlinear permeability, let us consider an iron circuit wound by an excitation coil (Figure 20). Two meshes are used in this example: M1 (59k elements) and M2 (33k elements).

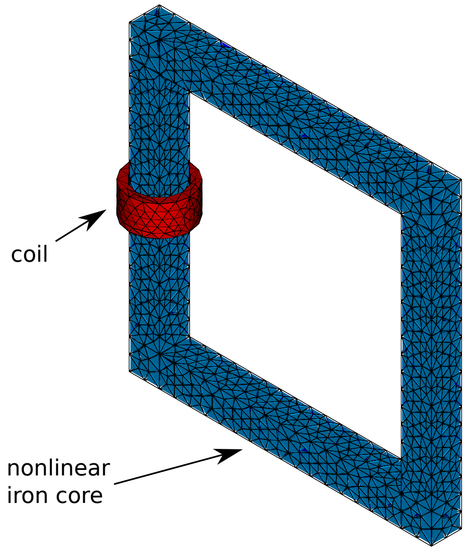

Figure 20: Mesh used for the studied example.

In this example the iron core has a nonlinear permeability. Its B versus H characteristic is shown in Figure 21.

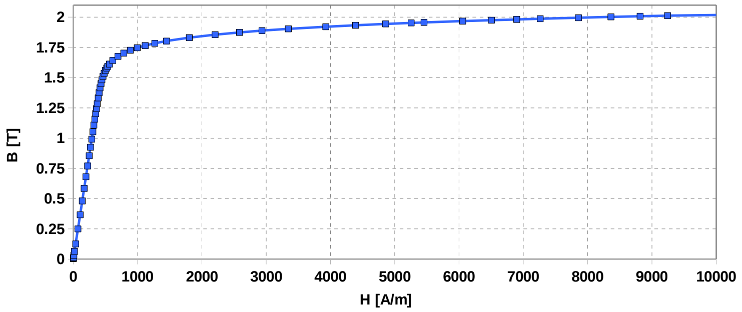

Figure 21: B-H characteristic of the iron circuit used here.

The medium used saturates at 2T. The B-H curve folds around 1.75T. In order to validate the proposed energetic formulations, three working points are considered by imposing different currents in the coil (using `code_Carmel`). In terms of the maximum value of the magnetic flux density, the first working point is located in the linear zone, the second one around 1.75T and the third in the saturated zone. For each working point, we first solve the magnetic problem on M1 with the scalar potential formulation (14). The obtained magnetic field is then used as $\mathbf{H}_s$ for the projection onto mesh M2 with the proposed energetic formulation (88).

Once the projection is carried out, from the obtained $\mathbf{H}_t$ we can calculate the corresponding $\mathbf{B}_t$ field and compare it to the source one $\mathbf{B}_s$.

In terms of implementation, here the nonlinear system (89) is solved with a fixed-point algorithm. For the first iteration, we replace the nonlinear permeability with a linear approximation. Then with the obtained result of step 1 (denoted by $[h]^1$), we update the $[C^{nl}]$ matrix with the nonlinear permeability and solve the updated system for $[h]^2$. This updating and solving iteration continues until the difference between two steps (i. e. $\left\|[h]^n - [h]^{n-1}\right\|$) is smaller than the imposed tolerance.

In the case of the second working point (i. e. B_{max} around 1.75T), the distribution of $\mathbf{B}_s$ and $\mathbf{B}_t$ fields are shown in Figure 22.

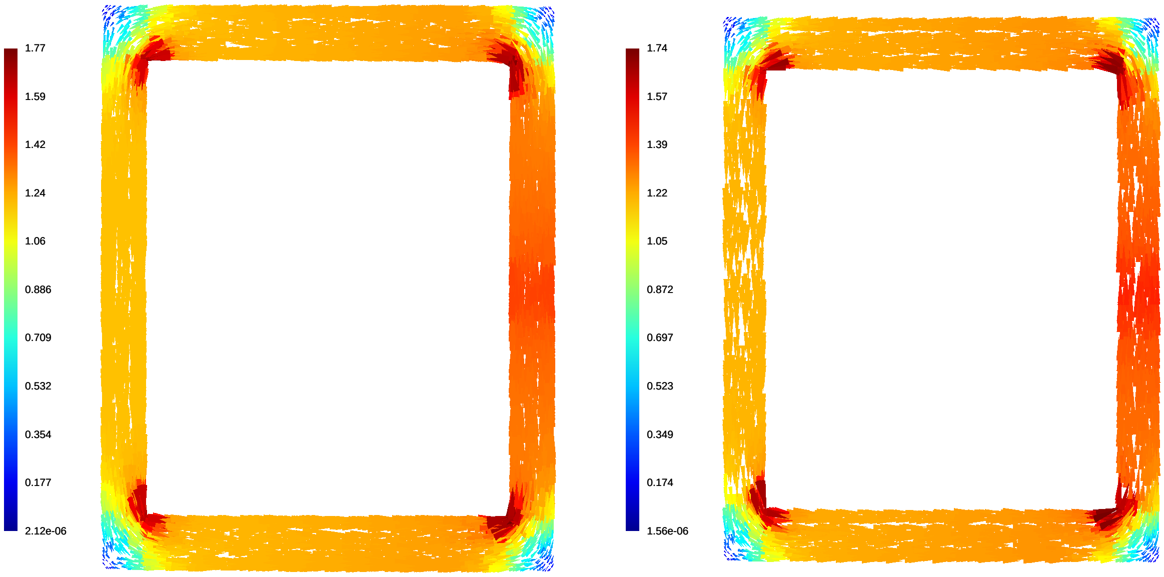

(a) $\mathbf{B}_s$ field (b) $\mathbf{B}_t$ field

Figure 22: Comparison of the $\mathbf{B}_s$ field on the source mesh and the $\mathbf{B}_t$ field on the target mesh. Here the $\mathbf{B}_t$ field is calculated from the "energetically" projected H_t field.

Table 16 compares the maximum values of $\mathbf{B}_s$ and $\mathbf{B}_t$, for the three working points. The number of iterations for solving the nonlinear system, is also given.

Table 16: Comparison of the maximum values of $\mathbf{B}_s$ and $\mathbf{B}_t$, for the projections regarding nonlinear magnetic media.

working point	$\lvert\mathbf{B}_s\rvert_{max}$ (T)	$\lvert\mathbf{B}_t\rvert_{max}$ (T)	Nb. of iterations
1	0.468	0.456	3
2	1.77	1.74	9
3	2.05	2.01	22

For all the three working points, the maximum values of $\mathbf{B}_s$ and $\mathbf{B}_t$ are very close (i. e. differences are smaller than 2.6%). In general, a greater $|\mathbf{B}_s|_{max}$ requires more iterations in order to solve the nonlinear system using energetic projections. As a matter of fact, in Figure 19(b), we can remark that the red part becomes very flat in the saturated zone. In this case, even a great variation of $\mathbf{H}_t$ has little influence on the larger of the red areas. A greater number of iterations is needed to find the result.

2.3.6 *Conclusion*

In order to transfer electromagnetic fields between different meshes, energy-conserving projection methods are presented in this section. The definition of energetic norms is given for magneto-static problems as well as harmonic eddy current problems. Nonlinear cases are then investigated in order to take into account nonlinear magnetic permeability.

For magneto-mechanical and magneto-thermal modeling, the presented formulations ensure accuracy regarding energy distribution for the mesh-to-mesh transfer of electromagnetic fields. In the studied example, the projected magnetic fields can be used for the computation of forces and joule heating.

3

APPLICATIONS

In Chapter 2, we presented field projection methods on finite element overlapping domains. To illustrate some of their applications, in this chapter the projection tools are applied to the discretization of uniform analytical current densities. Subsequently, using the computational models presented in Chapter 1, several weak-coupling magneto-mechanical or magneto-thermal examples are studied. Mesh-to-mesh filed projections are employed to ensure the model coupling.

We begin with two conductor geometries for the discretization of uniform analytical current densities. Different projection formulations are compared with respect to the quality of the obtained field. Secondly, the computational models are tested with a magneto-mechanical example of simple geometry, for which we can deduce the analytical field distributions. The electromagnetic and mechanical problems are solved on a common mesh and then on different meshes with mesh-to-mesh field projections. Thirdly, we study the mechanical deformations of an elastic plate due to the attraction forces of an electromagnet. The projection formulations as well as their implementation techniques are compared, in terms of their influences on the result of the entire magneto-mechanical problem. Finally, a double-excitation synchronous alternator from Valeo is considered. We propose a solution strategy in order to calculate the vibrations on the stator due to the magnetic forces.

In the following, `code_Carmel`, `code_Aster` and `Syrthes` are used to compute the electromagnetic, mechanical and thermal models respectively.

3.1 DISCRETIZATION OF UNIFORM ANALYTICAL CURRENT DENSITIES

In computational electromagnetism, we aim to calculate the field distribution produced by excitations (e. g. currents, charges, magnetic flux, etc.). The accurate discretization of excitation fields is thus very important for the purpose of setting up the correct discrete problem.

Let us focus on the discretization of given uniform current densities. Besides the discrete values to be calculated, the difficulty in such processing is to satisfy specific physical properties - i. e. the obtained current densities should be divergence-free. However, the target mesh often has flaws (e. g. approximation of a circular line with several straight lines). This implies that the uniformity and the zero divergence of the discrete field can not be satisfied at the same time. Several solutions can be found in the literature regarding this subject [63, 64, 65, 66, 67, 68].

The projection methods presented in this manuscript (Section 2.1), are also convenient tools for discretising excitation fields.

3.1.1 *Formulations*

Let us consider a uniform analytical current density $\mathbf{J}_e$ defined on the domain $\mathscr{D}$. It is divergence-free: $\operatorname{div} \mathbf{J}_e = 0$.

The aim of the discretization of $\mathbf{J}_e$, is to find in the facet space a discrete field $\mathbf{J}_h = \sum_F \mathbf{w}_i^f X_i$ such that the norm of their difference is minimized. This is the same concept we met in field projections.

Since both $\mathbf{J}_e$ and $\mathbf{J}_h$ are members of $\mathbf{H}(\operatorname{div}, \mathscr{D}) \subset \mathbf{L}^2(\mathscr{D})$, two formulations can be applied:

- $\mathbf{L}^2(\mathscr{D})$ projection

$$\int_{\mathscr{D}} \|\mathbf{J}_h - \mathbf{J}_e\|^2 \rightarrow \min \tag{92}$$

- $\mathbf{H}(\operatorname{div}, \mathscr{D})$ projection

$$\int_{\mathscr{D}} (\|\mathbf{J}_h - \mathbf{J}_e\|^2 + \|\operatorname{div} \mathbf{J}_h - \operatorname{div} \mathbf{J}_e\|^2) \rightarrow \min \tag{93}$$

After the application of the Galerkin method and test functions, the weak formulations to be solved are:

- $\mathbf{L}^2(\mathscr{D})$ projection

$$(\psi_h, \mathbf{J}_h)_{\mathbf{L}^2(\mathscr{D})} = (\psi_h, \mathbf{J}_e)_{\mathbf{L}^2(\mathscr{D})}, \ \forall \psi_h \in \mathbf{L}_h^2(\mathscr{D}) \tag{94}$$

- $\mathbf{H}(\operatorname{div}, \mathscr{D})$ projection

$$\langle \psi_h, \mathbf{J}_h \rangle_{\mathbf{H}(\operatorname{div}, \mathscr{D})} = \langle \psi_h, \mathbf{J}_e \rangle_{\mathbf{H}(\operatorname{div}, \mathscr{D})}, \ \forall \psi_h \in \mathbf{H}_h(\operatorname{div}, \mathscr{D}) \tag{95}$$

The $\mathbf{L}^2(\mathscr{D})$ projection returns a discrete field with minimized difference with respect to the analytical field. The $\mathbf{H}(\operatorname{div}, \mathscr{D})$ projection approximates not only the field but also the divergence.

As we wish to obtain a field of zero divergence, another natural idea is to use the following property in the de Rham complex (35): the image of $\mathbf{H}(\mathbf{curl}, \mathscr{D})$ in $\mathbf{H}(\operatorname{div}, \mathscr{D})$ by **curl** is the kernel of the div operator. The divergence-free $\mathbf{J}_h$ field can be expressed as a curl:

$$\mathbf{J}_h = \mathbf{curl}\ \mathbf{K}_h \tag{96}$$

where $\mathbf{K}_h$ is a vector potential to be determined at the edge elements: $\mathbf{K}_h = \sum_E \mathbf{w}_i^e Y_i$.

The problem to be solved becomes:

$$\int_{\mathscr{D}} \|\mathbf{curl}\ \mathbf{K}_h - \mathbf{J}_e\|^2 \rightarrow \ \min \tag{97}$$

or in the weak form:

$$(\mathbf{curl}\ \psi_h, \mathbf{curl}\ \mathbf{K}_h)_{\mathbf{L}^2(\mathscr{D})} = (\mathbf{curl}\ \psi_h, \mathbf{J}_e)_{\mathbf{L}^2(\mathscr{D})}\ ,\ \forall \psi_h \in \mathbf{H}(\mathbf{curl}, \mathscr{D}) \tag{98}$$

Here (98) can be understood as a projection using the semi-norm of $\mathbf{H}(\mathbf{curl}, \mathscr{D})$ - i. e. the module defined as:

$$\forall \mathbf{f} \in \mathbf{H}(\mathbf{curl}, \mathscr{D}),\ |\mathbf{f}|_{\mathbf{H}(\mathbf{curl}, \mathscr{D})} = \left[\int_{\mathscr{D}} \mathbf{curl}\ \mathbf{f} \cdot \mathbf{curl}\ \mathbf{f} \right]^{1/2} \tag{99}$$

which contains only half of the $\mathbf{H}(\mathbf{curl}, \mathscr{D})$-norm.

Physically, (98) is equivalent to solving a magneto-static problem using the vector potential formulation. Unlike the normal full-norm projections, a differential equation needs to be solved. Boundary conditions must be added in order to ensure the unicity of the solution.

3.1.2 *Applications*

For illustration purposes, two geometries of conductors are considered (Figure 23). Uniform analytical current densities are defined in these conductors. For simplicity, the module of the analytical current densities is fixed at $1A/m^2$.

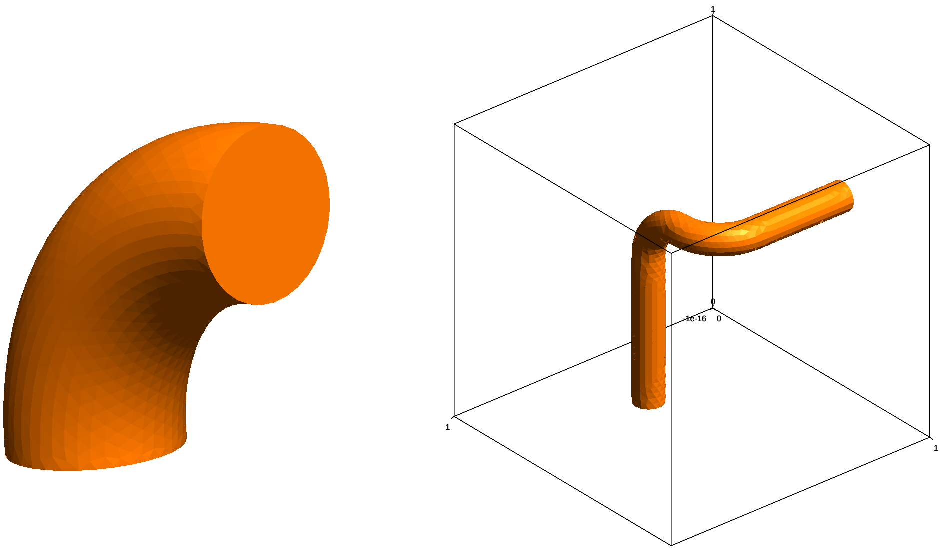

(a) Bent conductor (b) Twisted conductor

Figure 23: Two conductor geometries for the discretization of excitation current densities. The mesh of the bent conductor only contains the conductor. For the twisted conductor, an air box also is used.

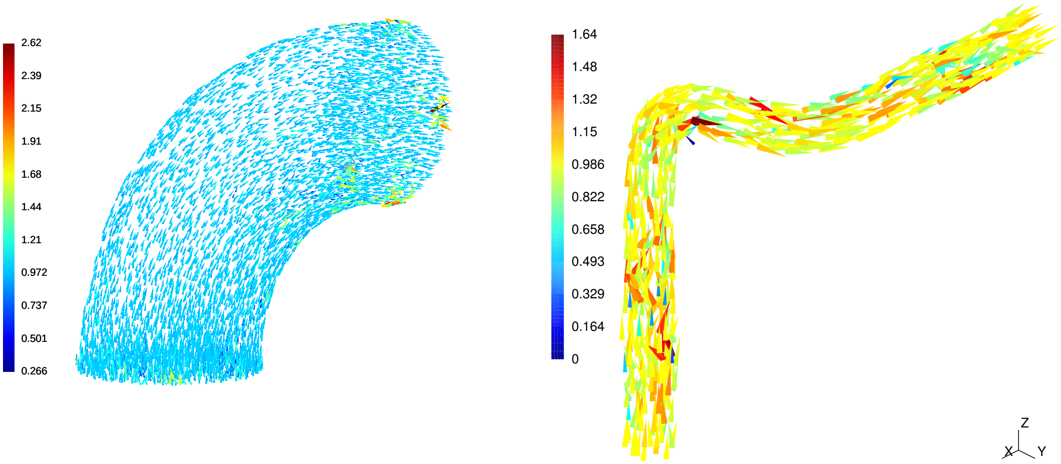

(a) Bent conductor (b) Twisted conductor

Figure 24: Discretized current densities, obtained using edge and facet trees (code_Carmel v1.7.2).

Before proceeding the projection approaches, in Figure 24 we present the obtained discrete $\mathbf{J}_h$ field using edge and facet tree techniques [69, 70].

Edge and facet tree techniques verify the divergence in each element and calculate iteratively the current flowing through each facet. The advantage of such techniques is that the divergence is ensured to be zero. However, in the example of the bent conductor (Figure 24(a)), all local errors are brought to one boundary of the conductor. The maximum value $2.62\mathrm{A}/\mathrm{m}^2$ represents a local error of 162%. For the twisted conductor (Figure 24(b)), the obtained current density is barely "uniform".

Figure 25 and Figure 26 illustrate the results obtained using projection methods.

In Figure 25, (a) and (b) have no significant difference: both the $\mathbf{L}^2(\mathscr{D})$ projection and the $\mathbf{H}(\mathrm{div}, \mathscr{D})$ projection are capable to discretise the analytical current density at facet elements. The maximum local error is 3% for the $\mathbf{L}^2(\mathscr{D})$ projection and 3.2% for $\mathbf{H}(\mathrm{div}, \mathscr{D})$. In this case the $\mathbf{H}(\mathrm{div}, \mathscr{D})$ projection is much better than the $\mathbf{L}^2(\mathscr{D})$ projection, because the obtained divergence is hundreds of times smaller (comparing (d) with (c)).

When applied to the twisted conductor, the $\mathbf{H}(\mathrm{div}, \mathscr{D})$ projection shows a similar performance (Figure 26). The local error regarding the current density is smaller than for the edge and facet tree techniques. Minor divergences, can however be remarked in the conductor.

We can also apply the $\mathbf{H}(\mathbf{curl}, \mathscr{D})$ semi-norm projection (98) to both geometries. Boundary conditions are added such that $\mathbf{K}_h = \mathbf{0}$ at all boundaries of the studied domain.

In Figure 27 and Figure 28, the calculated $\mathbf{K}_h$ fields fill the study domain. As this time the discrete current densities are described using curls, they are ensured to be divergence-free.

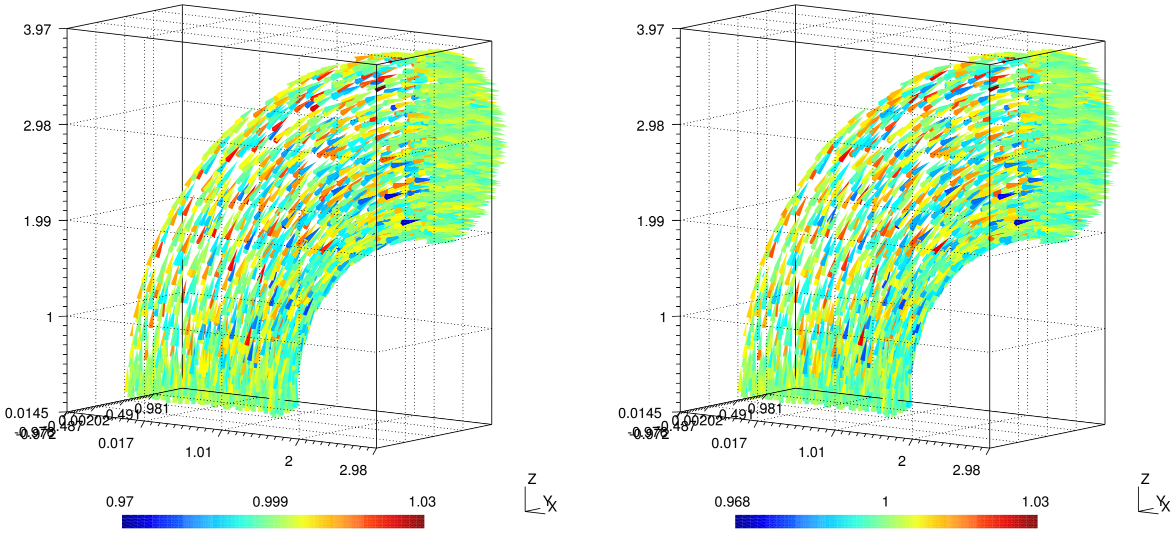

(a) $\mathbf{J}_h$, obtained using (94)

(b) $\mathbf{J}_h$, obtained using (95)

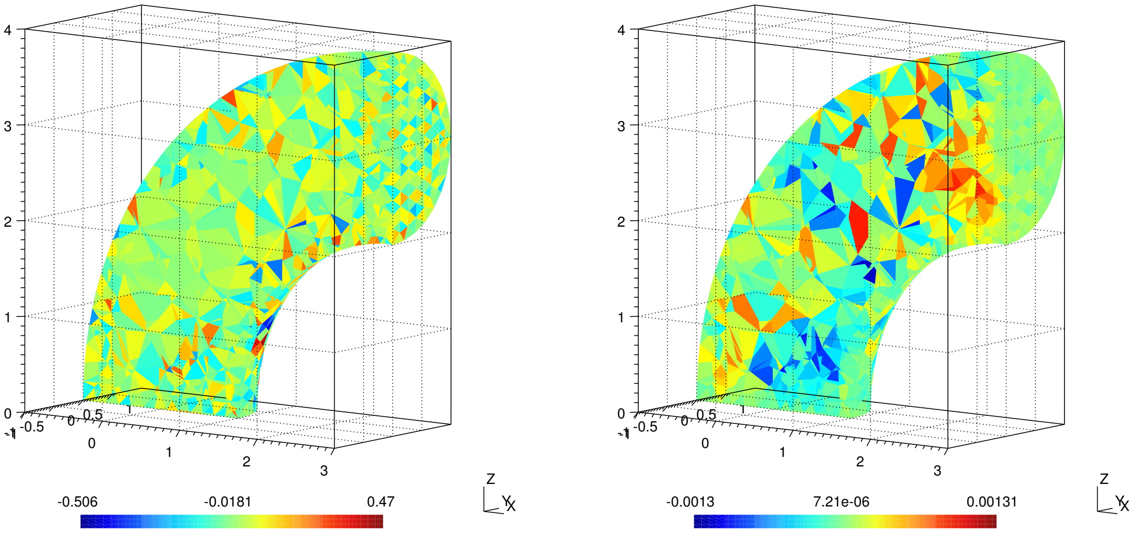

(c) div $\mathbf{J}_h$, obtained using (94)

(d) div $\mathbf{J}_h$, obtained using (95)

Figure 25: Discretized current densities and their divergence, obtained using full-norm projection methods (bent conductor, clipped).

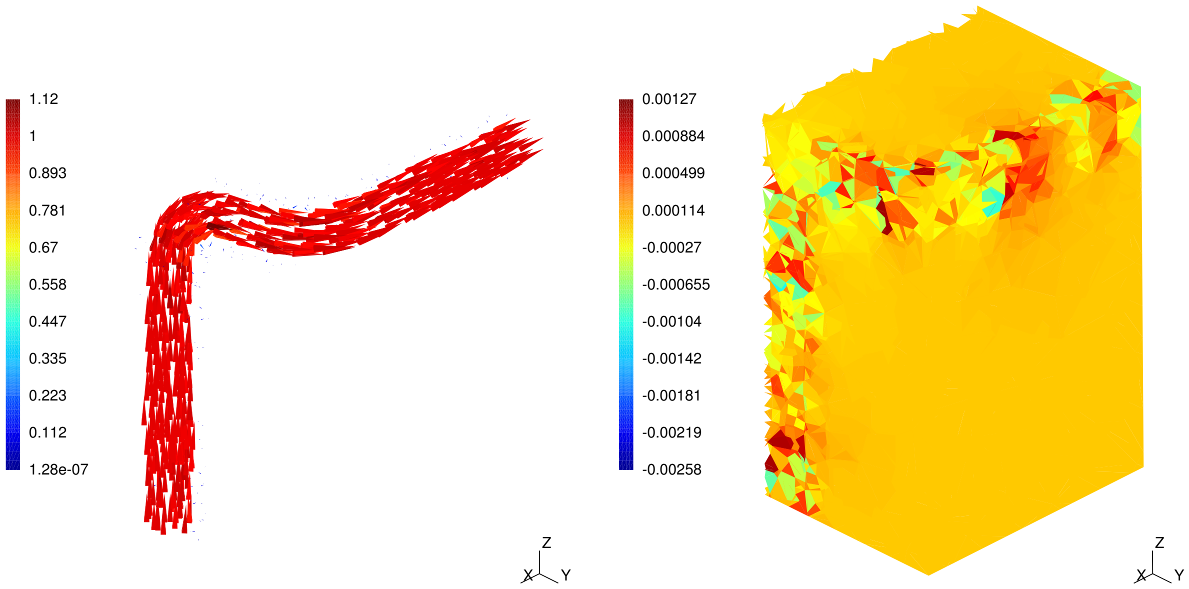

(a) $\mathbf{J}_h$, obtained using (95)

(b) div $\mathbf{J}_h$, obtained using (95)

Figure 26: Discretized current densities and their divergence, obtained using full-norm projection methods (twisted conductor).

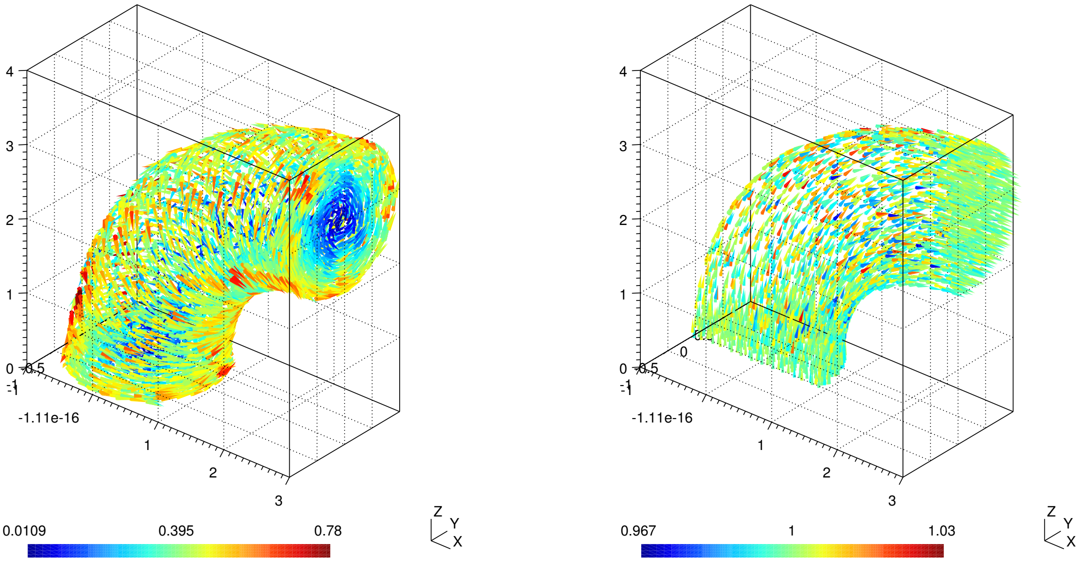

(a) $\mathbf{K}_h$

(b) $\mathbf{J}_h = \mathbf{curl}\ \mathbf{K}_h$

Figure 27: $\mathbf{K}_h$ field and discretized current densities, obtained using the $\mathbf{H}(\mathbf{curl}, \mathscr{D})$ semi-norm projection (98) (bent conductor).

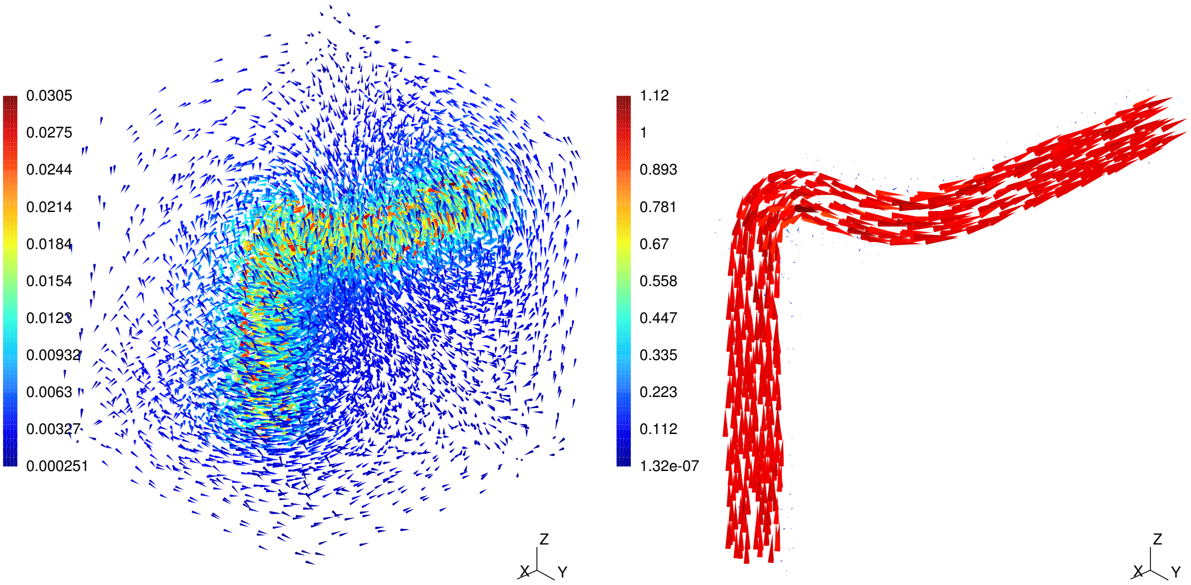

(a) $\mathbf{K}_h$

(b) $\mathbf{J}_h = \mathbf{curl}\ \mathbf{K}_h$

Figure 28: $\mathbf{K}_h$ field and discretized current densities, obtained using the $\mathbf{H}(\mathbf{curl}, \mathscr{D})$ semi-norm projection (98) (twisted conductor + air box).

3.1.3 *Conclusion*

Field projection methods are applied to the discretization of uniform analytical current densities. Both the $\mathbf{L}^2(\mathscr{D})$ projection and the $\mathbf{H}(\mathrm{div}, \mathscr{D})$ projection are capable of discretising the analytical current density at facet elements but the divergence is much smaller in the latter case. In order to ensure the zero divergence, $\mathbf{H}(\mathbf{curl}, \mathscr{D})$ semi-norm projections can be used.

3.2 CYLINDRICAL CONDUCTOR CARRYING UNIFORM CURRENTS

The second application considered is the magneto-mechanical modeling of a cylindrical conductor carrying uniform currents. For this example, we can deduce an analytical solution for the magneto-mechanical interaction thanks to the simple geometry [5]. In this case, we can validate our numerical solution of computational models, by the calculation of electromagnetic and mechanical models on common meshes and a comparison with the analytical solution. Subsequently, we will apply the mesh-to-mesh projection tools.

Let us consider an infinite cylinder, of which the magnetic permeability is μ_0. The cylinder is crossed by a uniform current density. Such current density creates magnetic forces and elastic deformations in the cylinder. Under the assumption of small deformations, Ohm's law is independent from mechanical stresses. In the elastic problem the stress-strain relations are decoupled from the magnetic fields. The exact solutions for the magnetic and elastic problem can be obtained by analytical calculations [5].

Using Ampere's law, the distribution of the magnetic flux density is perfectly known as a circumferential and linear function across the conductor. It can be written as:

$$B_\theta(r) = \begin{cases} \dfrac{\mu_0 J_0 r}{2}, & r < R \\ \dfrac{\mu_0 J_0 R^2}{2r}, & r \geqslant R \end{cases} \tag{100}$$

with J_0 the uniform current density and R the radius of the cylinder.

In the elastic problem, we take Lorentz forces (i. e. $\mathbf{J} \times \mathbf{B}$) as the source terms. After satisfying boundary conditions, i. e. no deformation at the center and no traction at $r = R$, the stresses in the cylinder are expressed as follows:

$$\begin{cases} \sigma_{rr}(r) = -\dfrac{\mu J_0^2 R^2}{16}\dfrac{(3-2\nu)}{(1-\nu)}(1-\dfrac{r^2}{R^2}) \\ \sigma_{\theta\theta}(r) = -\dfrac{\mu J_0^2 R^2}{16}\dfrac{(3-2\nu)}{(1-\nu)}(1-\dfrac{(1+2\nu)}{(3-2\nu)}\dfrac{r^2}{R^2}) \\ \sigma_{r\theta}(r) = 0 \end{cases} \tag{101}$$

We refer to [71, 72] for further magneto-thermo-electrostatic analytical study.

For a cylinder of 1mm radius and traversed by a current of 10A, with ν=0.3 we obtain at the center of the cylinder: $\sigma_{rr} = \sigma_{\theta\theta} =$ -2.73$\mathrm{N/m^2}$.

In the computations which follow, two meshes are used: M1 (624k elements) and M2 (152k elements) - see Figure 29.

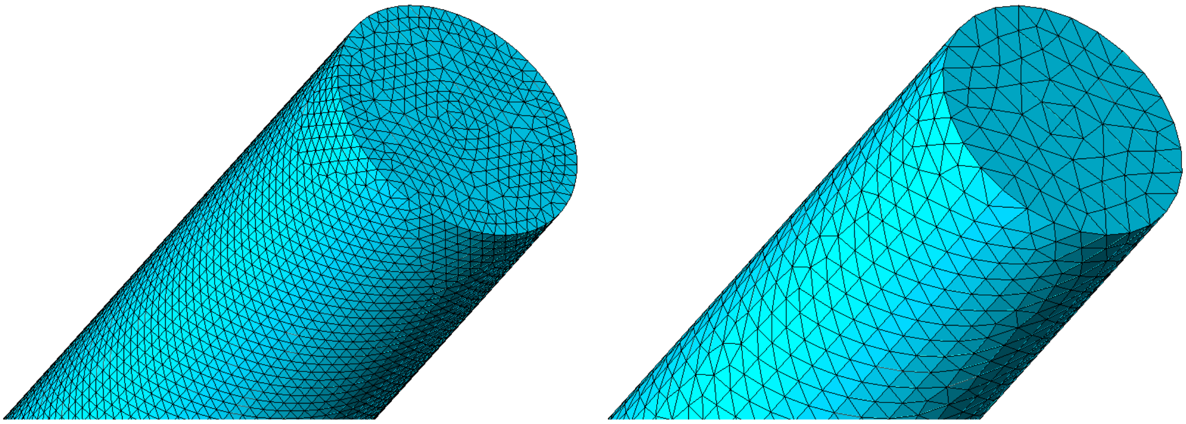

(a) M1

(b) M2

Figure 29: Meshes of the cylinder used here.

3.2.1 *Magneto-mechanical calculation on common meshes*

First, we solve the magnetic and mechanical models on common meshes. Thus no projection is used.

Using the vector potential **A**-formulation (11), the distribution of the magnetic flux density can be calculated. Figure 30 illustrates the obtained magnetic flux density on a clipping plane of the studied domain.

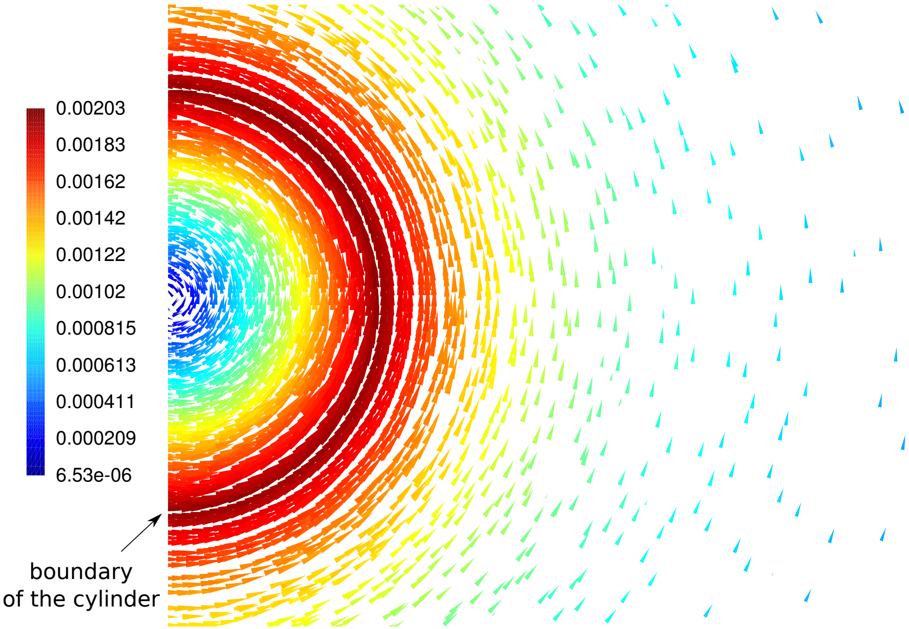

Figure 30: Distribution of the magnetic flux density (T), plotted on a clipping plane.

Magnetic forces are the source terms for the elastic problem. In the literature different methods are proposed regarding their calculation [73, 74, 75, 76, 77] Here we have used the virtual work principle to calculate nodal forces [57]. The elastic problem can then be solved with the static displacement formulation (27). We present, in Figure 31, the obtained stresses on mesh M1.

Table 17 compares, on the two meshes, the obtained radial stress σ_{rr} at the center of the cylinder to the analytical solution. Here by the numerical calculation on common meshes, the final result for the magneto-mechanical problem is close to the analytical solution. The relative errors is 3.3% on mesh M2 and 0.7% on the finer mesh M1. Thus in what follows we consider that the solution of our magnetic and elastic models, as well as the calculation of magnetic forces, are validated.

Table 17: Comparison with the analytical solution. Here the magnetic and elastic problems are solved on the common mesh.

mesh	σ_{rr} at r=0	relative error
M1	-2.71 N/m^2	0.7%
M2	-2.64 N/m^2	3.3%

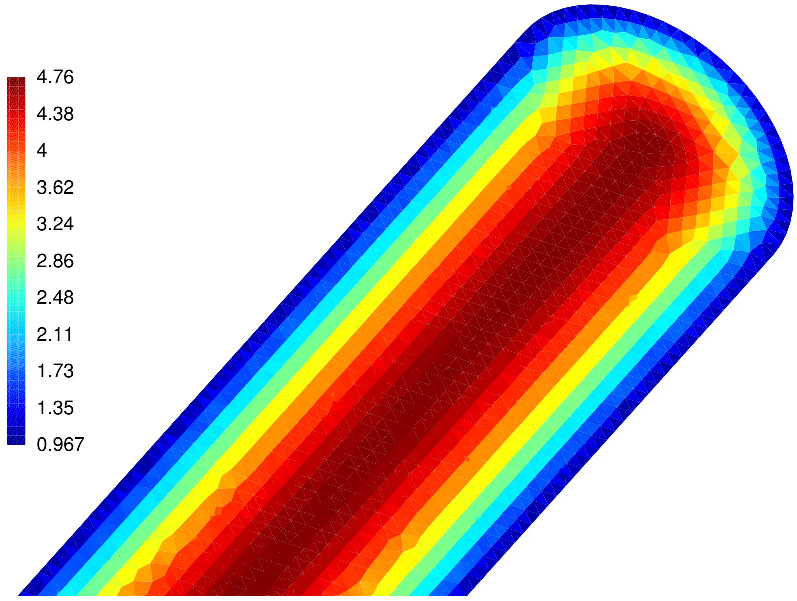

Figure 31: Obtained Von Mises stress (N/m^2) in the cylinder.

Table 18: Comparison with the analytical solution. Here both meshes are used and the M1-to-M2 projection of **B** field is carried out.

mesh	σ_{rr} at r=0	Relative error
M1-to-M2 with proj.	-2.66 N/m^2	2.2%

3.2.2 *Magneto-mechanical calculation with M1-to-M2 projection*

Secondly, using the projection techniques, we can now solve the problem with two meshes: M1 for the magnetic problem and M2 for the elastic problem.

Remark 7 *In terms of the communication between the two models, various strategies can be investigated e. g. the projection of the magnetic potential, the magnetic field or the forces directly. As indicated in Remark 6, in this work we focus on the mesh-to-mesh transfer of electro-magnetic quantities.*

Here in our case, the magnetic flux density **B** is projected from M1 to M2. The magnetic forces are calculated on M2 by applying the virtual work principle on the projected **B** field. The elastic problem is then solved on the submesh of M2 which consists of the cylinder. Regarding the implementation technique for the projection, here the intersection of M1 and M2 is undertaken.

In Table 18 regarding the stress at the center, the calculation with the M1-to-M2 projection is very close to the analytical solution.

Compared with the magnetic and elastic computations both on M1 (line 2 in Table 17), here the solution strategy with projection is indeed less accurate. This is because M1 is finer than M2. In the M1-to-M2 field projection, accuracy losses should not be ignored between the source and target meshes. Similar phenomena can be remarked in Chapter 2.

The advantage of using the M1-to-M2 projection strategy, is shown by the greater precision in comparison with the solution on M2 alone (line 3 in Table 17). As a matter of fact, using both these two strategies the elastic problem is solved on M2. The M1-to-M2 projection is advantaged because the magnetic problem is solved on M1, which is finer.

3.2.3 *Conclusion*

In this section we have treated a simple magneto-elastic example. The obtained results from finite element analysis are compared with analytical solutions. Subsequently we have compared the mesh-to-mesh field projection approach with the strategy of solving magnetic and mechanical problems on common mesh.

In practice, solving several models on common meshes implies an important computational cost. The projection approaches can transfer magnetic fields from one mesh to another, allow us to solve different models on different meshes. Moreover, in the studied example the projection used provides great accuracy regarding the final result for the entire magneto-mechanical problem.

3.3 TWO FACE-TO-FACE IRON CORES

In Section 2.3.3, we considered an example of two face-to-face iron cores (Figure 14). For this example, two cases were studied: a magneto-static problem and a magneto-harmonic problem. For each case we solved the electromagnetic model and projected the results onto a second mesh using energetic formulations. Now we can continue and calculate downstream mechanical deformations and thermal temperature rises.

3.3.1 *From the magneto-static problem to mechanical deformations*

When the excitation currents are stable, the two iron cores are attracted by static magnetic forces.

The magneto-static problem has been solved on mesh M1 using the scalar potential Ω-formulation. The obtained magnetic field $\mathbf{H}_s$ is then projected onto mesh M2 using the energetic approach. With the virtual work principle, the magnetic forces have then been calculated (e. g. the forces on iron core 2 previously calculated are reminded in Figure 32).

Using these forces as the source terms in the mechanical model, we can calculate the corresponding elastic deformations (Figure 33) and stresses (Figure 34). Here the von Mises stress is a scalar stress value computed from the 3×3 stress tensor, in order to state the distortion energy. In terms of boundary conditions, here we have embedded the right-hand face of iron core 2.

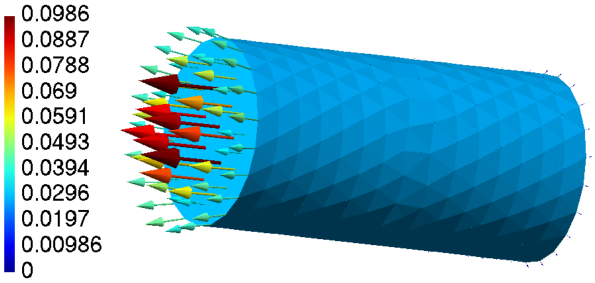
0.0986
0.0887
0.0788
0.069
0.0591
0.0493
0.0394
0.0296
0.0197
0.00986
0

Figure 32: Magnetic forces (N) on iron core 2. They are calculated by applying the virtual work method on the projected $\mathbf{H}_t$ field using the energetic formulation.

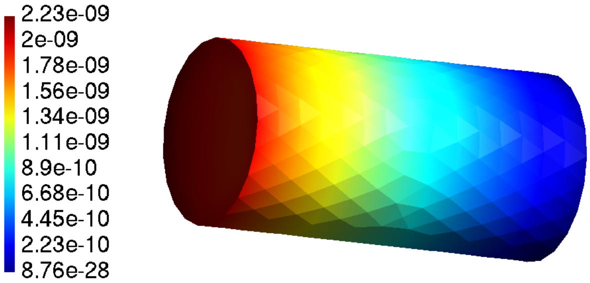
2.23e-09
2e-09
1.78e-09
1.56e-09
1.34e-09
1.11e-09
8.9e-10
6.68e-10
4.45e-10
2.23e-10
8.76e-28

Figure 33: Displacement field (m) in iron core 2. Here the left-hand face is attracted by magnetic forces.

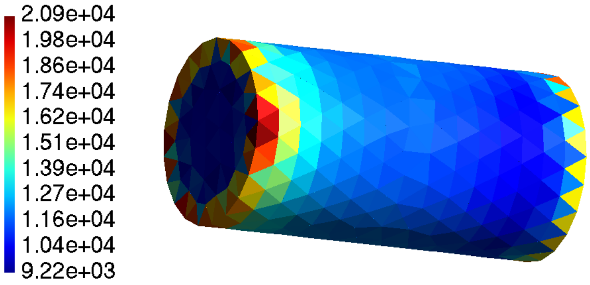
2.09e+04
1.98e+04
1.86e+04
1.74e+04
1.62e+04
1.51e+04
1.39e+04
1.27e+04
1.16e+04
1.04e+04
9.22e+03

Figure 34: Von Mises stresses (N/m^2) in iron core 2.

3.3.2 *From the magneto-harmonic problem to temperature rises*

Subsequently, an alternating current were applied in the excitation coil.

The magneto-harmonic problem was solved on mesh M1 using the **T**-Ω formulation. The energetic projection transfered the magnetic field onto mesh M2 with respect to the magnetic energy. Moreover, the joule heating was well conserved between the two meshes (Figure 35).

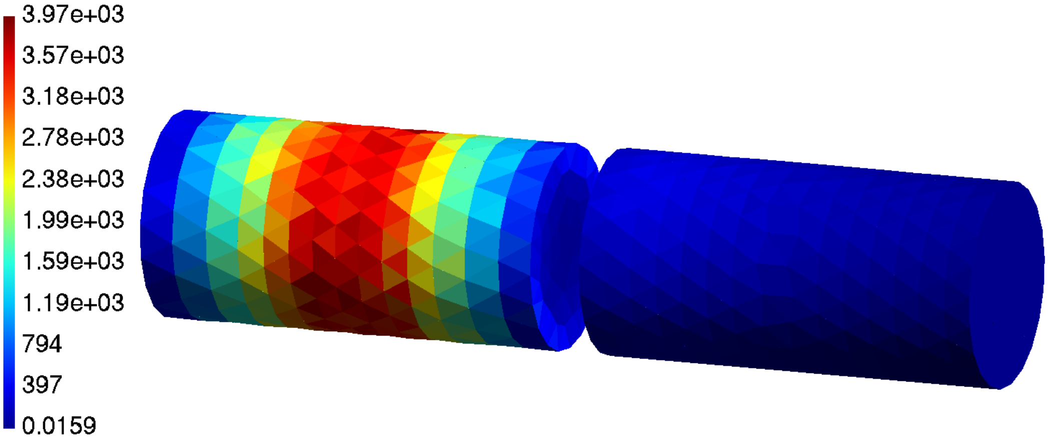

Figure 35: Ohmic losses densities (w/m^3) in the two iron cores. They are calculated from the "energetically" projected $\mathbf{H}_t$ field.

The thus obtained joule heating can then be used as source terms in the thermal model. After imposing a uniform initial temperature of 20°C and fixing the temperature at the air box boundaries, the temperature evolution can be solved using the temperature formulation (31). The maximum temperature can be traced as a function of time (Figure 36).

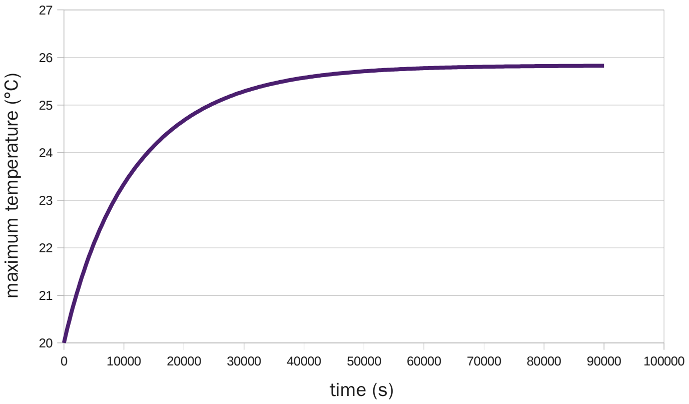

Figure 36: Evolution of the maximum temperature (°C) versus time (s).

From the initial state to the static state, the evolution of the distribution of the temperature is shown in Figure 37. Here the temperature field is plotted on the clipping plane S of Figure 14. The cylindrical iron cores are presented by rectangles in this case.

Due to the great thermal conductivity, the distribution of the temperature inside both iron cores are almost uniform. Iron core 1 is heated faster because of the greater eddy currents

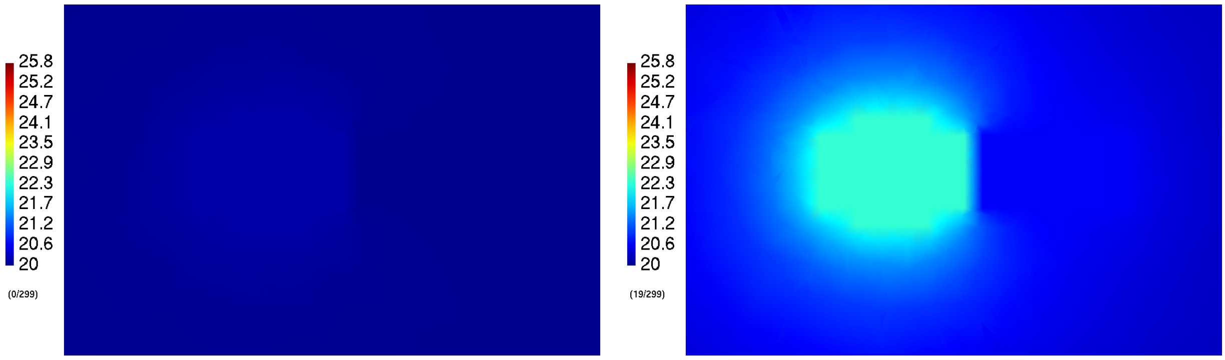

(a) 5min (b) 100min

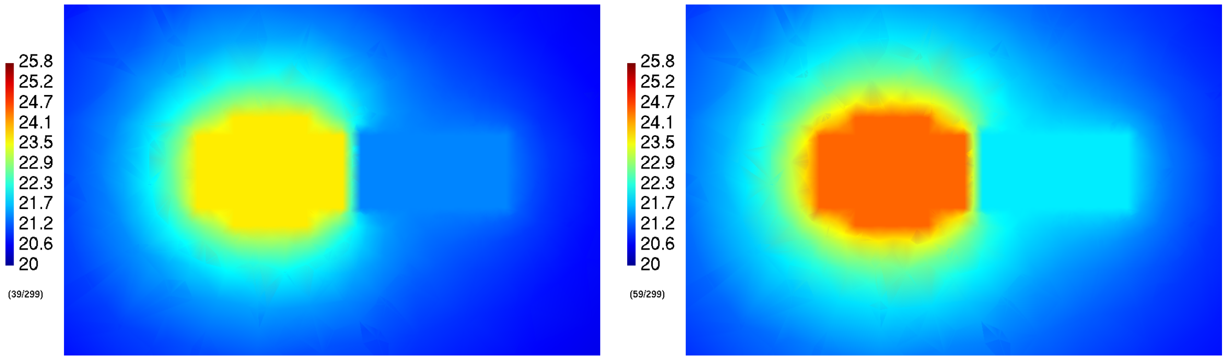

(c) 200min (d) 300min

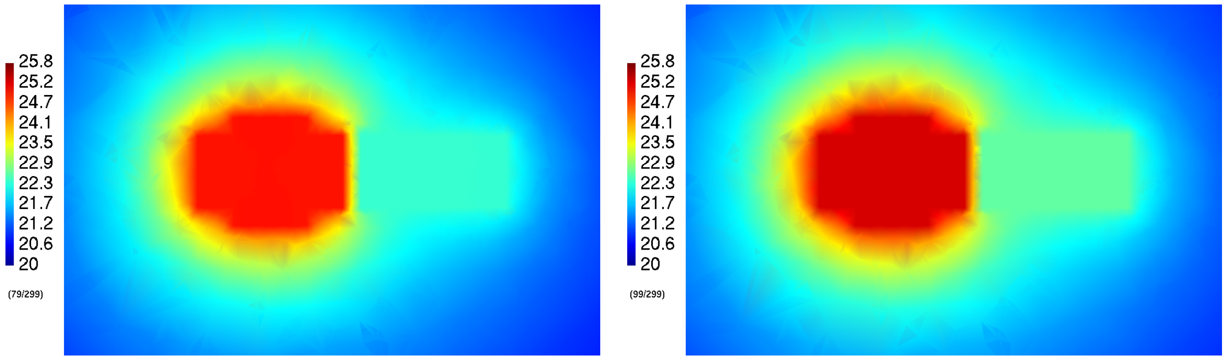

(e) 400min (f) 500min

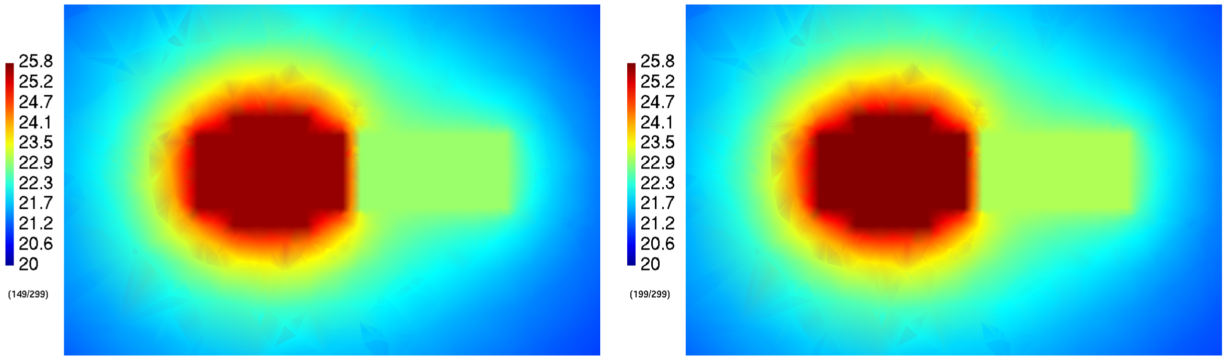

(g) 750min (h) 1000min

Figure 37: Evolution of the distribution of the temperature field T (°C), plotted on a clipping plane of mesh M2.

and the copper losses insider the coil. In the absence of convection, air is a good insulator between the two iron cores.

3.3.3 *Conclusion*

Following the example of energetic projections presented in Section 2.3.3, here we have used the projected fields as inputs for mechanical and thermal models. In the static problem the projected magnetic field has been used for the calculation of magnetic forces and the corresponding elastic deformations. For the harmonic case the joule heating has allowed us to simulate the temperature variations.

3.4 ELECTROMAGNET FACING AN ELASTIC PLATE

In Chapter 2, we presented different techniques for field projections - e. g. the space of projection can be $\mathscr{L}^2(\mathscr{D})$ or $\mathscr{H}^1(\mathscr{D})$ depending on the objectives to be satisfied. In the case of $\mathscr{L}^2(\mathscr{D})$-projections, we can use either the Ritz-Galerkin method or specific bi-orthogonal test functions. Moreover, in terms of the mesh-to-mesh implementation, either the intersection of meshes or the approximate integration on the target mesh can be used. Now we setup a magneto-mechanical example, with which the influence of these techniques can be studied.

The example given concerns the calculation of the magnetic force acting on the embedded plate of an electromagnet and the elastic deformations [53, 56]. The geometry of the electromagnet is shown in Figure 38. The yoke we used has an axial symmetry. A total current of 100 Ampere turns is applied to the excitation coil. The initial air gap between the yoke and the plate is fixed at 1mm.

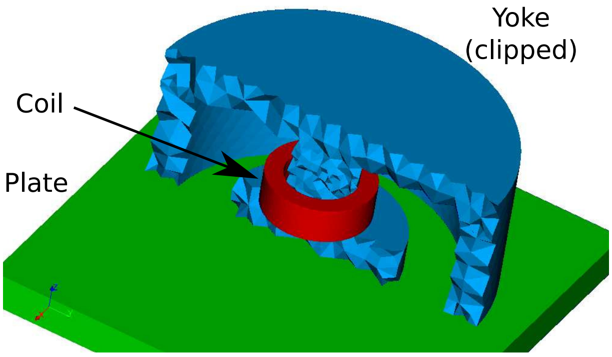

Figure 38: Geometry of the considered electromagnet.

Let us consider two different meshes: m_1 (384k tetrahedrons) and m_2 (133k tetrahedrons), the first being for the magnetic computation and the second for the elastic problem. Here we focus on the strategy involving the projection of $\mathbf{B}$ (Figure 39). In order to conserve the energy (Section 2.3), the projections are weighted with $1/\mu$.

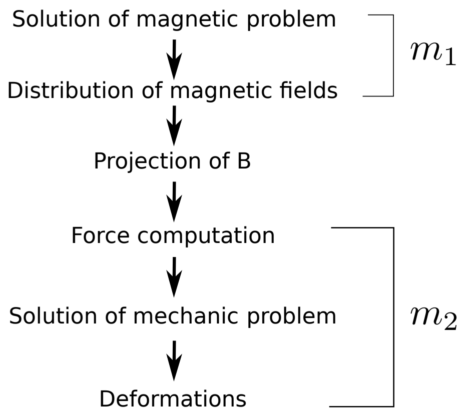
Solution of magnetic problem
Distribution of magnetic fields
Projection of B
Force computation
Solution of mechanic problem
Deformations
m_1
m_2

Figure 39: Computation strategy using the projection of **B**.

The magneto-static problem is solved using the vector potential **A** formulation (11). The elastic-static problem is solved using the displacement **u** formulation (27). The coupling terms between the magnetic model and the elastic model are, as in the previous examples, the magnetic forces. They are calculated on the plate using the virtual work principle from the magnetic fields. In the elastic problem, assuming boundary conditions such that the sides are clamped, these forces are then used as source terms for the calculation of the deformations.

For instance, the forces acting on the plate and the deformations calculated from the projected **B** are illustrated in Figure 40.

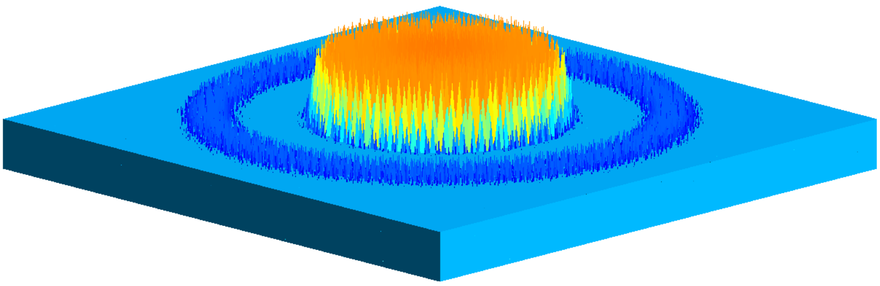

(a) magnetic forces

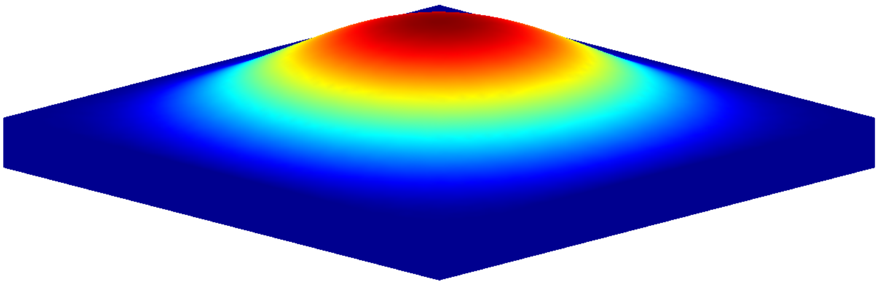

(b) elastic deformations

Figure 40: Magnetic forces on the plate and the induced deformations.

3.4.1 *Comparison of projection techniques*

First, we compare the different projection techniques. As the magnetic flux density is involved, we can carry out the projections in either $\mathbf{L}^2(\mathscr{D})$ or $\mathbf{H}(\mathrm{div},\mathscr{D})$. For the $\mathbf{L}^2(\mathscr{D})$-projection, we can use both the classic Ritz-Galerkin method and the Petrov-Galerkin method with bi-orthogonal test functions. In terms of implementation, here the intersection of the two meshes is calculated.

Table 19 compares the different projection approaches of $\mathbf{B}$ in such a magneto-elastic problem, In terms of the magnetic energy and the elastic deformations. The results obtained by magneto-elastic computation on common mesh are also given for reference purposes.

Since m_1 is finer than m_2, the result obtained on m_1 by the direct calculation (line 2 in Table 19) is considered as the most accurate solution. In comparison to $\mathbf{L}^2(\mathscr{D})$-projections, the $\mathbf{H}(\mathrm{div},\mathscr{D})$-projection allows greater conservation of the divergence during the projection and thus better precision when calculating the magnetic energy.

On the other hand, the projected field $\mathbf{B}$, using all three methods, allows a precision level which is equal in each case for the computation of the deformation. In fact, the deformation is calculated from the magnetic forces and the forces are actually the derivative of the magnetic energy with respect to virtual displacements. The $\mathbf{H}(\mathrm{div},\mathscr{D})$-projection allows better conservation for the divergence of $\mathbf{B}$ and thus better precision with respect to the magnetic energy. But this advantage is no longer valid for the deformations. Thus if we are interested in the deformations, a $\mathbf{L}^2(\mathscr{D})$-projection is able to provide adequate accuracy. In this case the use of the Petrov-Galerkin method with bi-orthogonal test functions is more interesting than the classical Ritz-Galerkin method, because the computation cost is lower.

3.4.2 *Comparison of implementation techniques*

Second, Table 20 compares the different implementation techniques (Section 2.2). For this, we restrict ourselves to the case of $\mathbf{L}^2(\mathscr{D})$-projections using the Ritz-Galerkin method. The projection system is calculated either with the intersection of m_1 and m_2, or approximately on m_2. For the later technique, we can also employ different quadrature rules.

In terms of magnetic energy, since m_1 is finer than m_2, the result on m_1 by the direct calculation (line 2 in Table 20) is considered as the most accurate solution. In comparison to the projection using approximate integration, the intersection of meshes allows greater conservation of the distribution of the magnetic flux density and thus better precision when calculating the magnetic energy. However, as we have seen in the analytical example (Section 2.2.2), for the integration over the target mesh, more quadrature points can indeed improve the sampling of the given field, and thus improve the accuracy of the obtained magnetic energy.

On the other hand, in comparison to direct calculation results, the projected $\mathbf{B}$ allows a precision level which is equal for the computation of the deformation. As a matter of fact, at the center of the plate, the displacements obtained using both implementation techniques

Table 19: Comparison of the different strategies. (Concerning "$\mathfrak{m}_\#$ without projection", the magnetic problem is solved on $\mathfrak{m}_\#$ and the elastic problem is solved on the submesh of $\mathfrak{m}_\#$ which constitutes the plate.)

Computation strategy		Magnetic energy (mJ)	Deformation at center (nm)
$\mathfrak{m}_1$ without projection		17.2	12.7
$\mathfrak{m}_2$ without projection		16.8	11.6
$\mathfrak{m}_1 \to \mathfrak{m}_2$ projection of $\mathbf{B}$	$\mathbf{L}^2(\mathscr{D})$ Ritz-Galerkin	17.4	11.6
	$\mathbf{L}^2(\mathscr{D})$ Petrov-Galerkin (ψ_B)	17.6	11.7
	$\mathbf{H}(\mathrm{div}, \mathscr{D})$ Ritz-Galerkin	17.1	11.4

Table 20: Comparison of implementation techniques in the magneto-mechanical example. The Galerkin projection is applied to the magnetic flux density **B**. Concerning "$\mathfrak{m}_\#$ without projection" ($\# = 1, 2$), the magnetic problem is solved on $\mathfrak{m}_\#$ and the elastic problem is solved on the submesh of $\mathfrak{m}_\#$ which constitutes the plate.

		Magnetic energy (mJ)	Displacement (nm)	computation time (s)
$\mathfrak{m}_1$ without projection		17.2	12.7	
$\mathfrak{m}_2$ without projection		16.8	11.6	
$\mathfrak{m}_1 \to \mathfrak{m}_2$ projection of **B**	intersection	17.4	11.6	2861
	4 Gaussian points	16.6	11.6	144
	16 Gaussian points	16.7	11.6	345
	29 Gaussian points	17.0	11.6	775

and high-order quadrature rules are practically the same. The greater precision for the mesh-to-mesh projection of the magnetic flux density, can barely ensure greater accuracy in order to solve the deformation in the mechanical problem. In this case, the integration over target elements shows a significant advantage regarding the computation time.

3.4.3 *Conclusion*

In this section we have studied the performance of different projection techniques through a magneto-elastic example.

Previously in the analytical example (Section 2.1.6), the $\mathbf{H}(\mathrm{div}, \mathscr{D})$-projection gives greater accuracy than the $\mathbf{L}^2(\mathscr{D})$-projection. This advantage is weaker here in our magneto-elastic application. For the entire magneto-mechanical example with $\mathbf{L}^2(\mathscr{D})$-projections, the Petrov-Galerkin method with bi-orthogonal test functions allows the same level of accuracy as the Ritz-Galerkin method, and reduces the computation cost.

Regarding the implementation techniques, mesh-intersecting is still the best way to ensure the accuracy of the field projection in our application but is computationally expensive. The implementation technique of integration over target elements is less accurate but reduces the computation cost. One compromise solution can be several projections with the later technique but with different quadrature rules. The solution can be trusted if the different quadrature rules have little influence on the final result. Moreover, the sum of the computation time is still preferable in comparison to mesh-intersecting, while also presenting the advantage of being simple to implement.

3.5 DOUBLE-EXCITATION SYNCHRONOUS ALTERNATOR

With all the tools previously presented, we can now study the magneto-mechanical phenomena inside an electrical machine. The machine given concerns an alternator model under development at Valeo.

One important issue to be solved for the design of this model, is the generalization of acoustic noises. Silence is nowadays a crucial element for the marketing of automotive alternators. Thus several studies have been carried out in parallel for this alternator. At high speed ranges, most noises have been identified as being of mechanical and aerodynamic origins. Nevertheless, for a velocity smaller than 6000tr/min, the magneto-mechanical interaction is the major the major source for the vibrations.

3.5.1 *Magneto-mechanical calculations*

In order to calculate the mechanical vibrations issued from magnetic forces in this electrical machine, the magnetic model and the mechanical model are coupled. For simplicity, here we use linear media in the magnetic model. In the mechanical model, only the stator is considered. The meshes used are presented in Figure 41.

In the following, we consider that this alternator runs off-load at 1000tr/min. The remanence for each permanent magnet is equal to 1.15T. The rotor is double excited, i. e. a current of 5A is also applied to its coil.

For the accuracy of the magnetic computation, the air gap has been finely meshed in Figure 41(a). Due to the symmetry of the magnetic study, only one layer of mesh is necessary. On the contrary, in the mechanical computation, as only the stator is considered, the mesh of the rotor and air gap is no longer necessary (Figure 41(b)). Multiple layers are however required for the computation of deformations.

Remark 8 *Here for the mechanical mesh the stator teeth are covered by at least one layer of air elements. These air elements are not used in the mechanical computation. They are however useful for the force calculation with virtual work principle.*

In order to calculate the nodal forces, the virtual work principle consists of calculating the energy derivatives in all neighboring elements (i. e. the patch of the node of interest). For this reason the air elements surrounding the stator also contribute to the acting magnetic forces.

The computation strategy for the entire magneto-mechanical problem can be summarised as Figure 42.

It can be recalled that in our case `code_Carmel` and `code_Aster` are the software packages for the magnetic and mechanical calculations respectively.

To take into account the movement of the rotor with the fixed-step technique, the magnetic mesh of the air gap is uniform. n=1656 steps is used in the magnetic computation. For each step, a magnetic quasi-static problem is solved using the Ω-formulation (14) - e. g. , the obtained magnetic flux density $\mathbf{B}$ at the first step is illustrated in Figure 43.

The obtained magnetic field $\mathbf{H}$ for each step is then projected to the mechanical mesh (edge elements). In order to take into account the computation time, the $\mathbf{L}^2(\mathscr{D})$-projection and the bi-orthogonal test functions have been used (Section 2.1). For the same reason the projection systems are calculated on the mechanical mesh using the sampling-integration technique (Section 2.2). Moreover, the energetic formulations have been used for the conservation of magnetic energy and the accuracy of magnetic forces (Section 2.3).

Once the magnetic field $\mathbf{H}$ is projected onto the mechanical mesh, the magnetic forces can be obtained by applying the virtual work principle. Figure 44 shows the distribution of the forces for the first time step.

These forces obtained at different time steps can then be transformed into frequency domain. For instance, we can focus one node at the middle of a tooth, such as node 4899 in Figure 44. Figure 45 plots its nodal force as a function of time and the corresponding frequency spectrum.

After the fast Fourier transform, the obtained sample frequencies ranges from 0Hz to 13.78kHz with an interval of 16.67Hz. These forces are source terms for the mechanical model. Assuming that the stator is embedded by two faces, the vibrations can be calculated using the

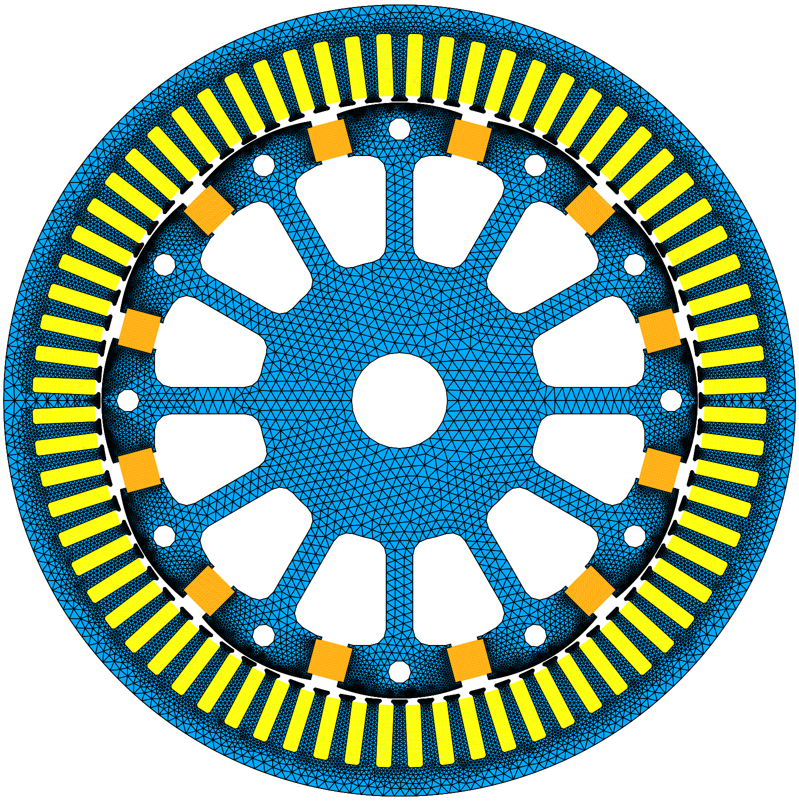

(a) magnetic mesh: 71k prisms × 1 layer

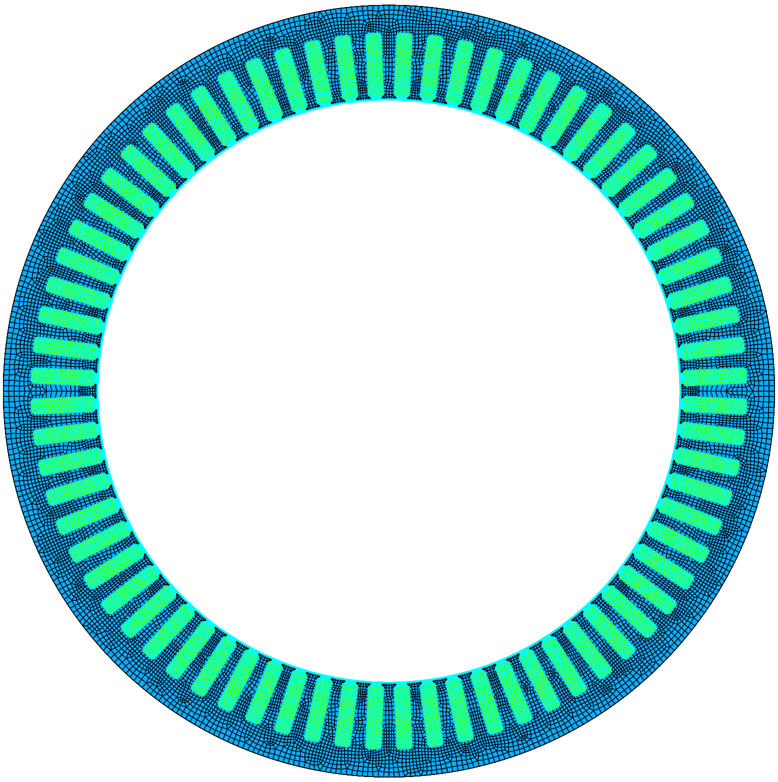

(b) mechanical mesh: 12k hexahedrons × 4 layers

Figure 41: Meshes used in the magnetic and mechanical models.

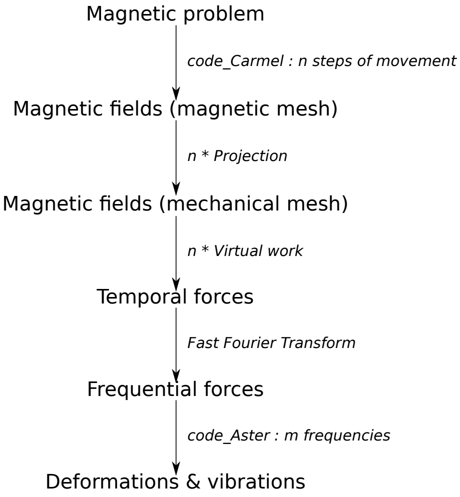
Magnetic problem
code_Carmel : n steps of movement
Magnetic fields (magnetic mesh)
n * Projection
Magnetic fields (mechanical mesh)
n * Virtual work
Temporal forces
Fast Fourier Transform
Frequential forces
code_Aster : m frequencies
Deformations & vibrations

Figure 42: Computation strategy for the electrical machine.

modal analysis. Figure 46 and Figure 47 illustrate the deformation and acceleration at node 4899. The distribution of the vibrations inside the electrical machine can also be obtained by harmonic calculations (Figure 48).

As the rotor rotates at 1000tr/min, the interval between two pole-facing positions for each stator tooth is 5ms. The fundamental frequency for the magnetic forces and the vibrations is thus 200Hz. Indeed, in comparison with Figure 47, in Figure 45 no magnetic force is visible at 9kHz. However, the acceleration is the second-derivative of the displacement and is proportional to the square of the frequency.

Last but no least, we can illustrate the computation time consumed in such magneto-mechanical analysis (Table 21).

Table 21: Computation time overview for the magneto-mechanical analysis (with a cpu of 2.4GHz single thread).

	electromagnetic model	model coupling	mechanical model
time (hour)	2.31	0.59	4.30
percentage	32.1%	8.1%	59.8%

In fact, in this application, for all the 1656 projections, the target mesh is always the same. We have thus calculated only once the local bi-orthogonal test functions and the projection system (requires 2 minutes). For the other time steps the projection time can be reduced to less than 2 seconds. In this case, the total time cost of the projections is equal to 8.1% in the entire magneto-mechanical analysis.

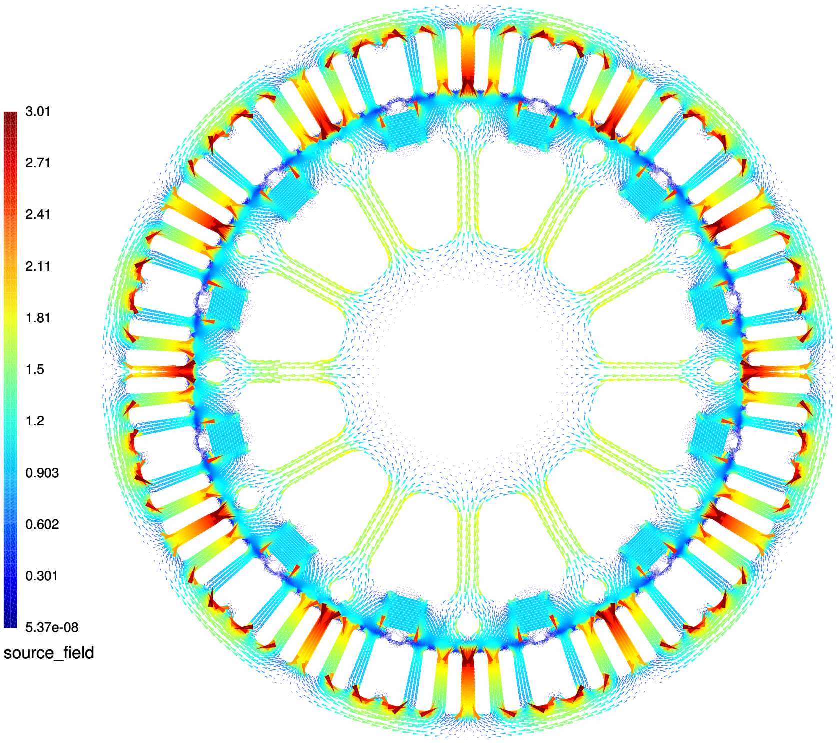

Figure 43: Obtained magnetic flux density (T) at the first time step (Collaboration with R. Fratila).

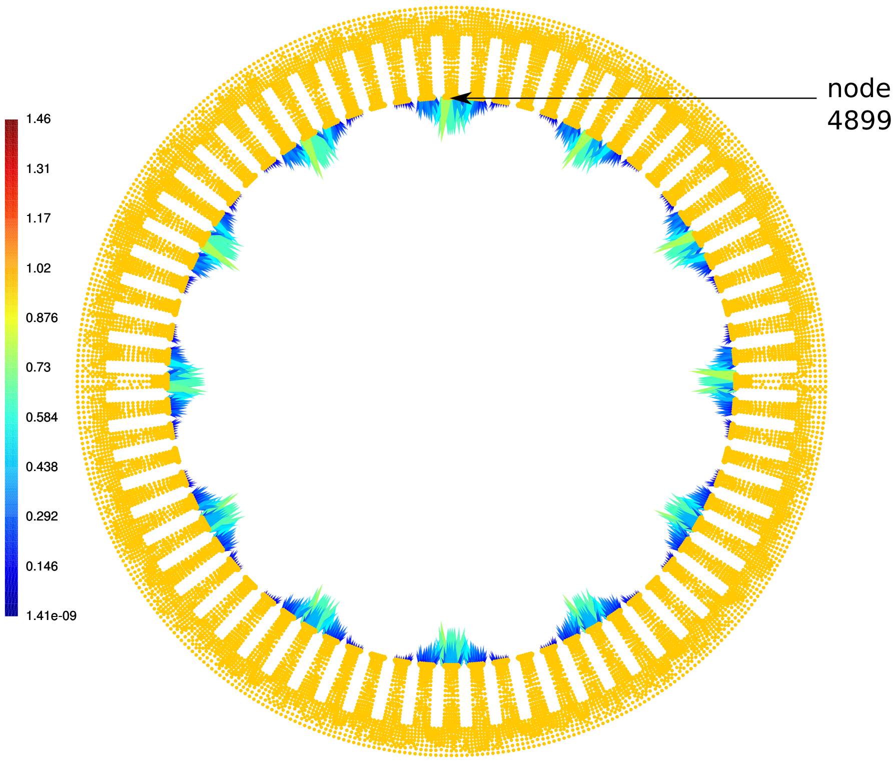

Figure 44: Obtained magnetic forces (N) on the stator (mechanical mesh), calculated from the projected **H** field at the first time step.

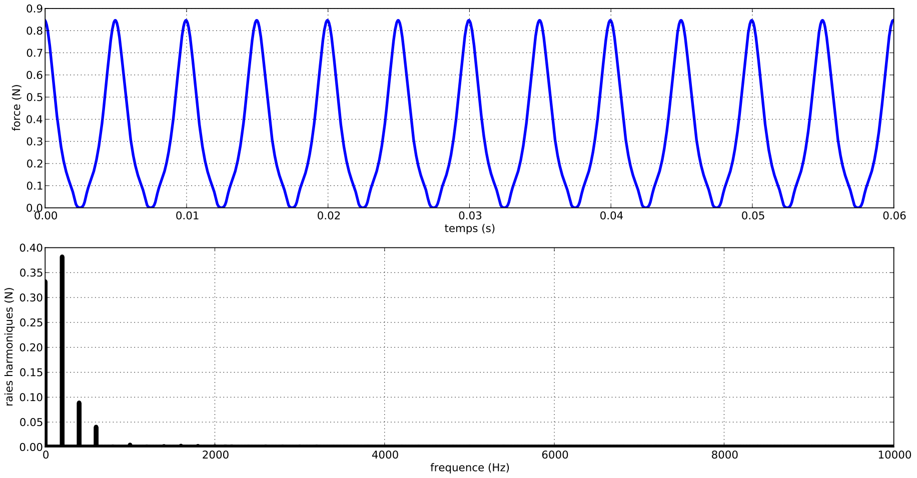

Figure 45: Module of the normal component of the force (N) on node 4899. Plotted as a function of time (above) and the corresponding frequency spectrum (below).

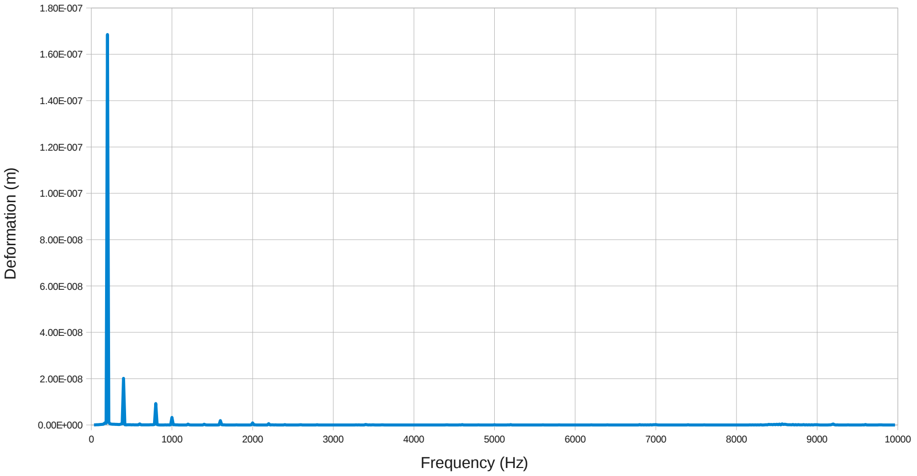

Figure 46: Module of the deformation (m) versus frequency (Hz) at node 4899 (collaboration with A. Tan-Kim).

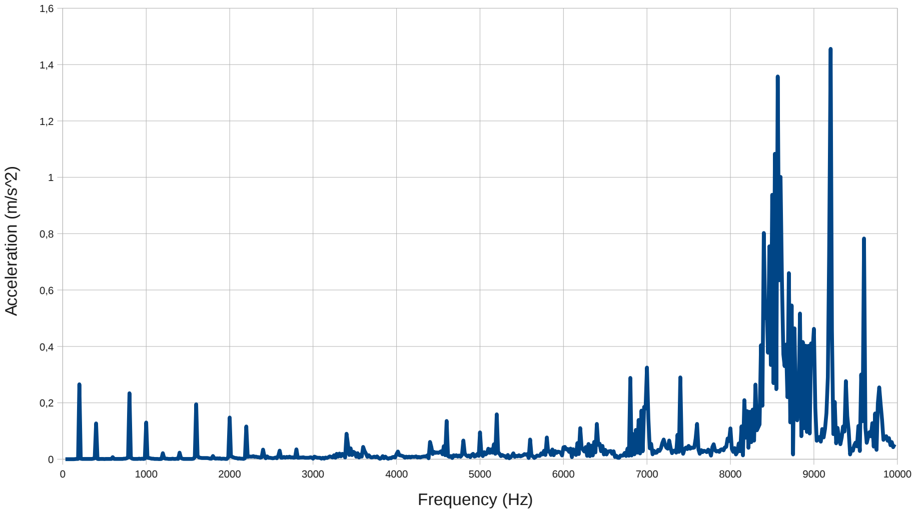

Figure 47: Module of the acceleration (m/s^2) versus frequency (Hz) at node 4899 (collaboration with A. Tan-Kim).

3.5.2 *Conclusion*

Magnetic forces are important origins of vibrations and acoustic noises in electrical machines. In this section we have simulated the magneto-mechanical phenomena inside a double-excitation synchronous machine. In particular, the magnetic and mechanical models are solved separately on their meshes.

The rotation of the rotor is taken into account using fixed time steps. The magnetic field for each time step is projected onto the mechanical mesh using the previously studied techniques. The projected magnetic field allows us to calculate the forces and the vibrations.

In terms of computation time, the presented projection approaches require times which are relatively small percentages within the entire magneto-mechanical analysis.

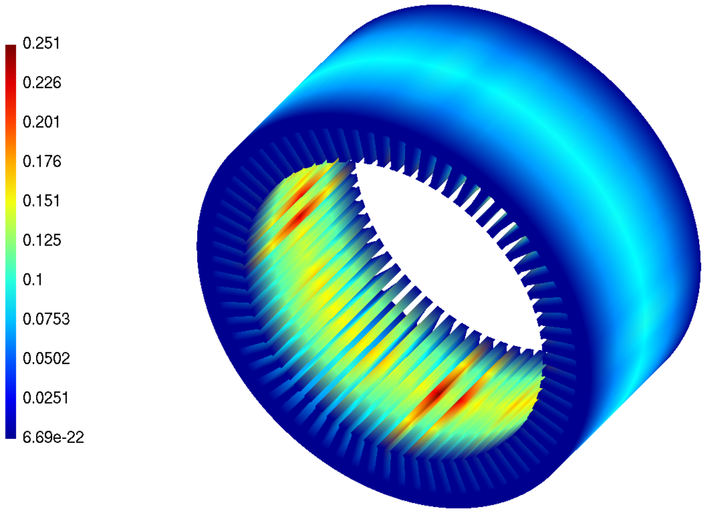
0.251
0.226
0.201
0.176
0.151
0.125
0.1
0.0753
0.0502
0.0251
6.69e-22

(a) 200Hz

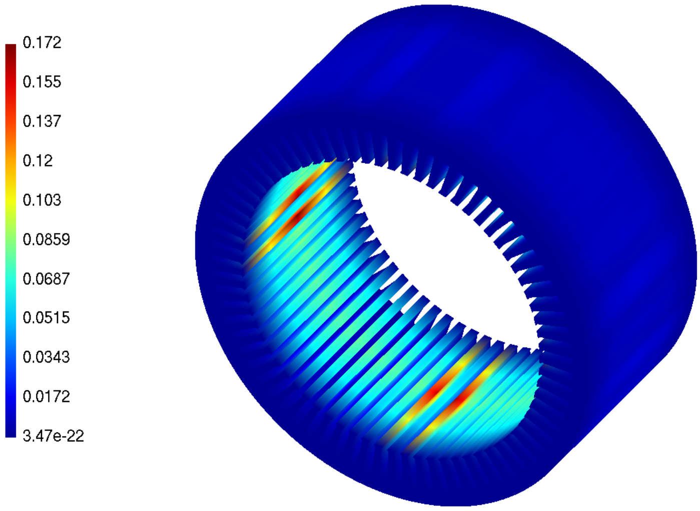
0.172
0.155
0.137
0.12
0.103
0.0859
0.0687
0.0515
0.0343
0.0172
3.47e-22

(b) 400Hz

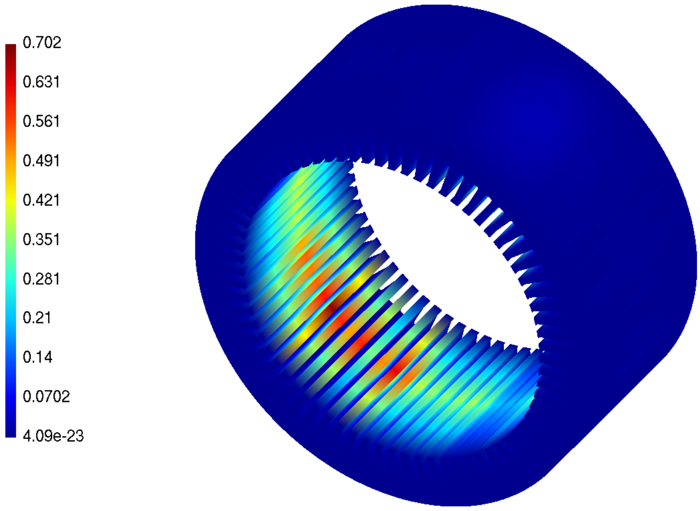
0.702
0.631
0.561
0.491
0.421
0.351
0.281
0.21
0.14
0.0702
4.09e-23

(c) 9kHz

Figure 48: Distribution of the module of the acceleration filed (m/s^2).

GENERAL CONCLUSIONS

The work presented in this thesis is focused on the model-coupling for finite element magneto-mechanical and magneto-thermal analysis.

Under the hypotheses of weak-coupling interactions, magneto-mechanical and magneto-thermal problems are divided into subproblems of which the physical nature differs. The subproblems are solved separately with electromagnetic, mechanical and thermal models (Chapter 1).

In the domain of finite element computation, the subproblems are very often solved with respect to their specific regions of interest and thus on different meshes. To obtain a precise computational result for the entire coupled problem, the information transmission and the communication between the subproblems are of crucial importance. In this thesis, we present field projection approaches for model coupling (Chapter 2).

To highlight some applications of field projections, numerical examples are studied through magneto-mechanical and magneto-thermal problems (Chapter 3).

The main conclusions and original contributions of this thesis are summarized hereafter, along with some future prospects.

CONCLUSIONS

Computation of weak-coupling magneto-mechanical and magneto-thermal problems requires field communication when the subproblems are discretized on multiple meshes. The field projection approaches based on the Galerkin method presented in this thesis provide useful tools for such cases.

- The classical Ritz-Galerkin projection is recalled in this thesis and extended to $\mathrm{H}(\mathbf{grad})$, $\mathbf{H}(\mathbf{curl})$ and $\mathbf{H}(\mathrm{div})$ in order to obtain greater projection accuracy for the distributional derivatives. Subsequently, local bi-orthogonal test functions are used to build a Petrov-Galerkin projection system with a diagonal matrix.

  Through the analytical examples, we have shown that the $\mathrm{H}(\mathbf{grad})$, $\mathbf{H}(\mathbf{curl})$ and $\mathbf{H}(\mathrm{div})$ projections give greater accuracy than L^2 or $\mathbf{L}^2$ projections regarding the obtained derivatives. In the case of L^2 or $\mathbf{L}^2$ projections, the Petrov-Galerkin method with bi-orthogonal test functions allows the same level of accuracy as the Ritz-Galerkin method, and reduces the computation cost.

- The accurate implementation of field projections requires the intersection of source and target meshes. Another solution is to directly integrate over target elements, by means of sampling the source field distribution at quadrature points. Projection with the latter technique is simpler but in general less accurate than mesh-intersecting.

Mesh-intersecting is still the only way to ensure the accuracy of the field projection but is computationally expensive. The sampling-integration algorithm over target elements is less accurate but reduces the computation cost. In our opinion the compromise solution should be several projections with the latter technique but with different quadrature rules. The solution can be trusted if the different quadrature rules have little influence on the final result. Moreover, the sum of the computation time is still preferable in comparison to mesh-intersecting, while also presenting the advantage of being simple to implement.

- In order to transfer electromagnetic fields between different meshes, energy-conserving projection methods are presented in this work. The definition of energetic norms are given for magneto-static problems as well as harmonic eddy current problems. Nonlinear cases are then investigated in order to take into account nonlinear magnetic characteristics.

  For magneto-mechanical and magneto-thermal modeling, the energetic formulations presented ensure the accuracy regarding energy distribution for the mesh-to-mesh transfer of electromagnetic fields.

CONTRIBUTIONS

Here is a list, with references to papers published in the frame of this thesis and section numbers in this manuscript, for the contributions we believe to be (at least partly) original:

+ Generalized summary of projection formulations in different spaces. Besides L^2 and $\mathbf{L}^2$, in this work projections are also carried out in $H(\mathbf{grad})$, $\mathbf{H}(\mathbf{curl})$ and $\mathbf{H}(div)$. These extensions of projection theory allow greater accuracy for derivatives. More details are presented in Section 2.1.2. This is published in [53] and connected to [9].

+ Local bi-orthogonal test functions for L^2 and $\mathbf{L}^2$ projections. Within the framework of the Petrov-Galerkin method, special test functions are constructed in order to simplify projections. Using this approach, the projection map is turned into a diagonal matrix. However, using the classical method, a linear system must be solved. We refer to Section 2.1.4 for further explanations. This has led to publication [53].

+ Comparison of two implementation techniques for mesh-to-mesh field projections. In practice the accurate implementation of the projection requires the intersection of source and target meshes and is computationally expensive. Another solution is to directly integrate over target elements, by means of sampling the source field distribution on quadrature points. In this work we have compared these solutions in terms of accuracy, speed and simplicity of realization. See Section 2.2. This is published in [56].

+ Energy-conserving projections for electromagnetic fields. The definition of energetic norms are given for magneto-static problems as well as harmonic eddy current problems. Nonlinear cases are then investigated in order to take into account nonlinear magnetic permeability. This is presented in Section 2.3 and has led to publications [58, 59].

FUTURE PROSPECTS

Several subjects for future research can be considered:

- The field projections presented can be enhanced in the time domain. In this work projections allow us to transfer fields between different meshes. Space-time projections would enable transferring between different time discretization bases.
- The space norm defined in this work can be modified into other forms. For instance, the norm of $\mathbf{H}(div)$ used in this thesis contains of the volume integration of the divergences. This could be replaced (improved) with a plane integration of the discontinuities of fields at the element boundaries.
- High-order bi-orthogonal functions can be sought in the spaces $\mathrm{H}(\mathbf{grad})$, $\mathbf{H}(\mathbf{curl})$ and $\mathbf{H}(div)$. Unlike the linear degree-one bi-orthogonal functions used in this thesis, high-order ones can take into account the continuity of derivatives at boundaries. This reduces the computation cost for high-precision $\mathrm{H}(\mathbf{grad})$, $\mathbf{H}(\mathbf{curl})$ and $\mathbf{H}(div)$ projections.

A

APPENDIX: BI-ORTHOGONAL FUNCTIONS

Bi-orthogonal functions are demonstrated in this appendix for nodes, edges and facets.

In particular, the nodal functions presented can be directly used for projections in a general way. For edges and facets, as the coordinate transformation is much more complex, the corresponding bi-orthogonal functions have to be determined on real meshes. Here we demonstrate the determination process of edge and facet functions, in the framework of the example previously presented in Section 2.1.4.

NODAL BI-ORTHOGONAL FUNCTIONS

Nodal bi-orthogonal functions are given in this part for a reference triangle and tetrahedron. In this thesis, they are used as test functions for $\mathscr{L}^2(\mathscr{D})$ projections with the Ritz-Galerkin method onto the node elements.

Triangles

Let $(0,0)$, $(1,0)$ and $(0,1)$ be the three nodes of the reference triangle. The nodal Whitney functions are:

$$\begin{cases} w_1^n = 1 - \xi - \eta \\ w_2^n = \xi \\ w_3^n = \eta \end{cases} \tag{102}$$

The corresponding bi-orthogonal functions are:

$$\begin{cases} \psi_{B1}^n = 18 - 24\xi - 24\eta \\ \psi_{B2}^n = 24\xi - 6 \\ \psi_{B3}^n = 24\eta - 6 \end{cases} \tag{103}$$

Tetrahedrons

For the reference tetrahedron, let $(0,0,0)$, $(1,0,0)$, $(0,1,0)$ and $(0,0,1)$ be the four nodes. The nodal Whitney functions are:

$$\begin{cases} w_1^n = 1 - \xi - \eta - \zeta \\ w_2^n = \xi \\ w_3^n = \eta \\ w_4^n = \zeta \end{cases} \tag{104}$$

The corresponding bi-orthogonal functions are:

$$\begin{cases} \psi_{B1}^n = 96 - 120\xi - 120\eta - 120\zeta \\ \psi_{B2}^n = 120\xi - 24 \\ \psi_{B3}^n = 120\eta - 24 \\ \psi_{B4}^n = 120\zeta - 24 \end{cases} \tag{105}$$

EDGE BI-ORTHOGONAL FUNCTIONS

In general, edge bi-orthogonal functions are determined on real meshes. Figure 49 recalls the 2D mesh previously used in Section 2.1.4.

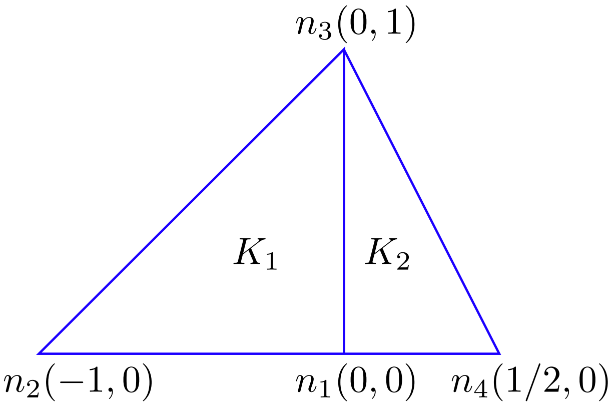

Figure 49: Mesh of two triangles. They share a common edge.

We determine the bi-orthogonal functions separately on both sides of the common edge.

Triangle on the left: K_1

For the triangle on the left side, the nodal functions are:

$$\begin{cases} w_1^n = 1 + x - y \\ w_2^n = -x \\ w_3^n = y \end{cases} \tag{106}$$

The edge functions can thus be constructed:

$$\begin{cases} \mathbf{w}_1^a = w_1^n \ \mathbf{grad} \ w_2^n - w_2^n \ \mathbf{grad} \ w_1^n = (y-1)\mathbf{e_x} - x\mathbf{e_y} \\ \mathbf{w}_2^a = w_1^n \ \mathbf{grad} \ w_3^n - w_3^n \ \mathbf{grad} \ w_1^n = -y\mathbf{e_x} + (x+1)\mathbf{e_y} \\ \mathbf{w}_3^a = w_2^n \ \mathbf{grad} \ w_3^n - w_3^n \ \mathbf{grad} \ w_2^n = y\mathbf{e_x} - x\mathbf{e_y} \end{cases} \tag{107}$$

Let us write the bi-orthogonal function associated with edge 2 (oriented from n_1 to n_3) as the linear combination of the edge functions:

$$\psi_{B2}^e = a \ \mathbf{w}_1^a + b \ \mathbf{w}_2^a + c \ \mathbf{w}_3^a \tag{108}$$

with a, b and c the coefficients to be determined.

By definition, ψ_{B2}^e satisfies:

$$\begin{cases} \int_{K_1} \psi_{B2}^e \cdot \mathbf{w}_1^a = 0 \\ \int_{K_1} \psi_{B2}^e \cdot \mathbf{w}_2^a = 1 \\ \int_{K_1} \psi_{B2}^e \cdot \mathbf{w}_3^a = 0 \end{cases} \tag{109}$$

We can thus obtain the solution for the coefficients:

$$\begin{cases} a = -2 \\ b = 4 \\ c = 0 \end{cases} \tag{110}$$

and the bi-orthogonal function associated with edge 2 (left-hand side):

$$\psi_{B2}^e = (2-6y)\mathbf{e_x} + (6x+4)\mathbf{e_y} \tag{111}$$

Triangle on the right: K_2

For the triangle on the right side, the nodal functions are:

$$\begin{cases} w_1^n = 1 - 2x - y \\ w_4^n = 2x \\ w_3^n = y \end{cases} \tag{112}$$

The edge functions can thus be constructed:

$$\begin{cases} \mathbf{w}_4^a = w_1^n \ \mathbf{grad} \ w_4^n - w_4^n \ \mathbf{grad} \ w_1^n = (2-2y)\mathbf{e_x} + 2x\mathbf{e_y} \\ \mathbf{w}_2^a = w_1^n \ \mathbf{grad} \ w_3^n - w_3^n \ \mathbf{grad} \ w_1^n = 2y\mathbf{e_x} + (1-2x)\mathbf{e_y} \\ \mathbf{w}_5^a = w_4^n \ \mathbf{grad} \ w_3^n - w_3^n \ \mathbf{grad} \ w_4^n = -2y\mathbf{e_x} + 2x\mathbf{e_y} \end{cases} \tag{113}$$

Let us write the bi-orthogonal function associated with edge 2 (oriented from n_1 to n_3) as the linear combination of the edge functions:

$$\psi_{B2}^{e\,\prime} = a' \ \mathbf{w}_4^a + b' \ \mathbf{w}_2^a + c' \ \mathbf{w}_5^a \tag{114}$$

with a', b' and c' the coefficients to be determined.

The equations to be solved are:

$$\begin{cases} \int_{K_2} \psi_{B\,2}^{e\,\prime} \cdot \mathbf{w}_4^a = 0 \\ \int_{K_2} \psi_{B\,2}^{e\,\prime} \cdot \mathbf{w}_2^a = 1 \\ \int_{K_2} \psi_{B\,2}^{e\,\prime} \cdot \mathbf{w}_5^a = 0 \end{cases} \tag{115}$$

We can thus obtain the solution for the coefficients:

$$\begin{cases} a' = -8/5 \\ b' = 28/5 \\ c' = 12/5 \end{cases} \tag{116}$$

and the bi-orthogonal function associated with edge 2 (right-hand side):

$$\psi_{B\,2}^{e\,\prime} = (\frac{48}{5}y - \frac{16}{5})\mathbf{e_x} + (\frac{28}{5} - \frac{48}{5}x)\mathbf{e_y} \tag{117}$$

Comparison with Whitney functions

The Whitney functions and obtained bi-orthogonal functions are illustrated in Figure 50.

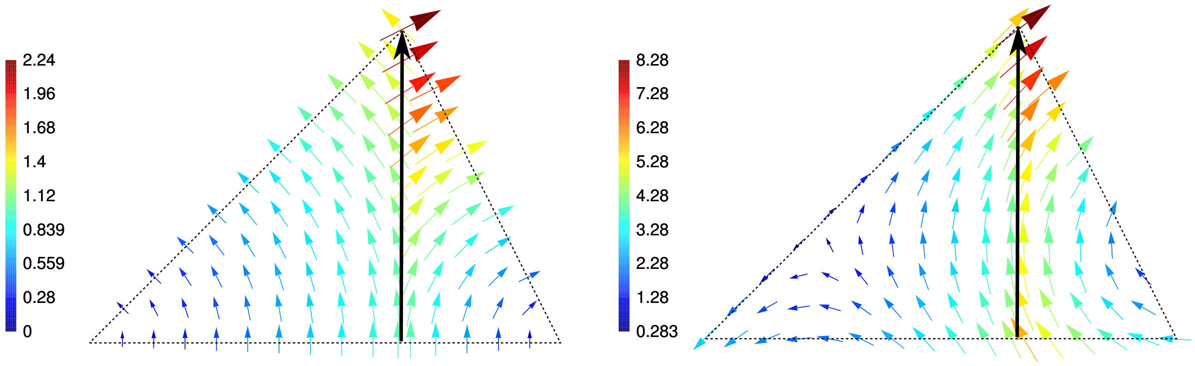

(a) Whitney functions

(b) Bi-orthogonal functions

Figure 50: Whitney functions and bi-orthogonal functions associated with the common edge.

For both triangles, we can remark that the tangential component of the Whitney function is zero at the bottom boundary. This is however not the case for bi-orthogonal functions: their tangential components are not continuous from one element to another. The gradient operator is thus non-applicable at the boundaries.

FACET BI-ORTHOGONAL FUNCTION

In the same was as for the edges, the determination of the facet bi-orthogonal functions can be demonstrated on the 2D mesh (Figure 49). For the sake of simplicity, a new point $n_5(0, 0, 1)$

is considered. The two triangles thus become the bottom of two tetrahedrons which share a common facet.

We can now determine the bi-orthogonal functions separately on both sides of the common facet.

Tetrahedron on the left: K_1

For the tetrahedron on the left side, the nodal functions are:

$$\begin{cases} w_1^n = 1 + x - y - z \\ w_2^n = -x \\ w_3^n = y \\ w_5^n = z \end{cases} \tag{118}$$

The Whitney functions can thus be constructed on each facet:

$$\begin{cases} \mathbf{w}_1^f = (2x)\mathbf{e_x} + (2y)\mathbf{e_y} + (2z-2)\mathbf{e_z} \\ \mathbf{w}_2^f = (-2x)\mathbf{e_x} + (2-2y)\mathbf{e_y} + (-2z)\mathbf{e_z} \\ \mathbf{w}_3^f = (2x+2)\mathbf{e_x} + (2y)\mathbf{e_y} + (2z)\mathbf{e_z} \\ \mathbf{w}_4^f = (-2x)\mathbf{e_x} + (-2y)\mathbf{e_y} + (-2z)\mathbf{e_z} \end{cases} \tag{119}$$

where facet f_1 is constructed by $n1$, $n2$ and $n3$; f_2: $n1$, $n2$ and $n5$; f_3: $n1$, $n3$ and $n5$; f_4: $n2$, $n3$ and $n5$.

The bi-orthogonal function to be determined at facet 3 is then described as the linear combination of Whitney functions and solved using a 4×4 linear system. The result is given as follows:

$$\boldsymbol{\psi}_{B3}^f = (\frac{20}{3}x + \frac{14}{3})\mathbf{e_x} + (\frac{20}{3}y - \frac{5}{3})\mathbf{e_y} + (\frac{20}{3}z - \frac{5}{3})\mathbf{e_z} \tag{120}$$

Tetrahedron on the right: K_2

For the tetrahedron on the right side, the nodal functions are:

$$\begin{cases} w_1^n = 1 - 2x - y - z \\ w_4^n = 2x \\ w_3^n = y \\ w_5^n = z \end{cases} \tag{121}$$

The Whitney functions can thus be constructed on each facet:

$$\begin{cases} \mathbf{w}_5^f = (-4x)\mathbf{e_x} + (-4y)\mathbf{e_y} + (4-4z)\mathbf{e_z} \\ \mathbf{w}_6^f = (4x)\mathbf{e_x} + (4y-4)\mathbf{e_y} + (4z)\mathbf{e_z} \\ \mathbf{w}_3^f = (2-4x)\mathbf{e_x} + (-4y)\mathbf{e_y} + (-4z)\mathbf{e_z} \\ \mathbf{w}_7^f = (4x)\mathbf{e_x} + (4y)\mathbf{e_y} + (4z)\mathbf{e_z} \end{cases} \tag{122}$$

where facet f_5 is constructed by $n1$, $n4$ and $n3$; f_6: $n1$, $n4$ and $n5$; f_7: $n4$, $n3$ and $n5$.

The bi-orthogonal function associated with facet 3 at the right side is calculated:

$$\psi^{f\,\prime}_{B3} = \left(-\frac{80}{9}x + \frac{64}{9}\right)\mathbf{e_x} + \left(-\frac{80}{9}y + \frac{20}{9}\right)\mathbf{e_y} + \left(-\frac{80}{9}z + \frac{20}{9}\right)\mathbf{e_z} \tag{123}$$

Comparison with Whitney functions

The Whitney functions and obtained bi-orthogonal functions are illustrated in Figure 51.

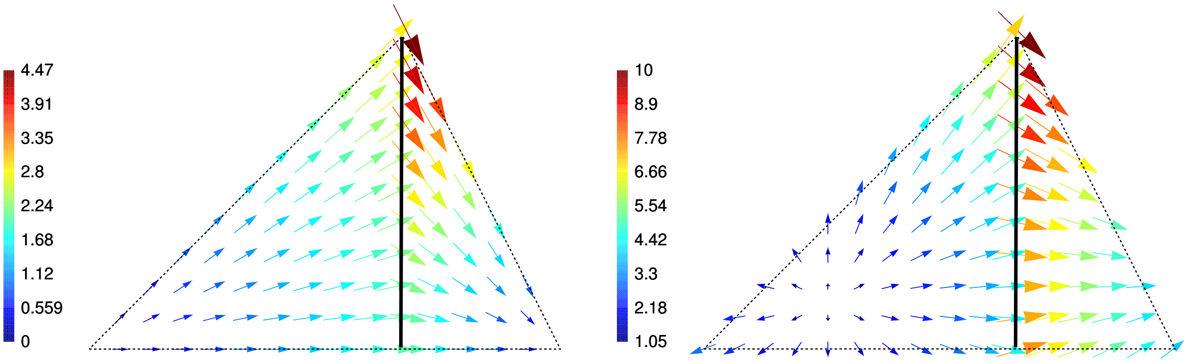

(a) Whitney functions (b) Bi-orthogonal functions

Figure 51: Whitney functions and bi-orthogonal functions associated with the common facet.

The normal component of the Whitney functions is continuous at the common facet and strictly zero for all other facets. Neither condition is however satisfied for bi-orthogonal functions. The thus determined bi-orthogonal functions are not members of $\mathbf{H}(\mathrm{div}, \mathscr{D})$.

ACKNOWLEDGMENTS

The work described in this thesis would have been impossible without supervisors and colleagues who are generous with their time and a family which is generous in its support.

First of all, I would like to express my deepest sense of gratitude to my supervisors: Prof. Francis Piriou (University of Lille 1), Dr. Thomas Henneron (University of Lille 1) and Dr. Jean-Claude Mipo (Valeo Electrical Systems). Thanks to them, I have never lacked advice or support in the course of this work.

I sincerely thank Prof. Herbert De Gersem (KU Leuven), Prof. Gérard Meunier (G2ELAB), Prof. Frédéric Bouillault (Supélec) and Prof. Patrick Dular (University of Liège) for accepting to be members of the examining board of this thesis.

In addition I want to warmly thank all the colleagues I worked with. In particular, I am much indebted to Prof. Stéphane Clénet (Arts et Métiers ParisTech), Dr. Yvonnick Le Menach (University of Lille 1), Prof. Nathan Ida (University of Akron) and Dr. Frédéric Palleschi (Valeo Electrical Systems) for their unreserved insight. In the same way, I wish to express my gratitude to Dr. Jean-Yves Roger (EDF R&D), Dr. Zuqi Tang (University of Lille 1), Dr. Nicolas Nemitz (EDF R&D) as well as Dr. Antoine Journaux (Supélec) for the time they shared with me in our cooperation on exciting research topics.

I do not forget all my colleagues at the laboratory: Radu, Ludovic, Mircea, Clément(s), Bruno, Juliana, Antoine, Sijun, Abedelmounaïm, Abdelkader, Wenhua, Loïc, Julien, Claire, Virginie, Quang, Francisc, Rindra, Jalal, Nicolas, Ke, Ali, Laure, Hung, Tony, Carlos, Reberta, Karim, Medhi, Aymen, Bassel, Sajjed… The simple phrase “Thank you”, is far from enough to express my gratitude for their companionship.

I thank Valeo Electrical Systems and the French National Association of Research and Technologies for funding my research, and the Laboratory of Electrical Engineering and Power Electronics Power for providing the excellent conditions and great freedom during three years.

Finally, I would like to take the opportunity to thank my family and friends who shared my daily life and kept me sane during the realization of this thesis. None of my work would have been possible without their love and support.

BIBLIOGRAPHY

[1] V. Cingoski, A. Namera, K. Kaneda, and H. Yamashita. Analysis of magneto-thermal coupled problem involving moving eddy-current conductors. *IEEE Transactions on Magnetics*, 32(3):1042 –1045, may 1996. (Cited on page 1.)

[2] F. Roy, B. Dutoit, F. Grilli, and F. Sirois. Magneto-thermal modeling of second-generation hts for resistive fault current limiter design purposes. *IEEE Transactions on Applied Superconductivity*, 18(1):29 –35, march 2008. (Cited on page 1.)

[3] H. Kurose, D. Miyagi, N. Takahashi, N. Uchida, and K. Kawanaka. 3-d eddy current analysis of induction heating apparatus considering heat emission, heat conduction, and temperature dependence of magnetic characteristics. *IEEE Transactions on Magnetics*, 45(3):1847 –1850, march 2009. (Cited on page 1.)

[4] N. Nemitz, O. Moreau, and Y. Ould-Rouis. Magneto-thermal coupling: A conservative-based method for scalar field projection. In *Compumag*, Sydney, Australia, 2011. (Cited on page 1.)

[5] F. C. Moon. *Magneto-solid mechanics*. Wiley-Interscience. John Wiley & Sons, 1984. ISBN 0-471-88536-3. (Cited on pages 1 and 57.)

[6] Z. Ren and A. Razek. Modelling of dynamical behaviours of electro-magneto-mechanical coupled systems. In *Second International Conference on Computation in Electromagnetics*, pages 20–23, 1994. (Cited on page 1.)

[7] Z. Ren, B. Ionescu, M. Besbes, and A. Razek. Calculation of mechanical deformation of magnetic materials in electromagnetic devices. *IEEE Transactions on Magnetics*, 31:1873–1876, 1995. (Cited on page 1.)

[8] A. Bossavit. Discrete magneto-elasticity: A geometrical approach. *IEEE Transactions on Magnetics*, 46(8):3485 –3491, aug. 2010. (Cited on pages 1 and 13.)

[9] Z. Wang, A.A. Journeaux, T. Henneron, F. Bouillault, N. Nemitz, J.-Y. Roger, J.-C. Mipo, and F. Piriou. Modelling of magneto-elastic problems on disconnected meshes. In *Numélec*, Marseille, France, 2012. invited paper. (Cited on pages 1 and 80.)

[10] A.A. Journeaux, F. Bouillault, and J. Roger. Magneto-mechanical dynamic system modeling using computer code chaining and field projections. *IEEE Transactions on Magnetics*, 49(5):1757–1760, 2013. (Cited on page 1.)

[11] A. A. Journeaux, A. Bossavit, and F. Bouillaut. Relevance of magnetic behaviour in the modelling of electro-mechanical systems. *The European Physical Journal - Applied Physics*, eFirst, 9 2013. (Cited on page 1.)

[12] A. A. Journeaux, F. Bouillaut, and J. Roger. Multi-physics problems computation using numerically adapted meshes: application to magneto-thermo-mechanical systems. *The European Physical Journal - Applied Physics*, 61, 3 2013. (Cited on page 1.)

[13] A. Marrocco. Analyse numérique des problèmes en électrotechnique. *Ann. Cs. Math.*, 1:271–296, 1977. (Cited on page 5.)

[14] A. Bossavit. *Computational Electromagnetism*. Academic Press, 1998. (Cited on pages 6, 13, and 14.)

[15] Z. Ren. A 3d vector potential formulation using edge element for electrostatic field computation. *IEEE Transactions on Magnetics*, 31(3):1520–1523, 1995. (Cited on page 6.)

[16] Morton E Gurtin. The linear theory of elasticity. *Solid-state mechanics 2.(A 73-11976 02-32) Berlin, Springer-Verlag, 1972,*, pages 1–295, 1972. (Cited on page 8.)

[17] L Victor Berdichevsky. *Variational principles of continuum mechanics*. London-New York, 2009. (Cited on page 8.)

[18] Frank Incropera and David DeWitt. *Introduction to heat transfer*. John Wiley and Sons Inc., New York, NY, 1985. (Cited on page 10.)

[19] Kevin D Cole. *Heat conduction using Green's functions*. CRC Press, 2011. (Cited on page 10.)

[20] R. A. Adams and J. JF. Fournier. *Sobolev Spaces*, volume 140. Academic press, 2003. (Cited on pages 12 and 18.)

[21] Prasanta Kumar Banerjee and Roy Butterfield. *Boundary element methods in engineering science*, volume 17. McGraw-Hill London, 1981. (Cited on page 13.)

[22] Carlos Alberto Brebbia, José Claudio Faria Telles, and Luiz C Wrobel. *Boundary element techniques: theory and applications in engineering*, volume 5. Springer-Verlag Berlin, 1984. (Cited on page 13.)

[23] Thomas Weiland. Time domain electromagnetic field computation with finite difference methods. *International Journal of Numerical Modelling: Electronic Networks, Devices and Fields*, 9(4):295–319, 1996. (Cited on page 13.)

[24] Natarajan Sukumar. *The natural element method in solid mechanics*. PhD thesis, Northwestern University, 1998. (Cited on page 13.)

[25] Hassler Whitney. *Geometric integration theory*, volume 21. Princeton UP, 1957. (Cited on page 14.)

[26] A. Bossavit. Whitney forms: a class of finite elements for three-dimensional computations in electromagnetism. *Physical Science, Measurement and Instrumentation, Management and Education - Reviews, IEE Proceedings A*, 135(8):493–500, 1988. (Cited on page 14.)

[27] C. Geuzaine, B. Meys, F. Henrotte, P. Dular, and W. Legros. A Galerkin projection method for mixed finite elements. *IEEE Transactions on Magnetics*, 35(3):1438 –1441, may 1999. (Cited on pages 17 and 21.)

[28] G. Parent, P. Dular, J. P Ducreux, and F. Piriou. Using a Galerkin projection method for coupled problems. *IEEE Transactions on Magnetics*, 44(6):830–833, 2008. (Cited on pages 17 and 21.)

[29] Faker Ben Belgacem. The mortar finite element method with lagrange multipliers. *Numerische Mathematik*, 84:173–197, 1999. 10.1007/s002110050468. (Cited on pages 17 and 21.)

[30] B. I. Wohlmuth. A mortar finite element method using dual spaces for the lagrange multiplier. *SIAM Journal on Numerical Analysis*, 38(3):989–1012, 2000. (Cited on pages 17, 21, and 22.)

[31] B. Flemisch, Y. Maday, F. Rapetti, and B.I. Wohlmuth. Coupling scalar and vector potentials on nonmatching grids for eddy currents in a moving conductor. *Journal of Computational and Applied Mathematics*, 168:191 – 205, 2004. (Cited on pages 17 and 21.)

[32] L. Demkowicz and A. A. Buffa. h^1, $h(curl)$ and $h(div)$-conforming projection-based interpolation in three-dimensions, quasi-optimal p-interpolation estimates. *Comput. Methods Appl. Mech. Engrg.*, 194:267–296, 2005. (Cited on page 17.)

[33] O.J. Antunes, J.P.A. Bastos, N. Sadowski, A. Razek, L. Santandrea, F. Bouillault, and F. Rapetti. Using hierarchic interpolation with mortar element method for electrical machines analysis. *IEEE Transactions on Magnetics*, 41(5):1472 – 1475, may 2005. (Cited on pages 17 and 21.)

[34] P. Dular, R.V. Sabariego, M.V.F. da Luz, P. Kuo-Peng, and L. Krahenbuhl. Perturbation finite element method for magnetic model refinement of air gaps and leakage fluxes. *IEEE Transactions on Magnetics*, 45(3):1400 –1403, march 2009. (Cited on pages 17 and 21.)

[35] A. Bossavit. How weak is the weak solution in finite element methods? *IEEE Transactions on Magnetics*, 34(5):2429–2432, 1998. (Cited on page 20.)

[36] L. Debnath and P. Mikusinski. *Introduction to Hilbert Spaces with Applications*. Elsevier/Academic Press, Inc., 3 edition, 2005. ISBN: 0-12-208438-1. (Cited on page 20.)

[37] J. Cea. *Approximation variationnelle des problemes aux limites*. PhD thesis, Institut Fourier, 1964. 14. 2. p345. (Cited on page 20.)

[38] A. Cauchy. *Oeuvres* 2. Ecole Royale Polytechnique, 1821. (Cited on page 20.)

[39] P. Lax and J. A. Milgram. Parabolic equations and semigroup. *Annals of Math. Studies*, 33:167–190, 1954. (Cited on page 20.)

[40] Lars B Wahlbin. *Superconvergence in Galerkin finite element methods*. Springer Berlin, 1995. (Cited on page 21.)

[41] R. Dautray and J.-L. Lions. *Analyse mathématique et calcul numérique pour les sciences et les techniques*. Masson, 1984 - 1985. (Cited on page 21.)

[42] J.J. Dongarra. *Numerical Linear Algebra for High-Performance Computers*. Software, Environments, Tools. Society for Industrial and Applied Mathematics, 1998. (Cited on page 21.)

[43] L. R. Scott and S. Zhang. Finite element interpolation of nonsmooth functions satisfying boundary conditions. *Mathematics of Computation*, 54:483–493, April 1990. (Cited on page 22.)

[44] E. Lange, F. Henrotte, and K. Hameyer. A variational formulation for nonconforming sliding interfaces in finite element analysis of electric machines. *IEEE Transactions on Magnetics*, 46(8):2755–2758, 2010. (Cited on page 22.)

[45] M. Aubertin, T. Henneron, F. Piriou, and J.-C. Mipo. Mortar method using bi-orthogonal nodal functions applied to a-phi formulation. *IEEE Transactions on Magnetics*, 48(2):491 –494, feb. 2012. (Cited on page 22.)

[46] J. Dieudonne. On biorthogonal systems. *Michigan Math.*, 2:7–20, 1954. Mathematical Reviews (MathSciNet): MR16:47c. Zentralblatt MATH: 0055.33704. (Cited on page 22.)

[47] B. Wohlmuth. A comparison of dual Lagrange multiplier spaces for mortar finite element discretizations. *M2AN Math. Model. Numer. Anal.*, 36:995–1012, 2002. (Cited on pages 23, 27, and 38.)

[48] E. Lange, F. Henrotte, and K. Hameyer. Biorthogonal shape functions for nonconforming sliding interfaces in 3-d electrical machine fe models with motion. *Magnetics, IEEE Transactions on*, 48(2):855 –858, feb. 2012. (Cited on page 23.)

[49] P.E. Farrell, M.D. Piggott, C.C. Pain, G.J. Gorman, and C.R. Wilson. Conservative interpolation between unstructured meshes via supermesh construction. *Computer Methods in Applied Mechanics and Engineering*, 198:2632 – 2642, 2009. (Cited on pages 25 and 35.)

[50] P.E. Farrell and J.R. Maddison. Conservative interpolation between volume meshes by local galerkin projection. *Computer Methods in Applied Mechanics and Engineering*, 200:89 – 100, 2011. (Cited on page 25.)

[51] Ivan E. Sutherland and Gary W. Hodgman. Reentrant polygon clipping. *Commun. ACM*, 17(1):32–42, January 1974. (Cited on page 25.)

[52] Mike Cyrus and Jay Beck. Generalized two- and three-dimensional clipping. *Computers & Graphics*, 3(1):23 – 28, 1978. (Cited on page 25.)

[53] Z. Wang, T. Henneron, N. Nemitz, J.-C. Mipo, and F. Piriou. Electromagnetic field projection on finite element overlapping domains. *IEEE Transactions on Magnetics*, 49(4):1290–1298, 2013. (Cited on pages 26, 65, and 80.)

[54] F. Ben Belgacem, A. Buffa, and Y. Maday. The mortar finite element method for 3d maxwell equations: First results. *SJNAAM*, 39(3):880–901, 2001. (Cited on pages 30 and 38.)

[55] Xiangmin Jiao and Michael T. Heath. Common-refinement-based data transfer between nonmatching meshes in multiphysics simulations. *International Journal for Numerical Methods in Engineering*, 61:2402–2427, 2004. (Cited on page 35.)

[56] Z. Wang, T. Henneron, P. Dular, J.-C. Mipo, and F. Piriou. Comparison of implementation techniques for Galerkin projection between different meshes. *Journal of Numerical Modelling: Electronic Networks, Devices and Fields*, 2013. to be published, poster presentation in EMF 2013. (Cited on pages 36, 65, and 80.)

[57] J. L. Coulomb. A methodology for the determination of global electomechanical quantities from a fea and its application to the evaluation of magnetic forces, torques and stiffness. *IEEE Transactions on magnetics*, Mag-19, No.6:2514–2519, November 1983. (Cited on pages 39 and 59.)

[58] Z. Wang, T. Henneron, J.-C. Mipo, and F. Piriou. Projection des champs entre deux maillages par une approche énergétique. In *Numélec*, Marseille, France, 2012. poster presentation. (Cited on pages 39 and 81.)

[59] Z. Wang, Z. Tang, T. Henneron, J.-C. Mipo, and F. Piriou. Energetic Galerkin projection of electromagnetic fields between different meshes. *IEEE Transactions on Magnetics*, 2013. to be pulished, poster presentation in Compumag 2013. (Cited on pages 39, 41, and 81.)

[60] Z. Tang. *Estimateurs d'erreur a posteriori résiduels en éléments finis pour la résolution des problèmes d'électromgnétisme en formulations potentielles*. PhD thesis, Université Lille 1, 2012. (Cited on page 41.)

[61] Emmanuel Creusé, Serge Nicaise, Zuqi Tang, Yvonnick Le Menach, Nicolas Nemitz, and Francis Piriou. Residual-based a posteriori estimators for the A/ϕ magnetodynamic harmonic formulation of the maxwell system. *Mathematical Models and Methods in Applied Sciences*, 22(05):1150028, 2012. (Cited on page 41.)

[62] Emmanuel Creusé, Serge Nicaise, Zuqi Tang, Yvonnick Le Menach, Nicolas Nemitz, and Francis Piriou. Residual-based a posteriori estimators for the T/Ω magnetodynamic harmonic formulation of the maxwell system. *International Journal of Numerical Analysis and Modeling*, 10(2):411–429, 2013. (Cited on page 41.)

[63] Y. Le Menach, S. Clénet, and F. Piriou. Numerical model to discretize source fields in the 3d finite element method. *IEEE Transactions on Magnetics*, 36(4):676–679, 2000. (Cited on page 52.)

[64] P. Dular, P. Kuo-Peng, C. Geuzaine, N. Sadowski, and J. P A Bastos. Dual magnetodynamic formulations and their source fields associated with massive and stranded inductors. *Magnetics, IEEE Transactions on*, 36(4):1293–1299, 2000. (Cited on page 52.)

[65] S. Clénet. Model with source terms in the constitutive relationship. *Magnetics, IEEE Transactions on*, 38(2):481–484, 2002. (Cited on page 52.)

[66] T. Henneron. *Contribution a la prise en compte des Grandeurs Globales dans les Problemes dElectromagnetisme resolus avec la Methode des Elements Finis*. PhD thesis, Universite Lille 1, 2004. (Cited on page 52.)

[67] Patrick Dular. Curl-conform source fields in finite element formulations: Automatic construction of a reduced form. *COMPEL: The International Journal for Computation and Mathematics in Electrical and Electronic Engineering*, 24:364–373, 2005. (Cited on page 52.)

[68] A. Pierquin, Y. Lemenach, Y. Roger, and L. Chevallier. Imposition d'un courant uniforme dans un conducteur. In *Numélec*, Marseille, France, 2012. (Cited on page 52.)

[69] Y. Le Menach, S. Clénet, and F. Piriou. Determination and utilization of the source field in 3d magnetostatic problems. *IEEE Transactions on Magnetics*, 34(5):2509–2512, 1998. (Cited on page 54.)

[70] Y. Le Menach. *Contribution à la modélisation numérique tridimensionnelle des systèmes électrotechniques*. PhD thesis, Université Lille1, 1999. (Cited on page 54.)

[71] K. Yuan. Magneto-thermo-elastic stresses in an infinitely long cylindrical conductor carrying a uniformly distributed axial current. *Applied Scientific Research*, 26:307–314, 1972. 10.1007/BF01897857. (Cited on page 58.)

[72] A.R. El Dhaba', A.F. Ghaleb, and M.S. Abou-Dina. A plane problem of uncoupled thermomagnetoelasticity for an infinite, elliptical cylinder carrying a steady axial current by a boundary integral method. *Applied Mathematical Modelling*, 31(3):448 – 477, 2007. (Cited on page 58.)

[73] W. Muller. Comparison of different methods of force calculation. *IEEE Transactions on Magnetics*, 26(2):1058–1061, 1990. (Cited on page 59.)

[74] A. Bossavit. Edge-element computation of the force field in deformable bodies. *IEEE Transactions on Magnetics*, 28(2):1263–1266, 1992. (Cited on page 59.)

[75] Z. Ren and A. Razek. Local force computation in deformable bodies using edge elements. *IEEE Transactions on Magnetics*, 28(2):1212–1215, 1992. (Cited on page 59.)

[76] L. H. de Medeiros, G. Reyne, and G. Meunier. About the distribution of forces in permanent magnets. *IEEE Transactions on Magnetics*, 35(3; given that only the method based on the virtual work principle provides reliable results):1215–1218, 1999. (Cited on page 59.)

[77] F. Henrotte, H. V. Sande, G. Deliege, and K. Hameyer. Electromagnetic force density in a ferromagnetic material. *IEEE Transactions on Magnetics*, 40(2):553–556, 2004. (Cited on page 59.)